University of Dundee

DOCTOR OF PHILOSOPHY

Cavitation in focused ultrasound

Gerold, Bjoern

Award date:
2013

DOCTOR OF PHILOSOPHY

Cavitation in focused ultrasound

Bjoern Gerold

2013

University of Dundee

Cavitation in focused ultrasound

Bjoern Gerold

A thesis submitted for the degree of

PhilosophiæDoctor (PhD)

University of Dundee

April 2013

To my wife Karine

Contents

List of Figures

List of Tables

Acknowledgements

Completing a PhD is truly a marathon event, and I would not have been able to complete this without my supervisor an expert in this field, Dr Paul Prentice. He showed me the fascination of physics, in particular the world of bubbles. He did not give up when my scientific writing most needed him. His attention to detail and hard work made this thesis possible. Therefore, I am immensely thankful for this experience. Finally I would like to thank him for not breaking my leg during football and for increasing my tolerance to alcohol in the pub.

I would like to thank Graham Brodie, Craig McDougall, Spiros Kotopoulis and all the other colleagues in the office for their help in the lab and the constructive discussions. Mike MacDonald and David McGloin for their contribution.

Thanks to Javier Grinfeld, Oleg Prus and Itay Rachmilevitch for making me feel welcome in Insightec and for their invaluable ultrasound tips & tricks.

I would like to thank Prof. Sandy Cochran for all the things he has done to help me since he was my MSc supervisor up-till now. Thanks to Christine Demore and the ultrasound team for always assisting me in the last years.

I am grateful to Prof. Andreas Melzer and Prof. Yoav Medan and the Nanoporation project to have provided a stimulating and supporting environment, which allowed me to be successful with my research.

Furthermore I would like to thank Prof. Eitan Kimmel and his students for for their hospitality in the Technion.

I would like to thank all the people from many corners of the world that I met over the last three years. In particular, Joyce, for introducing me to India, Tamir to Israel, and my friend Tommaso who always was there when I needed him.

I also acknowledge Adrian Walker and the EPSRC loan pool for providing the high-speed cameras which became such vital components of this work.

My family for always believing in me.

And finally last, but not least, I am in deep debt with Karine, my wonderful wife, for her stoicism when I was away, for her patience when I was at home, and her help especially during the writing up phase of the thesis. Without her support and love I might not have made it.

Declaration

I hereby declare that this dissertation entitled '*Cavitation in focused ultrasound*' has been prepared by me under the direct guidance of Dr. Paul Prentice as part of my study for the award of PhD Degree at the University of Dundee, Dundee, Scotland. I have not submitted this dissertation previously for the award of any degree or diploma at any other institution.

Dundee,

Abstract

A novel experimental configuration is developed combining a high-intensity focused ultrasound source and a pulsed-laser, for the study of cavitation in a field typical of those used for therapeutic ultrasound. The *sonoptic chamber* is specifically designed to avoid the formation of acoustic standing waves, known to have a critical influence on cavitation behaviour. A new technique of *laser-nucleated acoustic cavitation* is presented, whereby a laser-pulse of energy below the breakdown threshold for the host medium, acts to nucleate acoustic cavitation in a pre-established field. This facilitates the incorporation of high-speed cameras for interrogation at unprecedented temporal and spatial resolution, combined with acoustic detection directly correlated to the observed cavitation activity. A number of cavitation phenomena are investigated, including bubble-ensemble oscillations at a very early stage of development, in response to the acoustic driving. The frequency of oscillation, which bifurcates with increasing intensity, is also detected in the acoustic emissions. The application of a single-bubble model predicts a source for the acoustic emissions of quiescent radius equivalent to the bubble-ensemble observed, for each intensity investigated. The physical translation of the ensemble, due to the radiation force imposed by the primary field, is also analysed. For laser-pulses of energy above the breakdown threshold, applying focused ultrasound to the cavity promotes and actuates jet-formation. The characteristics of the so formed jets depend on the intensity and location of the cavity relative to the ultrasound focus.

Glossary

1 : *Symbols*

$\alpha(f)$	attenuation coefficient (frequency dependent)
$\bar{v}_t$	experimentally measured translational velocity
η	shear viscosity
γ	dimensionless stand-off parameter
γ	polytropic exponent
λ	wavelength
λ_0	wavelength of fundamental frequency of an acoustic field
Ω	solid angle
ρ	density
ρ_0	specific density of the medium
σ	surface tension
τ	duration of acoustic cycle
τ_c	time for collapse of an empty cavity
θ	angle from US axis
$\vec{F_r}$	radiation force vector
$\vec{n}$	surface normal vector
$\vec{u_1}$	first order acoustic velocity vector
A	Area
A	amplitude
A_0	amplitude at source
B_{AD}	adiabatic bulk modulus
c	speed of sound (specific medium)
C_d	drag coefficient
C_{MI}	derating factor for MI
f	frequency of sound
f_0	fundamental frequency of an acoustic field
f_c	centre frequency
f_e	emitted frequency
F_r	radiation force
f_r	bubble resonance frequency
I_{sa}	spatial-average intensity
m	mass
N	number of cycles
p	acoustic pressure
p_0	ambient pressure
p_g	gas pressure
p_i	internal pressure
p_v	vapour pressure
p_σ	Laplace pressure
R	bubble radius
R_0	bubble equilibrium radius

R_{crit}	critical radius or Blake radius
R_{eff}	effective average cloud radius
R_{max}	maximum radius
Re	Reynolds number
T	temperature
t	time
V	bubble volume
v_t	translation velocity
W_0	source power
W_e	electrical power
W_{ac}	acoustic power
Z_0	specific acoustic impedance

2: Acronyms

ARFI	Acoustic Radiation Force Impulse Imaging
BBB	Blood Brain Barrier
CW	Continuous Wave
DC	Duty Cycle
ESWL	Extra-corporeal Shock-Wave Lithotripsy
FDA	Food and Drug Administration
FUS	Focused Ultrasound Surgery
HIFU	High Intensity Focused Ultrasound
LIC	Laser-Induced Cavity
LNAC	Laser-Nucleated Acoustic Cavitation
MI	Mechanical Index
MRgFUS	Magnetic Resonance guided Focused Ultrasound Surgery
MRI	Magnetic Resonance Imaging
PNP	Peak Negative pressure
PRF	Pulse Repetition Frequency
PVDF	PolyVinyliDene Fluoride
PW	Pulsed Wave
TI	thermal index
US	ultrasound
USgFUS	Focused Ultrasound Surgery

1

A brief introduction to the phenomenon of cavitation

The term *cavitation* refers to any situation whereby a pocket of gas develops within a liquid host medium. The word 'bubble' can also be used to describe this system - and the two are used interchangeably throughout this thesis. A distinction between the bubbles encountered in a glass of champagne, for example, and bubbles formed from a soapy solution should, however, be made for clarity. The latter represents an internal gas-liquid film-external gas interfacial configuration, with striking colour patterns forming in the liquid film, due to light interference effects related to its thickness. The former is an internal gas-bulk liquid scenario, for which the opposing tendencies for the compressibility of the core-gas to expand, and the inertia of the host medium to collapse the cavity can result in a dynamic oscillating system.

The imposition of acoustic driving to the internal gas-bulk liquid bubble therefore, by extension, represents a forced oscillator system. Here, the compressibility of the internal gas renders the bubble sensitive to the pressure fluctuations of the acoustic field propagating through the comparatively incompressible liquid host medium. The additional energy delivered by the field, can drive the *acoustic cavity* into an, at times, bewildering array of response dynamics, dependent on the

local fluid environment and the parameters of the applied field. For example, the internal gas of a bubble strongly collapsed by a positive over-pressure phase, can achieve a remarkably high, albeit transient, energy density. Under the correct experimental arrangement, bubble core material will enter the plasma state-of-matter (whereby electrons are stripped, or dissociated, from parent molecules), indicating fleeting temperatures in excess of 10^4 K. Perhaps the most astonishing phenomenon associated with such extreme core conditions is that of *sonoluminescence*, which refers to flashes of light emitted from the bubble, at the instant of maximum compression. This bubble mediated sound-to-light transduction has been coined the star-in-a-jar, in recognition of conditions more usually associated with a stellar environment. The high temperatures and pressures reached within a bubble, subject to acoustic driving, are also known to mediate exotic chemical reactions, generating highly reactive free-radical species, for example. This energy-focusing effect is utilised industrially, in the form of *sonochemistry*, to accelerate the production of a useful chemical, or to degrade waste material for disposal.

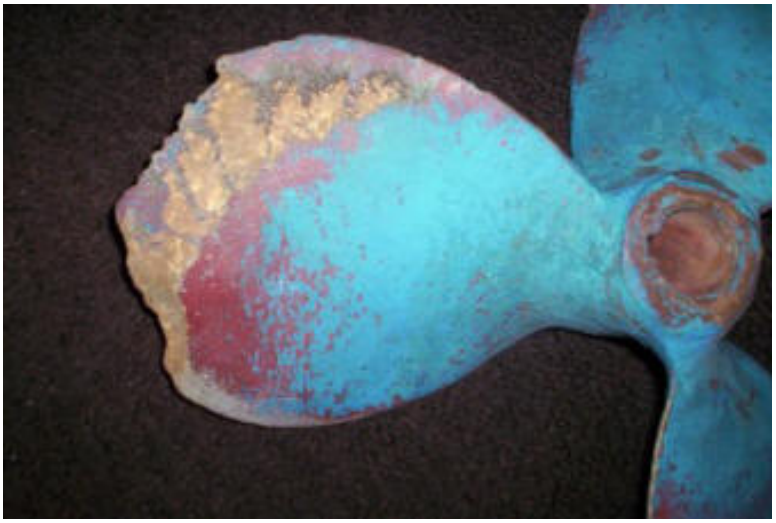

Figure 1.1: Cavitation damage - Cavitation can result from 'nicks' and sharp corners in the leading edge, bent blades, too much cup, incorrect matching of propeller style to the vessel and engine, or simply from being driven above a threshold rotation speed. From www.olds.com.au

Cavitation was first subject to scientific enquiry toward the end of the 19th century. Following the Steam-Revolution, marine engineers noted that ships were not attaining the maximum speeds predicted theoretically. The discrepancy was eventually correctly attributed to the formation of cavitation bubbles in the host medium, under the tension exerted by a rapidly rotating propeller. Moreover, it was found that the action of cavitation over time would lead to erosion, and ultimately the disintegration, of the steel of the propeller itself, fig. 1.1. This was early testament to the destructive potential of bubbly liquids, which led to the notorious reputation cavitation largely endures to this day. Nonetheless, the phenomenon is employed to beneficial effect in a wide range of processes, including *acoustic cleaning* of jewellery and surgical instrumentation, where the erosive nature of cavitation is used to remove contaminants from surfaces, and kidney-stone destruction, for which cavitation formed in the wake of a focused shock-wave is thought to contribute to stone fragmentation.

A novel and exciting application of cavitation is in the field of *focused ultrasound surgery* (FUS), itself an emerging clinical approach to the delivery of therapy non-invasively (so-called incision-less intervention). FUS procedures currently involve the extracorporeal administration of *high intensity focused ultrasound* (HIFU), to mediate the deposition of heat to a target region of diseased tissue. The absorption of acoustic energy at the focus forms a lesion of coagulated (cancerous) cells, with a non-ionising form of radiation. The technique thus offers localised therapy, with significantly reduced patient recovery time and associated risk of infection. The formation of cavitation in the HIFU produced by a typical focused-transducer device, fig. 1.2, is a common occurrence.

Cavitation in tissue can have the same violent and destructive effects as outlined above. Indeed, the interaction of cavitation with the HIFU radiation itself, can result in significantly malformed and difficult to predict lesioning during FUS. As such, the phenomenon is generally avoided for current FUS procedures.

There is, however, a growing realisation that cavitation could in fact revo-

Figure 1.2: Acoustic cavitation - Cavitation beneath a sonotrode ultrasound device, of 120 mm diameter. From Lauterborn [76]

lutionise the remit of FUS, to include drug-delivery applications and blood-clot dissolution, for example.

The rationale here is that bubble activity, in the region of the acoustic focus, could act to permeabilise tissue structures, rendering them susceptible to the action of drug compounds. Moreover, bubble-oscillations driven by the HIFU exposure may actively promote drug delivery to the diseased tissue. The extremely rapid evolution of cavitation in a HIFU field, combined with the high risk of collateral damage to surrounding healthy tissue, conspire to make the safe and controlled introduction of cavitation to tissue a significant and outstanding challenge.

Historically, a popular technique adopted by cavitation researchers to study bubble dynamics, involves focusing short, intense laser-pulses into a liquid host medium. The approach results in localised vaporisation of the liquid at the focus to form a bubble, commonly known as a *laser-induced cavity* (LIC). The intrinsic advantage of this process is that the precise location and moment of bubble formation is pre-determined, by the generation and focal position of the laser-pulse, respectively. This allows the implementation of high-frame rate cameras, to image the ensuing dynamics in great detail. In contrast, a significant limitation to the study of *acoustic* or *hydrodynamic* cavitation has been the difficulty in predicting the moment and location of bubble activity inception, in a HIFU field, or in proximity to a propeller blade, for example. The knowledge of bubble

dynamics obtained through the laser-induced technique is of limited use in terms of understanding 'naturally' forming cavitation, as key bubble characteristics are critically dependent on the conditions underpinning their formation. The pertinent characteristics of HIFU cavitation bubbles are discussed in detail in the background sections (see §2.2.2) that follow. Moreover, the behaviour of a bubble immediately after it forms, is strongly dependent on the local pressure conditions, which is the feature common to all the observations presented in the results of Chapter 4.

The work behind this thesis centres on an experimental configuration designed to confer the distinct advantage of the LIC technique, for relevance to acoustic cavitation, in a HIFU field. The term *laser-nucleated acoustic cavitation* (LNAC) is used to describe the bubble activity resulting from a combination radiation exposure; that is pulsed-laser simultaneous with focused ultrasound. The resulting acoustic cavitation observations, at unprecedented spatial and temporal resolution, might herald a significant advance in the understanding of bubble behaviour in HIFU. In turn, this may pave the way for the development of strategies and devices to monitor, control, and even manipulate cavitation in tissue, for the potential enhancement of therapy in the next generation of FUS-procedures.

2

Background

2.1 Ultrasound

2.1.1 What is ultrasound?

Sound is a mechanical longitudinal pressure wave that propagates through a medium as a series of compressions and rarefactions, such that constituent particles oscillate parallel to the direction of the energy transfer. As with all mechanical waves, ultrasound requires a medium-of-transfer, and is known to propagate through all states-of-matter (gas, liquid, solid), with some dependence on wave parameters. A second type of wave associated with ultrasound are *shear waves*, whereby the particles move in a direction perpendicular to that of wave propagation. These waves exist only in solids, including tissue. In this thesis, ultrasound primarily refers to *longitudinal waves*. The periodic phases of high and low pressure occur at time intervals determined by the frequency, f, of the sound, related to *pitch*, for the audible regime. Pressure waves can be produced by human vocal cords in the range of 60 to 7,000 Hz and are detectable by the human ear in the range of 20 to 20,000 Hz. The difference in pressure between the compression phase and the rarefaction is related to how loudly the sound is perceived. This can be expressed in terms of intensity, as the power radiating per unit area, W/cm^2 (or equivalent). Ultrasound (US) simply refers to pressure waves at fre-

quencies higher than the detection capability of the human ear. Specifically the word ultrasound is therefore used to describe pressure waves at frequencies above 20 kHz. In nature, animals such as bats and dolphins use ultrasound (circa 14-100kHz and 40-150 kHz, respectively) to navigate their environment. Using a technique known as *echo-location*, such animals are able to distinguish objects with a high degree of precision, from the reflected sound patterns.

The detection, and indeed generation, of ultrasonic frequencies was made possible by the discovery of the piezoelectric effect, by the Curie brothers in 1881. The piezoelectricity of certain materials allows the conversion of electrical to mechanical energy, and vice versa. The first materials used were quartz crystals, followed by synthetic materials, such as ceramics. Subjected to electrical stimulation at the appropriate frequency, such materials vibrate to produce pressure waves that propagate through a medium as sound, or ultrasound. Since then, ultrasound technologies have been developed for a broad range of applications, including *sound navigation and ranging* (SONAR) submarine navigation, *non-destructive testing* (NDT), and in medicine for diagnosis and therapy. The upper boundary for medical applications is generally $\sim$15 MHz, although higher frequencies are explored for use in special applications, such as high resolution imaging.

2.1.2 History of ultrasound in medicine

In 1940, Firestone invented the *supersonic reflectroscope*, which used pulse echo-ranging to detect and locate defects in metals. Donald became familiar with the reflectroscope to detect cracks in the wings of aeroplanes when serving with the Royal Air Force during the Second World War. He later implemented the technique of pulse echo-ranging on human volunteers, publishing his findings in the Lancet in 1958 as *'Investigation of Abdominal Masses by Pulsed Ultrasound'* (Donald *et al.* [36]), the seminal paper published in the field of diagnostic medical imaging.

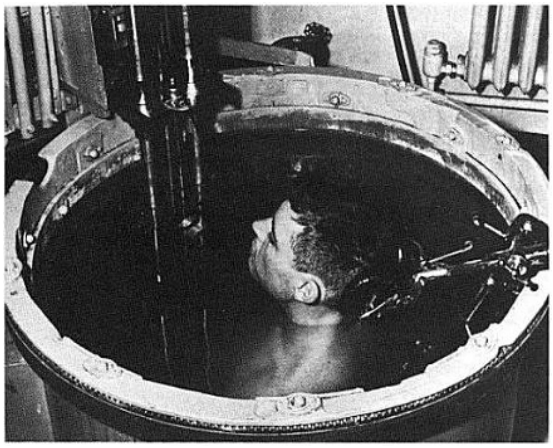

Figure 2.1: One of the first diagnostic ultrasound devices - The gun turret from a B-29 bomber was converted to obtain a ultrasonic tomographic system. After Szabo [113].

Parallel to the now familiar application of ultrasound imaging, ultrasound for therapy was also under development. In 1917, Langevin was one of the first scientists to utilize piezoelectric materials to produce ultrasound waves, thereby creating the first ultrasonic transducer (as referenced by O'Brien [97]). He was also one of the first to report on the *bioeffects* of ultrasound, noticing that fish would sometimes die on exposure. The concept of implementing ultrasound for therapy arose from the discovery that ultrasound creates heating in tissue (see §2.1.4). In 1938, Pohlman introduced ultrasonic physiotherapy as a medical practice at the Charite in Berlin (as referenced by Kremkau [71]). He suggested: "that the power of the transducer should be limited to $5W/cm^2$, that the transducer must be kept in motion, and insonifying the bone must be avoided". This statement indicates that even then, the potentially hazardous effects of using ultrasound in tissue were known. The use of High Intensity Focused Ultrasound (HIFU) in medicine to destroy tissue is often referred to as Focused Ultrasound Surgery (FUS). FUS conventionally works through the thermal ablation of tissue due to frictional effects at the microscopic level, induced by the rarefaction and compression phases of the ultrasound. This is, however, not the only effect induced that can create damage at the targeted area. If the dynamic pressure difference is high enough *cavitation* (see §2.2) can also occur in the region of the field.

In 1942, Lynn and Putnam successfully used ultrasound to destroy brain tissue in animals (as referenced by Evans *et al.* [39]). At 1949, which saw a peak in publications in the field, the early enthusiasm for ultrasound related cancer treatments was curbed. During a congress held in Erlangen, Germany, it was declared that there was a need for more fundamental studies of ultrasound, as a reliable treatment for cancer. The following decades saw a reduced level of interest in ultrasound as a therapeutic tool. In spite of this, the Fry brothers performed craniotomies in the 1950's, using high intensity ultrasound to destroy parts of the basal ganglia in patients with Parkinsonism (Fry [45]). Since then, the prospect of using ultrasound to treat tumours has remained a subject of research (Kennedy *et al.* [62]). Kremkau cites in his review (Kremkau [71]) that in 1956, Burov suggested the use of short bursts of high intensity ultrasound might also produce non-thermal anti-tumour effects. In Japan, many scientists followed the approach of Burov, reporting positive clinical experience for the treatment of thyroid and breast cancers. The first study of chemotherapy combined with ultrasound was reported in 1966 by Hill (as referenced by Kremkau [71]). In the early years of research in the field of therapeutic ultrasound for oncology, the results were contradictory. Three approaches were followed: (i) ultrasound alone was applied to the tumour, (ii) ultrasound was applied before, during or after x-ray treatment (iii) ultrasound was applied before or after administration of chemotherapy. The late 1960's delivered a slow revival of interest in ultrasound for treatment. Many studies were conducted to understand the relationship between sensitivity to electromagnetic radiation, and ultrasound. Tumour therapy with hyperthermia (an increase of temperature over natural levels) either alone, or in conjunction with radiotherapy, became a topic of interest (Wu [133]). The period between the early 1970's and the mid-1980's, was a phase of great expansion for diagnostic ultrasound, starting with bistable (binary) static,i culminating in gray-scale, real-time capabilities.

The capability of measuring and calibrating ultrasonic fields also improved

considerably over those years. This was possible with the development of better hydrophone devices. The invention of *PolyVinyliDene Fluoride* (PVDF), a piezoelectric polymer, made it possible to construct more sensitive and more accurate needle, or membrane, hydrophones.

A significant challenge to the use of HIFU for FUS was the difficulty in predicting the precise location of the treated area. This might be attributed in part to the wide range of responses of biological tissue to ultrasound, such as dependence of the speed of propagation on local temperature, propagation through layers of different tissue, and even inter-patient differences for the same tissue-type. During the 1970's and 1980's, the research in this field concentrated on: (i) identification of tissue parameters responsible for bioeffects, (ii) use of high power multi-element transducers (phased-arrays) possible due to the improvements in electronics, and (iii) visualization of the lesion after, or during, the treatment with ultrasonic imaging. An informative and detailed review of the issues faced in 1977, is given by Kremkau [71].

A prohibitive problem for research into ultrasound-induced bioeffects is, and was, a lack of measuring standards, for the comparison of independently conducted experiments. The main quantities used to describe the ultrasound parameters are: ultrasonic power, spatial-peak temporal-average intensity, and spatial-peak pulse-average intensity, as defined in table 2.1 (see 2.1.3) . In the 1990's, therapeutic ultrasound experienced something of a renaissance, with new technologies permitting researchers to obtain more convincing results (Kennedy *et al.* [62], ter Haar [114], ter Haar *et al.* [115]). A key advance was the introduction of guidance techniques, to target and confirm the exact location of treatment. Several systems that rely on Ultrasound-guided Focused Ultrasound Surgery (USgFUS) were developed at that time, and those principles remain in use today. There have been clinical trials for the treatment of prostate (Crawford and Barqawi [26], Gelet *et al.* [48], Misraï *et al.* [89]), bladder (Watkin and Ter Haar [129]), kidney (Illing *et al.* [61]), liver (Dick *et al.* [34], Wu *et al.* [134]), breast

(Wu *et al.* [135]), and bone (Wu *et al.* [134]), amongst other cancers. Significant work was performed in China using USgFUS, with tens of thousands of patients treated (Wu [132]).

The main disadvantage of this technology is that there is no direct monitoring of the energy delivered to the tissue. This means that the acoustic power administered is based on experimental data and theoretical modelling. The hyperechoic, i.e strong changes on B-mode (brightness mode) US-images, do not actually depict a temperature elevation, but reveal either the activity of acoustic cavitation or boiling. Cavitation during FUS is generally held to be a negative side effect, leading to unpredictable and rapidly developing lesions. The creation of cavitation disrupts the planned treatment, and can even produce unexpected heating effects (see §2.1.4), as discussed in detail by Coussios [24]. Boiling occurs when the applied acoustic energy is too high, and the temperature exceeds the planned temperatures of $60 - 80\,^{\circ}\mathrm{C}$. As for cavitation, this can lead to unnecessary damage of surrounding tissue, if not controlled. Therefore, there may be a possible mismatch in the locations between the hyperechoic changes and where the tissue is ablated (Kim *et al.* [65]). Guiding and monitoring with US-imaging is relatively economical (compared to Magnetic Resonance Imaging guidance technique described below), is completely real-time, and can simulate the HIFU beam propagation precisely, because diagnostic and therapeutic US waves share a similar modality. However, the drawbacks include relatively poor tissue-contrast, a limited field of view and a progressive deterioration of image quality as the treatment continues, due to changes in the treated tissue. These, combined with the inability to directly monitor the energy deposition, are the current limitations to USgFUS being the therapy-guidance modality of choice.

At the beginning of the 1990's, an important boost to HIFU in medicine was given by the introduction of *Magnetic Resonance Imaging* (MRI). This technology combination has since been called Magnetic Resonance-guided Focused Ultrasound Surgery (MRgFUS). There are two main factors that render the ad-

ministration of HIFU with MRI monitoring a very promising approach: (i) MRI images provide the most advanced imaging modality available for interventional radiology; (ii) MR-thermometry provides real-time feedback, allowing regulation of the applied acoustic energy. MR-thermometry utilises the temperature sensitivity of the water *proton resonance frequency*. A shift in the proton resonance frequency is linearly related to temperature and can be mapped rapidly with standard MR imaging sequences, using phase differences between images taken before and during FUS-treatment. However, conventional MR-thermometry is insensitive to temperature changes in fat, because in fatty tissue the water content is lower, and consequently the MR signal itself is low. It is also susceptible to motion artefacts, such as breathing, but also tissue-swelling which is more unpredictable. Consequently, the latter requires image subtraction, which increases treatment time and decreases precision. This technology is already used as a completely non-invasive surgery for the treatment of uterine fibroids, and for palliative care of bone metastasis. Currently, it is in development for primary malignant tumour treatment, with many clinical trials on-going (see §2.1.6). A difference between US- and MRI-guided systems is the ability to directly monitor the temperature with MRI thermometry. The MRIgFUS technique therefore requires a MRI operator and MRI compatible components, making these systems significantly more expensive, both to acquire and operate. Although MR-guidance sets the gold standard for FUS procedures, it can be prohibitively expensive for wide spread clinical use. As such, USgFUS approaches, which are more economical, remain a viable clinical option.

Several other potential therapeutic applications of HIFU are being investigated, including thrombolysis (clot dissolution), embolization (arterial occlusion) for the treatment of tumours, haemostasis of bleeding vessels and organs, drug and gene delivery. In recent years, particularly the treatment of brain disorders have had hugely encouraging results (see §2.1.6).

2.1.3 Significant ultrasound parameters

In this section, the principle parameters for biomedical applications of ultrasound, particularly HIFU, will be introduced. In practise, parameters are selected according to the application and desired bioeffects.

For ultrasound imaging, the wavelength, λ, of the ultrasound wave is a crucial parameter, as it relates to the spatial resolution that may be achieved. Wavelength is related to frequency through $f = c/\lambda$, where c is the speed of sound. In most cases, the speed of sound in tissue is approximated to the speed of sound in water. Frequency is a critical value, because it is responsible for both resolution and penetration depth. Fundamental physics dictate that higher frequencies permit higher resolution images, through the *diffraction limit*, however higher frequencies are also subject to higher levels of attenuation. The attenuated amplitude, A, depends on the frequency, f, used, and follows an exponential law, given by:

$$A = A_0 e^{\alpha(f)} \tag{2.1}$$

where A_0 is the amplitude at source and $\alpha(f)$ is an attenuation coefficient which is frequency dependent, and quite variable, even in tissues of the same type. Frequency selection is therefore a trade-off between resolution and depth of imaging. For therapeutic applications, the treatment (focal) volume is similarly related to the frequency of the HIFU applied, via the diffraction limit. The dimensions of the focus are calculated measuring the full width at half maximum (FWHM) from peak intensity value within the focus, along the propagation axis (see §3.3.2). The geometry of the ultrasound source also determines the size and shape of the focus. In §2.1.6, a few examples of transducer designs, in relation to their applications, are described.

To define the effect that ultrasound has in biology or medicine, some key quantities have been defined. Generally, these are divided into first and second order (O'Brien [97]). First order quantities are amplitude-based, and second order

quantities energy-based. The amplitude of the pressure wave, for the purpose of this thesis, is measured in 10^6 Pascal (MPa). The peak negative pressure (PNP) is the pressure in the rarefactional phase, to which the medium is exposed during the passage of the mechanical wave. Amplitude and its second order derivatives are the main adjustable parameters for therapeutic ultrasound. Ultrasound travelling through a medium creates a dynamic pressure field, which can be spatially calibrated with a hydrophone, which detects the pressure amplitude at the point at which the active element is located. Scanning of the hydrophone across the HIFU field, produces a *pressure map*, which can be used to calculate the acoustic power and intensity of the ultrasound field. These are the second order quantities which encompass amplitude (pressure), the medium of propagation and distribution of the focus. These types of quantities express energy transport. In the case of a planar wave, the intensity scales as the square of the pressure amplitude. Various types of intensity are used according to the exposure conditions, summarized in table 2.1.

The propagation of waves in a certain material is dependent on three main factors: speed in the medium, c_0, impedance, Z_0, and attenuation coefficient, $\alpha(f)$). The speed of sound propagation depends upon which medium the sound is travelling through and is temperature dependent. For example, sound waves in air travel at a speed of 346 m/s, and in water at 1497 m/s, at room temperature. The acoustic speed, c_0, in a medium is determined by its mechanical properties: $c_0 = \sqrt{\frac{B_{AD}}{\rho_0}}$, for an isotropic (uniform in all directions) fluid, where B_{AD} is the adiabatic bulk modulus and ρ_0 is the density of the medium. Often denser materials are stiffer (much higher B_{AD}) and the speed of sound is faster in such materials. The specific acoustic impedance ($Z_0 = \rho_0 c_0$) is directly proportional to density and acoustic speed.

Ultrasound waves can also be administered in one of two modes, dependent on the application: continuous wave (CW) or pulsed wave (PW) mode . In the case of pulsed operation, duty cycle (DC) is a parameter used to describe the

Table 2.1: Spatial and temporal dependent intensity representations according to HIFU administration modes

Symbol	Formula	Summary
$\boldsymbol{I}$	$\frac{p^2}{\rho c}$	Instantaneous Intensity
$\boldsymbol{I_{pi}}$	$\frac{p_i}{\rho c}$	Pulse-Intensity Integral
$\boldsymbol{I_{ta}}$	$\boldsymbol{I_{pi}/PRF}$	Temporal-Average Intensity
$\boldsymbol{I_{sptp}}$	-	Spatial-Peak Temporal-Peak Intensity
$\boldsymbol{I_{sppa}}$	-	Spatial-Peak Pulse-Average Intensity
$\boldsymbol{I_{spta}}$	-	Spatial-Peak Temporal-Average Intensity
$\boldsymbol{I_{sa}}$	$\int \boldsymbol{I_{ta}}\,\mathrm{d}\boldsymbol{A}$	Spatial-Average Intensity
$\boldsymbol{I_{sata}}$	$\int \boldsymbol{I_{ta}}\,\mathrm{d}\boldsymbol{A}/\int \mathrm{d}\boldsymbol{A}$	Spatial-Average Temporal-Average Intensity

ratio of 'on time' to 'total time', $DC = \tau PRF$, where $\tau = N/f$. N is the number of cycles per pulse and PRF the pulse repetition frequency.

To summarise, the most common ultrasound parameters are: amplitude (which determines intensity), frequency which is mainly hardware dependent; the medium characteristics (acoustic impedance and speed of sound); and finally, if the mode of operation is PW, the PRF and DC.

2.1.4 Ultrasound bioeffects

The exposure of tissue to ultrasound, of any intensity, will induce a range of *bioeffects*. Here, the pertinent bioeffects associated with HIFU are reviewed.

Thermal effects Ultrasound propagating through a medium is attenuated by two main effects: absorption and scattering. Some of the incident ultrasound is reflected from changes in the structure, such as a transition from one material to another. The degree of reflection depends on the difference in acoustic impedance between the different regions. Diagnostic applications of ultrasound are based on this principle. Energy which is absorbed by the medium is transformed into heat (Kennedy *et al.* [62]), via viscous frictional effects. In the case of FUS, this is a desirable effect used to mediate ablation of targeted tissue. If heat is generated more rapidly than it can be dissipated, by conduction and circulation in

the vasculature, a temperature rise will result. These thermal mechanisms are well understood for tissue and can be predicted using mathematical modelling techniques. Cells in tissue will only survive within a narrow range of temperatures. Above ~ 45°C, enzymes denature, which ultimately kills the cell (known as necrosis). The extent of this effect also depends on the duration of temperature elevation, i.e. long exposure at a moderately increased temperature, or shorter exposures at higher temperatures. To calculate an isoeffect on the cells, it is possible to use an empirical formula to calculate a normalized time, t_{43}, at the location of the maximum pulse depended on exposure time, t, intensity necessary for thermal damage:

$$t_{43} = tR_{TI}^{(43-T)} \tag{2.2}$$

where R_{TI} is the thermal index constant, with common values used of 0.5 above 43 °C, and 0.25 below 43 °C. T the temperature of the medium (37 °C for tissue). From eq. 2.2, it is possible to calculate the thermal dose that a tissue receives during an ultrasound exposure. A common way to determine the heating effects of ultrasound is the Thermal Index (TI) , which is defined by:

$$TI = \frac{W_0}{W_{DEG}} \tag{2.3}$$

where W_0 is the source power and W_{DEG} the power needed to increase the temperature by 1 °C.

Non-thermal effects The propagation of a pressure wave also induces mechanical (non-thermal) effects in a host medium, including tissues. The most significant of these, for ultrasound at therapeutic intensities, is cavitation. Others include acoustic radiation force and streaming. All have been studied in relation to biological tissues, but are still not well understood (O'Brien [96]).

A predictive index for non-thermal effects, equivalent to TI for thermal effects, has been developed to anticipate the likelihood of cavitation in tissue from a given

ultrasound exposure (Abbott [1], Holland *et al.* [58]).

The Mechanical Index (MI) is defined by the following formula:

$$MI = \frac{PNP \times C_{MI}}{\sqrt{f_c}}. \tag{2.4}$$

MI is a dimensionless parameter in which peak negative pressure (PNP in MPa) is attenuated in homogeneous tissue, using a derating factor, C_{MI}, of 0.3 dB/cm/MHz as a measure of energy dissipation at the location of the maximum pulse intensity integral, I_{pi}, and f_c denotes the centre frequency (in MHz), which is the arithmetic average f_c, of the frequencies f_1 and f_2, defined as the bandwidth of the acoustic wave. This index indicates the likelihood of cavitation occurring in tissue or degassed water for given ultrasound exposure. It is evident from eq. 2.4 that the probability of cavitation increases with decreasing frequency, and intuitively, with increasing pressure amplitude. The MI does not address the extent of the bioeffects whose threshold it predicts. MI also does not account for previous ultrasound exposures, as in the case for PW mode. Moreover there might be some mechanical effects due to the positive pressure phases which are unaccounted for. The safety threshold for MI is still an open topic. It is generally held that an MI of above 0.4 will elicit some mechanical bioeffects (ter Haar [116]) and that for an MI = 0.7 there is a significant probability of cavitation occurring. It was demonstrated that an MI = 0.9 resulted in extensive damage to the lungs of rats (Holland *et al.* [58]). These are typical values used during Doppler imaging of blood flow, one of the most energetic of the diagnostic settings. It is interesting to note that the Food and Drug Administration (FDA) safety limit is much higher, at MI = 1.9. This assumes that precautions, such as short scans and avoidance of lungs, are taken to render the negative effects of ultrasound negligible. However, it should be noted that this advice is based on ultrasound knowledge and device specification from 1976.

Radiation force The acoustic radiation force, F_r, or radiation pressure, is in effect a transfer of momentum between an acoustic wave and an exposed object (Lee and Wang [78]). For ultrasound incident on an absorbing rigid surface, the force is described by a simple formula:

$$F_r = W_{ac}/c \tag{2.5}$$

which equates the acoustic power, W_{ac}, to a force. Accordingly, if an absorbing material is immersed in a fluid which has a certain speed of sound, c, then a force will act upon the material in the direction of the ultrasound propagation. If the material is a reflector, the eq. 2.5 should be doubled, as the momentum is not simply absorbed, but reversed (Kino [66]). In the literature, many examples are described which demonstrate the macroscopic effects of the acoustical radiation force, for example on simple spheres (Hasegawa and Yosioka [55], Yoisioka and Kawasima [140]), and on bubbles (Lee [77]). For a more detailed account of the action of acoustic-forces on bubbles, see §2.2.4. It is also possible to create complex patterns in order to manipulate objects for a desired purpose (Demore *et al.* [33]). It has been shown that radiation forces act on microscopic objects, such as cells (Wang *et al.* [125]). Moreover, by producing standing waves, it is possible to create an acoustic potential landscape that can be used to separate cells or other particles in biology (Thalhammer *et al.* [118]).

Radiation force can be used to locally move or vibrate tissue. This effect forms the basis of a new application relevant to MRgFUS, called *acoustic radiation force impulse imaging* (ARFI). Here, a short pulse of focused ultrasound is used to physically move tissue. The displacement, on the order of micrometers, can be used to identify the true position of the HIFU focus, prior to the actual treatment. Possible bioeffects related to the action of the radiation force on biological tissue are still not fully investigated.

Acoustic streaming Acoustic streaming, also known as the as *quartz wind*, is a phenomenon that occurs due to the same principles described previously for radiation force. In essence, it is the transfer of momentum to a liquid, which generates local fluid motion, induced by absorption of acoustic energy. Extending eq. 2.5, it is possible to obtain an expression for the flow along the axis of the beam applied to the liquid.

$$U_0 = \alpha W_{ac} \Phi / \pi \eta c \tag{2.6}$$

where W_{ac} is the total power in the beam, η is the shear viscosity for the liquid and Φ is a function of the beam and the diameter of the containing vessel or tube. It has been noted that streaming is circa 30 times stronger in blood than in water, or similar liquids such as urine or amniotic liquid, because of increased ultrasonic absorption by the red blood cells (NIH-PA [94], Nyborg [95]).

Another type of streaming is microstreaming, or boundary-layer streaming, which occurs near a small vibrating cylinder or sphere. Microstreaming is thought to be one of the mechanisms by which cell membrane permeability increases on ultrasound exposure, an effect often termed *sonoporation* (see 2.2.5), (Delalande *et al.* [31], van Wamel *et al.* [122], WU *et al.* [137]). It was shown that sonoporation is drastically enhanced by the introduction of artificial bubbles (Delalande *et al.* [32]), which promotes microstreaming in the vicinity of the membrane (Barnett *et al.* [3], Manasseh *et al.* [82], Marmottant and Hilgenfeldt [83], Wu and Nyborg [138]).

2.1.5 Non-linearity of ultrasound in medicine

The developments in the field of therapeutic ultrasound have largely been made based on the convenient assumption of linear acoustics. However, this can be invalid at the frequencies and amplitudes used in high intensity applications. The following assumptions are now known to be incorrect: (i) only one frequency

propagates into the medium, and (ii) raising the source, A_0 amplitude raises the field amplitude, A by an equivalent amount, at remote points in the medium. The generally assumed linearity of acoustic pressure, p with excess density, ρ is only an approximation valid at infinitesimal amplitudes (Duck [37]).

The localized pressure changes of the wave imposes an asymmetry in the propagation speed for the component phases within the wave itself. The propagation speed is higher for the positive pressure, compressional phase of the oscillation, than the low pressure, rarefactional phase. The higher the pressure amplitudes, the greater the discrepancy between the speeds of propagation. An initially plane monochromatic sinusoidal wave of single frequency, will adopt a saw-tooth profile when propagating non-linearly, which increases at higher intensity, see fig. 2.2 (a). One consequence of such a distorted waveform is the addition of new frequency components to the spectrum of the wave, see fig. 2.2.

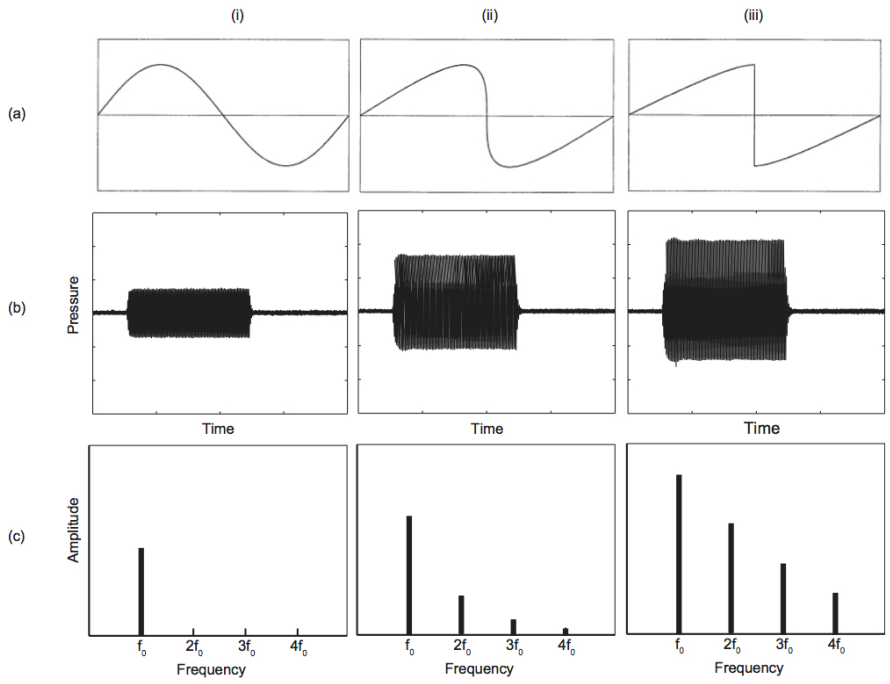

Figure 2.2: Waveforms and spectra for ultrasound of varying non-linearity - (a) (i-iii) waveforms of increasing non-linearity exhibiting increasing saw-tooth characteristic. (b) (i-iii) typical hydrophone recording demonstrating the difference in positive pressure and negative pressure amplitudes, for an increasing degree of non-linearity. (c) (i-iii) typical spectra revealing higher harmonic components, obtained via Fourier transform of (b)

It is therefore possible to assess the degree of non-linearity through a frequency analysis of the signal. A Fourier analysis describes this effectively; whereby every signal can be represented by a sum of sinusoidal waves. In the case of the non-linear HIFU, the higher harmonic components have frequencies that are multiples of the fundamental frequency, given by $2f_0$, $3f_0$, etc., where f_0 is the frequency of the original waveform emitted by the transducer. A more accurate description of the non-linearity is possible through a series expansion:

$$p = c\rho + 1/2\frac{c^2}{\rho}(\frac{B}{A})\rho^2 + ... \tag{2.7}$$

c is the sound speed, ρ static density, and B/A the second order parameter of non-linearity. This value describes the extent to which the medium is affected by non-linear effects, in a certain thermodynamic state. A value of 5.2 for B/A is reported for water at 30 °C at atmospheric pressure, *'Non-linear acoustics'*, by Beyer [6]. For comparison this value is quite variable in tissue: B/A ranges for non-fat soft tissue from 6.3 to 8.0 and for fat soft tissue from 9.6 to 11.3 (Duck [37]).

Since absorption of ultrasound increases with frequency, eq. 2.1 (see §2.1.3), higher harmonics are therefore rapidly attenuated, and can be effectively disregarded for low intensity applications. While absorption of sound in air has been investigated since the 1930's, the first results for water were presented by Fox and Wallace [43] and Krassilnikov *et al.* [70], in 1954 and 1957, respectively. Krasilnikov measured the harmonic content of an ultrasound beam of 1.5 MHz, in water. The second harmonic component was measured at different distances from the transducer, at three different intensities, as shown in fig. 2.3. These experiments were performed using piezoelectric plates as receivers. Another technique used to analyse frequency components is the Debye-Sears method, based on a similar principle to Schlieren imaging, or modern fibre-optic hydrophones (see §3.4).

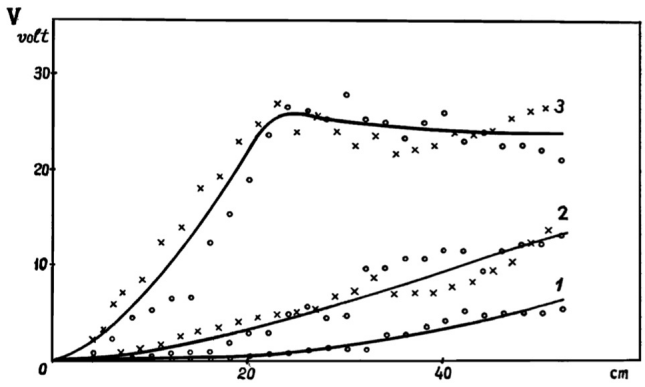

Figure 2.3: Dependence of the second harmonic amplitude with distance, for three pressure amplitudes - The second harmonic is detected over a range of distances from the source, driven at fundamental amplitudes of: 125 kPa (1), 240 kPa (2), and 500 kPa (3). From Krasilnikov *et al.* [70]

2.1.6 FUS: applications and devices

In this section, various hardware configurations for particular applications will be introduced. The aim is to illustrate how it is necessary to use different approaches acccording to the anatomy local to the targeted organ. Using HIFU to destroy pathologic tissue, with distinct advantage of minimising side effects and invasiveness, is common to all applications.

FUS employs HIFU at intensities in the range of $I_{sa} = 100 - 10000 W/cm^2$ (see table 2.1). Both mechanical and thermal effects can occur in most applications. (see §2.1.4). The most common mechanical effect is cavitation and the classic thermal effect is heating, due to absorption. The geometry of the heated/ablated area is often described as cigar-shaped, matching the focal volume of the HIFU field. Depending on the transducer frequency-of-operation (see §2.1.3), the size can range from a few millimetres at higher frequencies, up to a couple of centimetres for low frequency treatments. There are two types of devices: extracorporeal or transrectal according to their application. The design of the transducer is

therefore largely determined by the application, taking into account factors such as how deep-seated the pathology, amongst other anatomical considerations. In the following section, particular applications of FUS will be described, and the device used for each application will be introduced.

Uterine fibroid the uterus was identified as a good target for FUS treatments as it is static and located close to the abdominal wall. Uterine leiomyomas are bulky tumorous masses, which can be treated with less ethical concerns, due to the benign nature. Two MRgFUS devices exist; the Philips (Sonalleve® MR-HIFU), InSightec Ltd. (ExAblate® 2000) systems, and an USgFUS device, mostly used in China, produced by Chonqinq Haifu Technology Ltd. (Kim *et al.* [65]). The transducers used for the MRI-guided versions are multi-element phased arrays. These arrays are geometrically focused and are comprised of many hundreds of elements. Some of the elements can be used as passive cavitation detectors. The advantage of using electronically controlled multi-element transducers is that they allow active beam steering, over and above mechanical manipulation of the transducer itself. For the treatment of a bulky tumour such as a uterine fibroid which can be several centimetres in size or more, electronic steering allows the transducer to be fixed through out the procedure. Multi-element transducers also allow ultrasonically sensitive 'obstacles' to be avoided, such as bowel walls, bones, and nerves.

The competing clinical procedures to MRgFUS for uterine fibroids are hysterectomy and uterine artery embolisation (UAE). Both of these compromise fertility and carry the risks associated with invasive surgery, and so MRgFUS offers an attractive (albeit expensive) treatment option.

Bone metastasis is the only malignant tumour for which commercial FUS systems are used, for palliative treatment purposes. During a procedure HIFU is focused on or behind the bone. The high density, and therefore high acoustic absorption coefficient (see §2.1.4), of the bone cortex facilitates high temperatures

being rapidly achieved. The nerves responsible for the pain are thus quickly destroyed, mediating the desired effect of reducing the painful symptoms associated with the disease. The InSightec Ltd. system (ExAblate® bone system) employs a transducer which can be positioned in most locations around the body, for strapping onto the patient. The HIFU source is is not built into the MRI table and is not geometrically focused. The targeting can be achieved with phasing control of the 1000 element transducer. Other vendors are in the process of developing devices capable of offering this kind of treatment: Sonalleve® MR-HIFU by Philips and Model JC®, by Chongqing Haifu Technology Ltd.

Prostate high-frequency probes around 3MHz are inserted transrectally, thereby allowing very precise targeting with a tightly focused HIFU beam (see §2.1.3). Furthermore, from this transducer position it is possible to achieve good coupling of the HIFU beam to the target organ. The high-frequency employed also means the transducer is relatively small compared to the other FUS-application transducers. There are two widely used USgFUS clinical devices, manufactured by companies in France (Ablatherm® HIFU system; EDAP) and the United States (Sonablate® Inc.,). FUS can be used for two separate clinical conditions: benign prostatic hyperplasia (BPH) and carcinoma of the prostate (CaP) (Warmuth *et al.* [128]). Two MRgFUS sytstems are available, namely ExAblate® (InSightec Ltd.) and Profound® Trans-urethral system (Profound Medical Inc.).

Brain the pre-conception that bone is completely opaque to ultrasound is not entirely correct. At low enough frequencies (220 kHz and 650 kHz, ExAblate® Neuro, InSightec Ltd.) sufficient ultrasound can be transmitted across the skull. Recently, the first clinical trials in humans for palliative control of neuropathic pain (Martin *et al.* [86]) and Essential Tremor have delivered very promising results. High levels of energy deposition can cause excessive heating. Cooling systems that circulate chilled water around the scalp contribute to heat dissipation, created at the bone interface. Another challenge for transcranial FUS

therapy is strong aberration of incident HIFU waves that compromises the focus, due to the irregular thickness and local geometry of the skull. To overcome these problems, a hemispherical source is used, bearing some resemblance to a helmet, partially encloses the head, see fig. 2.4. The large surface area reduces local heat accumulation, thereby maintaining reasonable energy transmission. To minimize the defocusing problem, a multi-element phased array source is used, in conjunction with CT-scans of the skull (Marquet *et al.* [85]). In this manner, compensation for the strong aberrations can be applied to reform the focus at the desired position.

A particularly exiting facet of the brain-FUS application is the selective opening of the blood brain barrier (BBB) without damage to the normal neuronal tissue, which has been demonstrated on primate models (Tung *et al.* [121]). Microbubbles delivered intravascolary are critical to mediating the BBB permeabilisation. Moreover, the low frequencies required to traverse the skull, means cavitation is a likely occurrence (see §2.1.4).

Figure 2.4: MRI guided brain FUS - Multiphased High intensity focused ultrasound device for brain applications. The device is positioned on a patient. Here pre-treatment position. Image from InSightec Ltd.

Liver tumours were an early target for animal experiments dating from the 1970's. More recently, Wu *et al.* [136] published data demonstrating that a tumour subject to FUS and subsequently excised, was totally ablated. Many treatments are also performed in China, with the Chongqing HAIFU JC® device (Chongqing HAIFU), although follow-up to these treatments remain incomplete. A major technological challenge to liver-FUS treatments is tissue motion due to breathing. Currently 'breath-holding' techniques are used for patient trials. Competitive minimally-invasive techniques include cryotherapy, arterial embolisation, percutaneous alcohol ablation and either percutaneous or laparoscopic radiofrequency (rf) ablation.

Hemostasis bleeding cessation can be obtained with HIFU in the range of $I_{sa} = 500 - 3000 W/cm^2$. The application is targeted specifically to emergency situations and was primarily developed to control injuries in the battlefield. Structural deformation of the bulk tissue of a solid organ, due to temperature elevation, induces collapse of small vessels and sinusoids (capillary-type blood vessel supplying the endothelium) or sinusoid-like structures. Heat also causes coagulation of the outermost layer of vessels, and subsequently, fibrin-plug formation. The mechanical effect of acoustic cavitation also appears to play a minor role in haemostasis.

Thrombolysis or the dissolution of a blood clot, can result from ultrasound exposure, which has significant potential for the treatment of stroke. It is achieved with low intensities ($I_{sa} = 0.5 - 1 W/cm^2$) and is known to be connected to non-thermal effects (O'Brien [97]). Microstreaming (see §2.1.4) by cavitation is thought to increase the efficiency of thrombolytic agents and/or attack the integrity of the surface of the thrombus itself (Frenkel *et al.* [44]). These treatments can be done with an extracorporeal transducer or a miniaturized transducer on the tip of catheter, such as EndoWave® Pheripheral Infusion System (EKOS Co.).

2.2 Cavitation

New Oxford American Dictionary 3rd edition 2010 by Oxford University Press, Inc.[19]

Cav•i•ta•tion *(noun Physics):|kavə'tāSHən|*

The formation of an empty space within a solid object or body; the formation of bubbles in a liquid, typically by the movement of a propeller through it.

The literal meaning of the word *cavitation* derives from cavity or empty space. It will be shown that the term describes a broad range of situation were bi-phase gas-liquid interface is involved. Generally, it can be said that when the pressure and/or temperature of a liquid is changed, the thermodynamic state of the liquid changes too. With a reduction in pressure, and an increase in temperature, the liquid approaches a gaseous state. For instance, if water is heated at constant pressure, a state is reached through which the growth of vapour filled bubbles occurs. This state is commonly called *boiling* and is represented by the horizontal (adiabatic process) arrow in fig. 2.5.

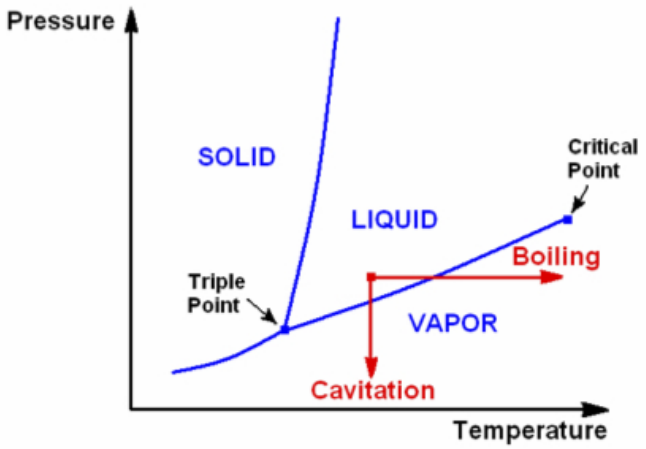

Figure 2.5: Phase diagram - for a 'simple' substance like water, where the blue line between the triple point and the critical point is the saturated vapour/liquid line. After Brennen [11]

In contrast, cavitation occurs when the pressure is reduced and the temperature maintained as constant, for which the separation between the liquid and the gaseous state is achieved following the vertical arrow (isothermal process) on the

same diagram. It can therefore be concluded that thermodynamically, boiling and cavitation are equivalent, the only effective difference being the path taken to cross the phase-transition line. In practice, changing the temperature of a liquid in a homogeneous fashion is very difficult, and typically during boiling the bubble source occurs at boundaries which are the source of heat, i.e. the bottom of pot on a stove.

The propeller of a ship, rotating through water can create localised drops in pressure, required for cavitation formation. Similarly ultrasound imposes local pressure reductions on the medium through which it propagates, and can therefore also cause cavitation (see §2.2.2).

2.2.1 History of cavitation research

The interest in cavitation dates back to the first reports on the corrosion of ship propellers, at the end of the 19th Century. In 1894, the British torpedo-boat destroyer 'HMS Daring' achieved a top speed of 24 knots despite a theoretically anticipated 27 knots. Barnaby's investigation of the problem led him to conclude that there was a limit to the propeller speed, related to the maximum tensile strength of the water, beyond which a breakdown of the propeller inflow occurs. Froude proposed the term "*Cavitation*" for this phenomenon, derived from the Latin word "*cavus, -a, -um*" ("*hollow*"). Between 1908 and 1924, cavitation studies became fundamental to the design and testing of propellers for fast boats. In order to study the phenomenon in greater detail, *cavitation tunnels* were constructed, which facilitated the first photographic observation of cavitation, in 1911, fig. 2.6 (as referenced by Weitendorf [130]).

These experiments, however, were not able to address the central question of how cavitation was actually corroding the surface. It was generally thought that the collapse of each single bubble was contributing to the corrosion damage. In 1917, Lord Rayleigh published, *'The Theory of Sound'* (Rayleigh [107]), which was the first theoretical work describing the phenomenon. Lord Rayleigh's core

equations are still used as a basis for single bubble studies. He derived the time for collapse, τ_c, of an empty cavity, related to the radius of the bubble at maximum expansion, R_{max}, as:

$$\tau_c = 0.91468 \times R_{max}\sqrt{\frac{\rho}{p_0}} \tag{2.8}$$

where ρ is the density of the medium and p_0 the ambient pressure.

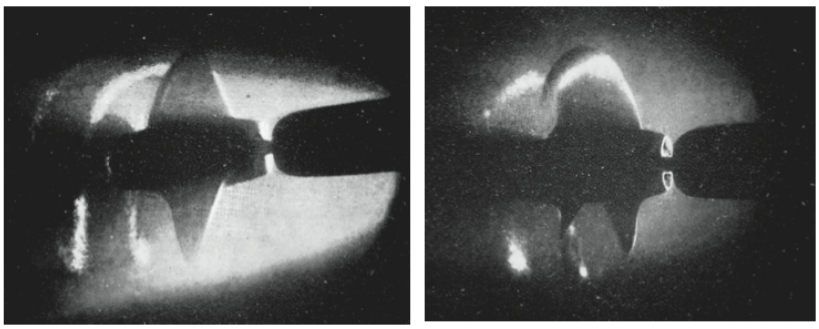

Figure 2.6: Historic photographs in cavitation tunnel - One of the first propeller cavitation photographs from Parsons first tunnel (1895). After Weitendorf [130]

In 1930, Ackeret (as referenced by Weitendorf [130]) measured five different pressure profiles and showed that for cavitating conditions, there is a linear proportionality between static peak pressure, minus vapour pressure, and the dynamic peak pressure of the inflow. These measurements, and simultaneous cavitation observations, lead to the realisation that cavitation inception occurs at interfaces, when the sum of static pressure, p_0, and maximum suction pressure, -p_{min}, is equal to the vapour pressure , p_v, for a given temperature.

It became fundamentally important to distinguish the behaviour of a single bubble, to better understand the corrosive effects of cavitation as an entity. For this purpose, bubbles were created with electrically induced sparks, from electrodes immersed in liquids. This single bubble approach led to the confirmation of cavity behaviours such as *jet-formation* and individuals collapse times (see eq. 2.8). The spark technique had one main disadvantage; the presence of the electrodes in a vicinity of the bubble. A new single-bubble technique circumvented this problem, with the invention of the laser in 1960.

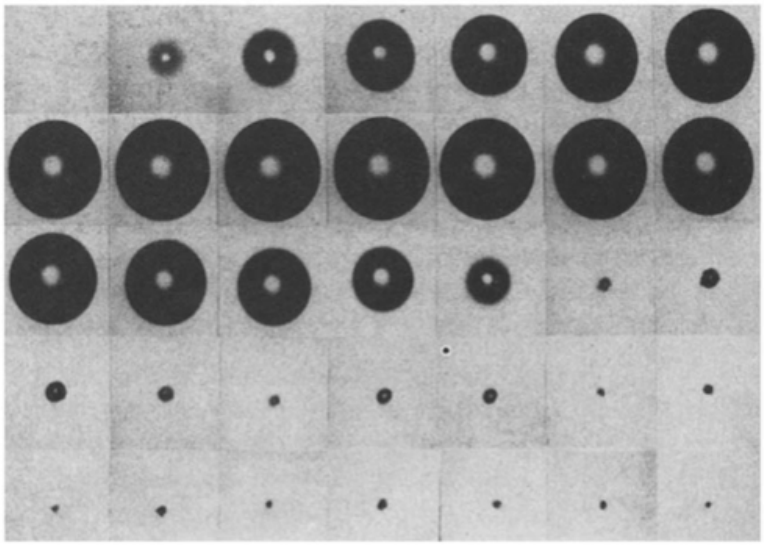

Figure 2.7: Laser-induced cavity (LIC) - Focusing a laser pulse into a host medium generates an undisturbed single spherical bubble. Here, maximum bubble diameter is 2.65 mm recorded with an imaging rate of 75000 fps (frames per second). (From Lauterborn [74])

Laser-induced cavitation through optical breakdown occurs when a pulsed-laser is tightly focused into an optically transparent medium. The initial experiments on optical breakdown consisted of the detection of acoustic transients and shockwaves propagating through liquids (Bell [4], Carome [15], Carome *et al.* [16, 17], Felix and Ellis [41], Fujimoto *et al.* [47]). In 1974, Lauterborn and Bolle were the first to use a high-speed camera to observe LIC's generated with a nanosecond Q-switched ruby laser (Lauterborn and Bolle [74]).

The pulsed-laser technique has the same advantage of the spark technique, in terms of temporal and spatial positioning of a single bubble, but without the disturbance of electrodes in the locale. A significant advantage of the laser method, compared to the spark method, is that that it can produce extremely smooth spherical bubbles, fig. 2.7. The disadvantage common to both methods, is that they involve intense local heating and vaporization of the liquid, which does not occur in hydrodynamic or acoustic cavitation processes. Cavitation models based on such observations, must therefore take this into account (Krasovitsky *et al.* [69]).

Optical breakdown through absorption of laser radiation, dielectric break-

down or laser-induced breakdown, involves the partial or complete ionisation of a solid, liquid or gas, at the location of absorption. The ionisation results in a plasma, which absorbs optical radiation much more strongly than the other states-of-matter. The plasma is thus rapidly heated by the laser radiation to very high temperatures, driving rapid plasma expansion, optical and acoustic emissions. This can be seen in fig. 2.8, where optical breakdown produces an intense emission of light, followed by a shock-wave, which radiates out into the host medium. For a more detailed account of the mechanism, see Kennedy [63].

Figure 2.8: Optical plasma emission and shock-wave generation - Bubble generation and shock wave emission upon laser-induced breakdown caused by a focused Nd:YAG laser pulse in water. From Ohl [98].

Almost any laser which can emit short pulses, with durations of the order of a few nanoseconds or less, and pulse energies of a few mJ, can be used. It is also possible to use shorter laser pulses to induce different shapes of LIC, such as elliptical bubbles from femtosecond pulses (Vogel *et al.* [123]). This technique has made the study of single cavities much easier, and has finally allowed single bubbles in specific fluidity environment to be studied, in great detail. A detailed review on formation of jets and more recent studies of corrosion, can be found in §4.4.1.

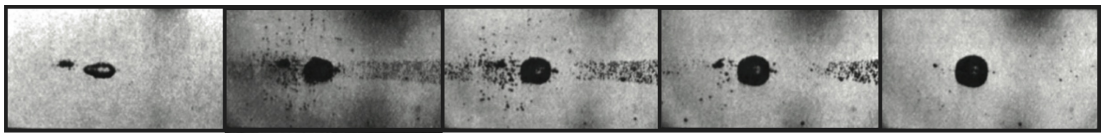

Figure 2.9: Laser-induced bubble at reduced pressure - Laser-induced bubble in water at reduced static pressure of 53kPa. Interframe time 167 ns (After Lauterborn [76], where interframe time is stated 167 μs)

In fig. 2.9 a focused laser beam is used to create a laser-induced cavity (Lauterborn and Kurz [76]), as described above. In this particular experiment, an under-pressure of 53 kPa decompresses the water. In the first frame, only the cavity produced by the optical breakdown is apparent. In subsequent frames, other much smaller bubbles form, due to the combination of the under-pressure and the passage of the shock-wave produced on laser absorption. This observation forms the basis for the *laser-nucleation technique* investigated in Chapters 3 and 4.

Specifically, fig. 2.9 suggests that acoustic cavitation bubbles can be generated along the optical path of pulsed laser-radiation, in a medium exposed to the pressure fluctuations of propagating acoustic transients. The hypothesis underpinning the current work is that purely acoustic cavitation could be *laser-nucleated* (to distinguish from laser-induced) in an established focused ultrasound field. Crucially, however, for the study of acoustic cavitation the large plasma mediated bubble must be avoided. As discussed in Chapters 3 and 4, this is achieved by administering laser-pulses at *below the breakdown energy threshold*, in a pre-existing HIFU field.

2.2.2 Acoustic Cavitation

Acoustic cavitation is generally understood to be the phenomenon of bubble formation occurring in relation to periodic pressure changes, rather than to sustained (static) pressure events (Brennen [12]). Boyle and others (as referenced by O'Brien [96]) in the 1920's were probably the first to identify *acoustic cavitation* in water, as produced by high intensity ultrasound. At sufficiently high intensities, ultrasound travelling through a medium, can reduce the local pressure below vapour pressure levels (see fig. 2.5), at which point cavitation occurs. The bubbles that result are *gaseous cavities* due to *degassing* of the host medium, to distinguish it from *vaporous cavities* in the case of the laser-induced cavities discussed previously. Moreover, when bubbles are present in an ultrasound field,

they are forced to react to the pressure changes imposed upon them by the ultrasound.

To minimize the surface energy, gas pockets tend to aggregate as spherical bubbles. The size of the bubble is fundamental to its behaviour in response to ultrasound of a given frequency. The wavelength dictates a resonance condition for the size of bubble that will have the strongest interaction with the field. The 'natural' oscillation frequency, f_r, of a spherical gas bubble of equilibrium radius R_0, can be approximated by the Minnaert equation:

$$f_r = 1/R_0\sqrt{\frac{3\gamma p_0}{\rho}} \tag{2.9}$$

where γ is the polytropic exponent, p_0 the ambient pressure and ρ the density (Akhatov *et al.* [2]). In the case of an air bubble in water, of $R_0 > 5\ \mu m$, this reduces to (Coussios *et al.* [24], Leighton *et al.* [81]):

$$f_r \cong 3/R_0. \tag{2.10}$$

Stable vs transient cavitation Flynn was the first to distinguished between *stable* (*non-inertial*) cavitation and *transient* (*inertial*) cavitation (as referenced by Leighton [80]). Stable cavitation refers to a less energetic dynamic, whereby bubbles pulsate around an equilibrium radius R_0 over many acoustic cycles. Transient cavitation is associated with violent collapses, typically occurring in high-intensity ultrasound.

Flynn analysed the energetics of transient collapses, through consideration of the mechanical work done on the cavity by the spherical convergence of the liquid, and the dissipation of energy during the collapse process. If the acoustic pressure is great enough for the liquid to go into tension during the negative half-cycle, cavities will expand rapidly, often to many times their original size. Following this, on the compression half-cycle, they collapse violently or 'implode', often breaking up into many smaller bubbles. This happens when the inertia abruptly

overcomes the weaker forces of surface tension and internal pressure. It is during this collapse phase that most of the disruptive effects of transient cavitation occur. The high energies imposed on the bubble often cause non-linear effects, such as heat production and broadband acoustic emissions. During non-inertial cavitation these implosions do not occur. The bubbles simply respond linearly to the external pressure fluctuations.

Acoustic cavitation emissions detection of the acoustic signals emitted by bubbles, driven by ultrasound, is a common technique used to characterise bubble response. This is especially useful for the case of an optically turbid host medium, through which bubble dynamics cannot be observed directly. Bubbles act as secondary point sources of sound, each emitting or scattering radially. If the bubbles are driven at comparatively lower powers, they pulsate in linear fashion around the equilibrium radius, R_0. Experimentally, it has been demonstrated that in such a stable regime, only the driving frequency, f_0, will be detected within the emitted signal (Lauterborn and Kurz [76]). At higher intensities, but still below the transient threshold, the bubbles begin to oscillate with a degree of non-linearty. The bubbles then start emitting $f_e = 2f_0$, where f_e is the emitted frequency of the acoustic signal from the bubble. Early experiments, reviewed by Neppiras [91] showed that emissions at $f_e = f_0/2$ can appear intermittently. With increasing pressure amplitudes, other ultra- and sub-harmonics emerge. Some of the harmonic content can be attributed to the inherent non-linearity of the medium (see §2.1.5). The harmonics originating from the non-linearity of the medium are, restricted to higher harmonics ($f = nf_0$) with n = 1, 2, 3, etc. Stable cavitation is therefore, in practice, detected through monitoring for $f_e = f_0/2$. One explanation by Neppiras [91] for the origin for sub-harmonics signal, is the presence of a form of periodic unstable oscillation of a bubble, driven at twice its resonance.

At high pressure amplitudes, white noise dominates the acoustic emissions,

which is correlated to transient cavitation (Leighton [80]). This strong signal of non-specific frequency can be explained by the violent and random collapses of the single bubbles at high acoustic pressures.

To summarise, it is generally held that signals with clear sub-harmonic frequencies f_0 are more likely to derive from bubble oscillations in the stable regime. If the emissions are dominated by white noise then it may be assumed that the cavitation activity is mostly transient (inertial).

One of the main drivers for the study of acoustic noise was oceanic ambient noise (the sound of the waves), as an issue for shipping navigation. The noise present in the ocean is usually in the frequency range from a few 100's Hz - 10's kHz, and is correlated with the speed of wind (Leighton [80]). Since single bubbles formed in sea waves tend to be smaller than 1 mm in radius, which would correspond to frequencies above 3 kHz (see eq. 2.9), they cannot be entirely responsible for the lower frequency content of the oceanic ambient noise. A physical mechanism that could account for some of this sound generation is the production of bubble clouds, by breaking waves (Yoon *et al.* [141]). It is likely that of the lower frequencies are due to the collective behaviour of bubbles. Such structures could then emit at distinct 'eigen-frequencies'.

Cavitation inception in theory, liquids can resist pressures of the order of from $3 \times 10^4 Pa$ to $3 \times 10^5 Pa$. In practice, tensions on the order of 100 times less are required to induce cavitation, due to imperfections or stress concentrations (Caupin and Herbert [18]). In cavitating liquids, such 'weaknesses' are often termed *nuclei*, as they provide the point of cavitation inception. The exact nature of cavitation nuclei is still under discussion within the scientific community. Pre-existing bubbles present in liquids serve as nuclei, if they are not removed by buoyancy or dissolution. Other impurities, such as particulates, also act as cavitation nuclei as they often contain gas and provide a discontinuity within the medium. Careful filtering and degassing can eliminate most of these sources,

and significantly increase the cavitation threshold. However, experiments with very pure water have not reached the maximum tensile strength calculated theoretically (Herbert and Balibar [56]). Another source of nuclei was identified as electromagnetic radiation, which may be mediated by ionisation, or thermal motion of the molecules. To summarise, a variety of features can be cavitation nuclei: boundaries and surface (particularly structural defects such as cracks, crevasses and debris material), suspended particles, small pre-existing bubbles (nanobubbles) and external electromagnetic radiation, such as cosmic rays.

Cavitation threshold in addition to the nature of the cavitation nuclei, the likelihood for cavitation to occur depends on overall thermodynamic state of the liquid. At increasing temperature the surface tension decreases. At reduced pressure the surface tension loses the capability to maintain a liquid state. For static pressures applied to a fluid, the Blake threshold pressure (as referenced by Leighton [79]) predicts the onset of explosive growth, without actually describing it. This model accounts only for surface tension, and cannot be applied to fully describe the much more interesting non-static pressure cases. It is still very useful in the case of very small bubbles, where the surface tension (*Laplace pressure* $p_\sigma = 2\sigma/R_0$) dominates over inertial and viscous effects. To calculate the critical liquid pressure for explosive growth, it is necessary to exceed a minimum critical radius (R_{crit}), or Blake radius, given by:

$$R_{crit} = \sqrt{\frac{3R^3}{2\sigma}(p_0 + \frac{2\sigma}{R_0} - p_v)} \tag{2.11}$$

where R_0 is equilibrium radius, σ surface tension, p_0 atmospheric pressure, and p_v vapour pressure. This critical radius is derived from the basic equilibrium assumptions of a bubble confined in a liquid medium, which are:

$$p_i = p_g + p_v \tag{2.12}$$

and

$$p_i = p_0 + p_\sigma \tag{2.13}$$

where internal pressure p_i within a bubble, is due to the pressure of the internal gas p_g and internal vapour pressure p_v. For bubbles less than a few micrometers, the pressure inside the bubble is greater than the pressure in the liquid p_0, due to the extra surface tension effect p_σ, which is often referred to as the Laplace pressure.

Finally, it is possible to derive the Blake threshold pressure for explosive growth:

$$P_B \approx p_0 + 0.77\frac{\sigma}{R_0}. \tag{2.14}$$

This equation is valid for small bubbles in the quasi-static case, neglecting viscous effects, and vapour pressure. The threshold discriminating between inertial and stable cavitation is dependent on the ratio of R_{max}/R_0 . The value obtained by Flynn (as referenced by(Leighton [80])), and later by Apfel and Holland (Holland and Apfel [57]) was 2 and 2.3, respectively. Apfel and Holland went on to define *Mechanical Index* (see §2.1.4), to predict the likelihood of cavitation occurrence in response to a given ultrasound protocol. American Institute of Ultrasound in Medicine (AIUM), National Electrical Manufacturers Association (NEMA) and FDA adopted the Mechanical Index (MI) defined as MI=$\sqrt{PNP}/f$, normalized to 1 MPa and 1 MHz. For *in-vivo* cavitation, a critical value of MI = 0.7 was fixed, see also §2.1.4.

Rectified diffusion A gas bubble in a liquid naturally dissolves due to the surface tension pressure, p_σ. When a sound field is present and acts on the bubble, the situation is quite different. A process called *rectified diffusion* describes the active pumping of gas from the liquid into the bubble. It is possible to describe this effect via two contributory elements: *area effect* and *shell effect*. The area effect describes the situation when more gas flows into the bubble during

the rarefaction phase, than out during the compression phase, of an acoustic cycle. This happens because the interface between gas and liquid has a much greater surface area when the bubble is expanded. The shell-effect incorporates the compression of the water surrounding the bubble throughout the oscillation. During the expansion of the bubble, a shell of compressed water is formed. In this compressed volume the pressure gradient pushes gas into the bubble. In the compressional phase, a shell of water under tensile stress surrounds the bubble, and the opposite dynamic happens. However, the compressed shell is thinner than the tensioned shell, and so the inward flow of gas is predominant. A further contribution to this effect is attributed to the behaviour of gas being compressed and tensioned inside the bubble. A net increase in bubble radius may result in the bubble tending toward the resonance size, for which the effects will become even more pronounced.

2.2.3 Bubble and bubble cloud models

Single bubble models Lord Rayleigh had already described mathematically (as seen before with eq. 2.8) the collapse phase of a bubble. In order to study completely the phenomenon of cavitation, the growth phase has also to be described, as well as the collapse. The fundamental work of Noltingk and Nepparis achieved this, by considering the initial growth of the bubble as an isothermal, and the collapse an adiabatic, process. This provides adequate basis to state that a more degassed liquid reduces the number of possible collapses, but also makes each individual collapse more violent (Leighton [80]). In order to fully describe the bubble, the vapour-phase has also to be taken in account. This equation was developed and subsequently modified by Rayleigh, Plesset, Noltingk, Neppiras and Poritsky; therefore it is also sometimes called RPNNP equation (Leighton *et al.* [81]). This is an approximate, non-linear equation, which describes the response of a spherical bubble to a time-varying pressure field $P(t)$, in an incompressible liquid. The radius of rest(equilibrium) is denoted R_0 and the hydrostatic

pressure p_0. The dynamic pressure $P(t)$ superimposed onto p_0, and causes the bubble radius $R(t)$ to change. The following equation can be derived, utilizing an energy equilibrium assumption and also takes viscosity into account :

$$R\ddot{R} + \frac{3\dot{R}^2}{2} = \frac{1}{\rho}[(p_0 + \frac{2\sigma}{R_0} - p_v)(\frac{R_0}{R})^{3\kappa} + p_v - \frac{2\sigma}{R} - \frac{4\eta\dot{R}}{R} - p_0 - P(t)] \quad (2.15)$$

where ρ the medium density, σ the surface tension, p_v the vapour pressure, and η the shear viscosity.

This equation has provided the basis for much of the theoretical work undertaken to describe bubble response to a dynamic pressure field. One simple example is the small amplitude oscillations of a bubble, which is the resonant frequency of a forced linear oscillator, a simplified form is eq. 2.9.

Lord Rayleigh had already noted that the assumption of an incompressible liquid limited his model. Therefore, to realistically describe cavitation effects, such as transient cavitation, compressibility has to be taken in account. To do so, the Herring or Kirkwood-Bethe approximations have to be used. Gilmore (Gilmore [52]), Keller and Miksis, Prosperetti (as referenced by D'Agostino and Brennen [28]) to name just a few, expanded the RPNNP equation to account for more violent cavitation processes.

Bubbles do not usually appear in isolation, but in clouds or clusters as, for example, in acoustic cavitation. Having reviewed the main features of single bubble dynamics, dynamics of bubble-bubble interactions and cloud dynamics now warrants attention.

Bubble cloud dynamics Bubbles produced by acoustic cavitation do not form homogeneously throughout the host medium. Instead they tend to arrange into different types of structures, including clusters of a few bubbles, filaments resembling webs, and clouds of densely packed bubbles, sometimes spherical in the bulk of the liquid. In a standing acoustic wave, as in an acoustic bath, the filaments

form centred at the pressure antinode, for pressure amplitudes that are not too high. The centre of a standing sound field is often a pressure antinode, where bubbles gather forming a dense cloud. It has been demonstrated that such a cloud exhibits global ensemble oscillations at the driving frequency and harmonics of the field, which conform to single-bubbles models, i.e. a Rayleigh-Plesset model (Lauterborn and Kurz [76]), with a quiescent radius selected to match the size of the cloud.

Brotchie *et al.* [13] demonstrated that not only is the average bubble size determined by the frequency of insonation, eq. 2.9, but the size distribution for acoustically driven cavitation. Specifically, in the range from 20 kHz to 1.1 MHz, the bubble distribution becomes narrower with increasing frequency, as predicted theoretically by Yasui [139].

Clouds of bubbles beneath vibrating horns (sonotrodes), often driven at circa 20 kHz, have also been studied for multi-bubble behaviour, including experimentally and theoretically by Hansson *et al.* [54] and Morch [90]. They found that the collapse of bubbles at the centre of the cloud is enhanced by an inwardly propagating shock-wave. Two fluid models were developed by Hansson *et al.* [54] and Omta [99]. Both concluded that the void fraction is the important parameter and Omta specifically looked at bubble clouds of a spherical morphology. The linear (fundamental) resonance frequency of the cloud is found to be well below the linear resonance frequency of the individual bubbles in the cloud. The same conclusion was reached by D'Agostino and Brennen in [27, 29, 72]. Kuttruff (as referenced by Ohl [98]) considers the pressure impulses from collapsing bubbles as the pressure input to the surrounding bubbles, and comes to the conclusion that in polydisperse cavitation bubble fields, the collapse of smaller bubbles enhances the collapse of the larger ones, because the smaller ones collapse first.

Tervo *et al.* [117] observed filament structures experimentally via high-speed photography, and calculated numerically that a simple cluster model based on the Rayleigh-Plesset equation responds with period-doubled, or higher multiples

of the driving period, oscillations. Furthermore, for polydisperse bubble-size distributions, synchronization of period of the oscillation for component bubbles, has been found (Birkin *et al.* [7]). This phenomenon can be of importance as a mechanism for the amplification of collective collapse action of bubble clusters, which has relevance to surface cleaning processes and erosion effects.

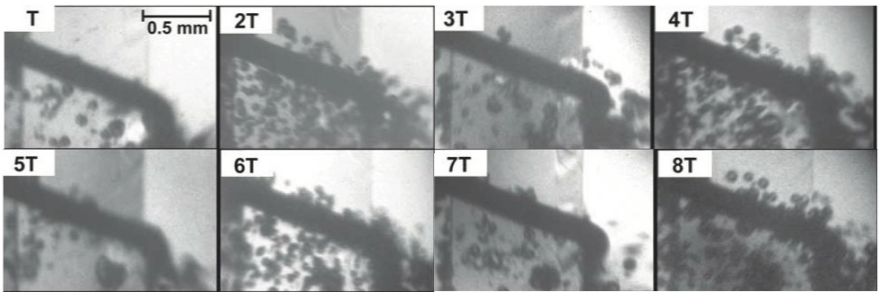

Figure 2.10: High speed images of cluster filaments - Bubble cluster oscillation (one frame per driving period). The cluster dynamics has period-doubled to $2T = 50\ \mu s$. From Tervo *et al.* [117].

2.2.4 Radiation forces acting on bubbles

As seen in §2.1.4, an acoustic pressure wave carries momentum that can be transferred to an object that it is incident upon. The force can be rewritten from eq. 2.5, taking into account the acoustic cycles, as follows:

$$< \vec{F_r} >= - < V \vec{\nabla} P_A > \tag{2.16}$$

where '<>' denotes the time-average and V the bubble-volume (Leighton [80]). In 1936, King published theoretical calculations regarding the acoustic radiation force acting on solid spheres (as referenced by Doinikov [35]). As a spherical object, a bubble obeys the same laws with the important condition that its resonance frequency (eq. 2.9 in §2.2.2) must be very different from the frequency of the incident acoustic wave. If the bubble radius is close to resonance with the field, the compressibility of the gas plays an important role, first investigated by Hasegawa and Yosioka [55]. They showed that the secondary acoustic field

radiated from an oscillating bubble (close to resonant size) will couple with the primary field and that the radiation force acting on the bubble is much higher than that expected for a solid sphere (theoretically a factor of 8×10^9 higher, fig. 2.11). This is a key fact to the results presented in §4.3 of this this thesis.

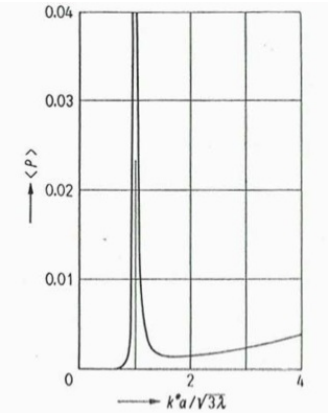

Figure 2.11: Radiation pressure dependency on frequency - Radiation pressure on an air bubble at 0 °at 1 atm, normalized to peak value. (from Hasegawa and Yosioka [55])

Bjerknes forces can be considered as an extension of the acoustic radiation forces acting on bubbles, that are coupled to a primary acoustic field. There are two types of Bjerkens forces, generally referred to as *primary* and *secondary*. The primary Bjerknes force was originally defined as in a standing-wave configuration, and explains bubble migration patterns in such a field. This force was first observed by Bjerknes in 1906 and properly identified by Blake in 1949 (as referenced by: Leighton *et al.* [81] and Brennen [12]). In a standing wave field, the pressure gradients oscillate, as well as the bubbles. Bubbles of radius less than the resonance size oscillate in phase, and larger bubbles at 180 ° out of phase, with the sound field. Therefore $\vec{F}$ will be in one direction for bubbles below the resonant size, and in the opposite direction for bubbles above. Averaged over time, smaller bubbles will therefore move 'up' a pressure gradient, to the pressure antinodes. This was demonstrated experimentally by Crum and Eller, in 1970 (as referenced by Mettin [88]). Bubbles larger than the resonant size will conversely move to the pressure nodes. It should be noted that the primary Bjerknes force acts in

any field with a gradient, and therefore will also apply to the case of propagating acoustic fields.

The secondary Bjerknes force describes the bubble-bubble interaction forces for multiple bubbles in a primary acoustic field. A bubble oscillating in response to a primary field may be considered as the source of a secondary acoustic field. In the presence of an oscillating second bubble (or indeed a surface), the coupling of the oscillations to the gradient of the secondary field induces a mutual interaction. Generally, bubbles will attract each other under the influence of the secondary Bjerknes force. There is a special case, whereby if the driving frequency lies between the resonance frequencies f_r of two bubbles of different R_0's, the secondary Bjerknes force acts as a mutual repulsion. Theoretical studies (Mettin *et al.* [88]) indicate that in very high pressure (primary) fields, the secondary Bjerknes force can be dominant. This is therefore an important consideration for the case of cavitation clouds in HIFU.

2.2.5 Cavitation bioeffects and sonoporation

As mentioned previously (see §2.1.4), the bioeffects incurred during the application of HIFU to tissue for FUS can be divided in thermal and mechanical. The occurrence of cavitation is evidently primarily mechanical, however, bubble activity during FUS can also have a pronounced effect on the efficiency of thermal deposition. Here, it is helpful to consider inertial versus stable cavitation, as defined in §2.2.2.

Enhanced heating currently, clinical FUS relies on viscous absorption to mediate heating at the target region. This is inherently an inefficient process, which translates to lengthy procedure times, particularly for the treatment of bulky conditions such as uterine fibroids (see §2.1.6). It has been demonstrated that inertial cavitation has the potential to mediate *enhanced heating* (Holt and Roy [59]), whereby the required thermal dose may be deposited more rapidly and

therefore over a much reduced HIFU exposure. There are several distinct mechanisms whereby cavitation-related effects act to focus incident HIFU energy, thus facilitating enhanced heating (Coussios *et al.* [24]): (i) The gas-tissue interface of a cavity in FUS, will itself mediate strong frictional effects, as the bubble oscillates under HIFU exposure. This provides enhanced heating in the tissue environment local to the cavity position. (ii) A cavitation cloud, consisting of multiple bubbles in close proximity to each other, will act to scatter and re-scatter incident HIFU between the component bubbles. This 'trapping' effect serves to increase the propagation path-length effectively travelled by the HIFU, through the tissue hosting the cloud, which in turn results in a greater proportion of the incident energy being absorbed. (iii) as discussed §2.2.2, inertial cavitation is associated with broadband white noise acoustic emissions. As such a strongly collapsing bubble 'receives' HIFU excitation at a given frequency and remits across a much larger bandwidth, some of which will be at higher frequency values than that incident to it. As the absorption coefficient of tissue increases with the frequency of the acoustic wave propagating through it (see eq. 2.1), a higher proportion of the re-emissions will be absorbed. This can be used to heat the tissue more efficiently, and reduce expensive treatments times, especially in MRgFUS.

In the extremity of pressure amplitude, the enhanced heating can reach near-boiling temperatures for exposures of approximately 1 s (Coussios and Roy [25]). So called *histotripsy*, is being investigated as a treatment for BPH in canine models, for example (Lake *et al.* [73]).

Tissue permeabilisation The mechanical action of cavitation, in combination with HIFU, is well known for producing tissue and cell membrane permeabilisation. Stabilised ultrasound contrast agent (UCA) microbubbles are widely used to provide cavitation nuclei, for an effect often termed *Sonoporation* ('sono'-sound, 'poration'-permeabilisation). Much of the early work on sonoporation was conducted with tissue culture constructs, including cell suspensions and monolayers

(supported on a pre-treated substrate), *in-vitro* (Guzman *et al.* [53], Ward *et al.* [127]). Two sonoporation regimes were identified, with no clear distinguishing threshold. For more aggressive exposure conditions (including higher HIFU intensities and higher microbubble concentrations), outright cell death by lysis tends to be the predominant effect, which is sometimes termed *lethal sonoporation*. Alternatively, if the exposure parameters are moderate, some cells retain downstream viability, but exhibit uptake of extraneous molecules, generally in the form of otherwise membrane-impermeable fluorescent species. These observations indicate that the cell membrane has been permeabilised during the exposure, but the damage inflicted has not been so severe as to result in cell death, either by lysis or apoptosis. In this case *reparable sonoporation* is said to have occurred. Sonoporation has been successfully reported as a protein and RNA delivery mechanism (Reslan *et al.* [108]).

A substantial body of literature now exists, reporting empirical results on sonoporation over a wide range of ultrasound exposure conditions, in varying experimental configurations, delivering an array of substances to cells. Reports on the mechanisms by which membrane pemeabilisation is affected, by microbubbles exposed to ultrasound remains, are much more elusive. At very low intensities Marmottant and Hilgenfeldt [84] have shown that shear flow from microstreaming around a stably cavitating bubble, plays an important role in vesicle-membrane rupture. At the higher intensities typical HIFU, Prentice *et al.* [105], reported microbubble jets (see §4.2.4) as capable of membrane penetration, and subsequently correlated damage features via *atomic force microscopy*. It appears likely that for a given exposure protocol, a potentially high number of contributory mechanisms will be in action.

For *in-vivo* applications, the blood brain barrier (BBB) can be rendered permeable by the HIFU-microbubble combination (Vykhodtseva *et al.* [124]), see §2.1.6. The BBB is formed by the brain capillary and endothelium, which regulates the transport of material into the brain tissue. This makes drug-delivery

to the brain extremely challenging. Several studies have shown that ultrasound-induced effects can result in localized BBB disruption (Tung *et al.* [121]). It was shown that if microbubbles are already present in the sonicated area, less acoustic energy had to be use to obtain similar results.

3

Materials and Methods: Hybrid laser-HIFU cavitation apparatus

3.1 Overview of chapter

Acoustic cavitation is a notoriously difficult phenomenon to study, particularly the early stages of development following activity inception. In the case of HIFU for medical applications, this is compounded by the microscopic size of resonant bubbles, eq. 2.9 (see §2.2.2), and the ultra-fast dynamics that will result in response to typical MHz frequencies. Moreover, the exact site of nucleation is difficult to predict, often occurring at an impurity or gaseous inclusion within the field, and not necessarily inside the focal volume.

In contrast, laser-induced cavitation, whereby a short laser pulse is focused into a liquid to form a plasma, which rapidly expands to generate a cavity, is a well-established and understood approach used to study single-cavity dynamics in a range of fluidic environments (Chen *et al.* [22], Evans *et al.* [40], Fujimoto *et al.* [47], Kim *et al.* [64], Palanker and Turovets [101]). The distinct advantage of this technique is that the location and instant of cavity formation is pre-determined,

defined by the point to which the laser pulse is focused. This allows the incorporation of high-speed cameras, capable of imaging at frame rates necessary to resolve the ensuing dynamics. In this manner, cavitation-related activity such as the phenomenon of jet-formation (see §4.4) during collapse in the vicinity of a boundary, (thought to contribute to material erosion and surface cleaning effects, (Brujan *et al.* [14], Niemczewki [93], Tong *et al.* [120])), can be investigated systematically and reproducibly.

The uncertainty of the spatial and temporal occurrence of acoustic cavitation prevents meaningful implementation of high-speed cameras, for studying the development of cavitation activity in ultrasound fields, although a number of such studies have been attempted (Birkin *et al.* [7], Tervo *et al.* [117], Wang *et al.* [126], Zhou *et al.* [142]). A common feature in these reports is the large field-of-view and long exposure times that the investigators are required to employ, to capture images of acoustic cavitation activity without prior knowledge of the moment and location of nucleation. This limitation significantly reduces the impact of the observations on the understanding of acoustic cavitation cloud evolution, particularly over the first few hundred cycles of ultrasound exposure. Laser-induced cavitation studies allow much higher temporally and spatially resolved dynamics, but have limited relevance to acoustic cavitation as the pulse energy required to induce optical breakdown in the host medium, results in a single cavity of dimensions typically around a few 100 μm, at maximum expansion. This is much larger than those typically encountered in MHz ultrasound fields (see §2.2.2) during the early phases of development following inception.

In this thesis, the development of an instrument that combines conventional approaches to study acoustic and optical cavitation, which facilitates the use of high-speed cameras at MHz frame rates, to observe the evolution of HIFU driven cavitation clouds, is reported. Laser-induced cavitation in an ultrasound field has been previously investigated, with the aim of enhancing collapse phenomenon,

using high-speed photography. To this end, bubble sonoluminescence was studied as a function of seeding phase, in a 130 kHz field (Palanchon *et al.* [100]). The current work is quite distinct in terms of employing low-energy nanosecond pulses in a well-characterized, moderate to high-MI HIFU field.

In this chapter the experimental arrangement is described in detail. Methodologically, the primary innovation is the custom-designed *sonoptic chamber* that allows optical access to the focal region of a HIFU transducer, whilst also allowing the field itself to propagate unimpeded. Moreover, the formation of standing waves, which are known to significantly affect cavitation activity (Koller and Shankar [67], Leighton [79], Parlitz *et al.* [103]), is avoided. As such, the configuration is taken to be representative of an idealised FUS procedure, in terms of a propagating HIFU field. The host medium, however, for all results presented is degassed water with an oxygen content of < 4 mg/L, which of course has different mechanical properties to tissue. Degassing was achieved using liquid heating (Shaw and ter Haar [112]), with gas content measured before and after the experiments using a DO 110 dissolved oxygen meter (Oakton, USA). The influence of known tissue parameters on key observations of cloud dynamics is addressed in §4.2.3.

Fig. 3.12 is provided to depict the various cavitation regimes that can be studied with the sonoptic chamber, defined in terms of laser-pulse energy and HIFU peak negative pressure, PNP, at the focus. These include (see §3.8) conventional laser-induced cavitation, the interaction between a laser-induced cavity and a HIFU field and the new technique of *laser-nucleated acoustic cavitation* (LNAC) (Gerold *et al.* [50]).

3.2 The sonoptic chamber

To observe cavitation phenomena at high spatial and temporal resolution, a specific experimental set-up was built, shown in fig. 3.1. A custom-designed sonoptic chamber, was constructed according to the dimensions of the field from a HIFU transducer, to accommodate the ultrasound beam produced, without scatter or reflection. The unique tapered shape also allows optical access to the medium located at the HIFU focus.

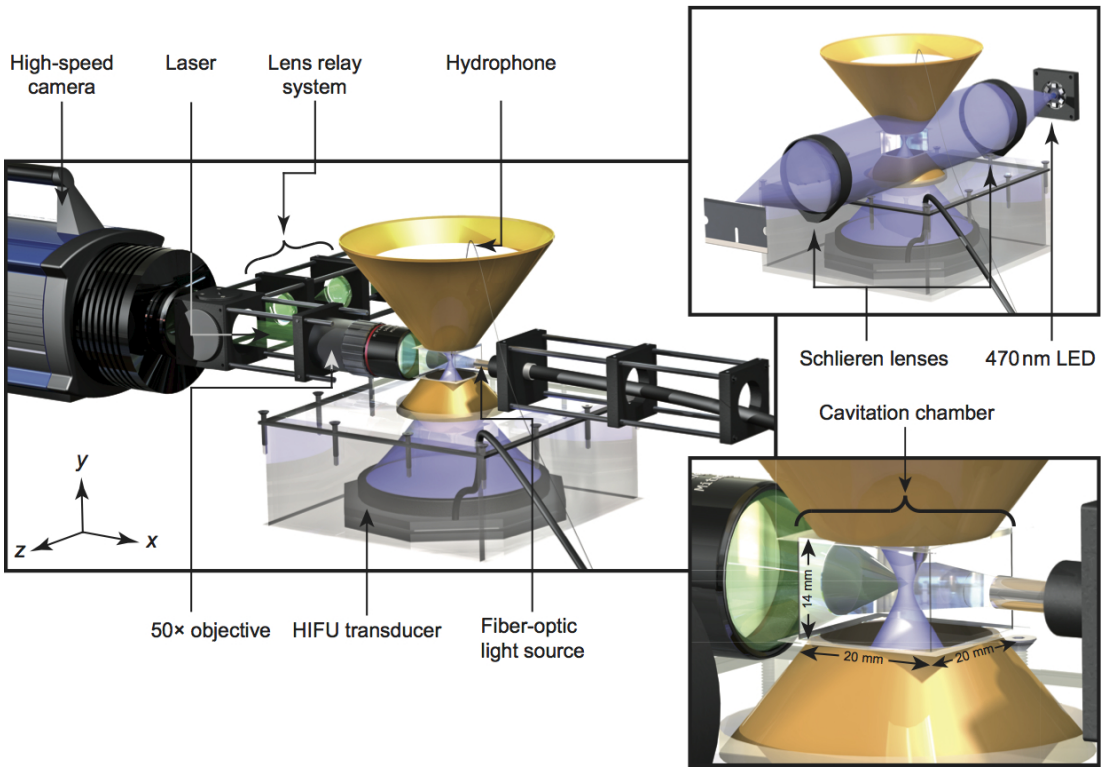

Figure 3.1: 3D model of the experimental set-up - Representation of the custom-made sonoptic chamber, constructed according to the dimensions of the HIFU field. The Shimadzu HPV-1 high-speed camera is depicted. Inset top right is the Schlieren imaging arrangement for alignment of the ultrasonic and optical foci. Inset bottom right is a close up of the cavitation chamber which contains the ultrasound (blue) and laser (green) foci.

The sonoptic chamber was constructed from 6 mm thick polycarbonate sheets of internal dimensions, $188 \times 188 \times 89\ mm^3$, with two polyvinyl chloride funnels connected via the tapered ends to a $20 \times 20 \times 14\ mm^3$ *glass cavitation chamber*, constructed from standard 1 mm thick microscope slides (Scientific Laboratory

Supplies Ltd., UK). The position of the cavitation chamber over the transducer is such that the centre aligned with the HIFU focus, see figs.3.2 and 3.6.

The second inverted funnel was positioned above the cavitation chamber, fig. 3.2 (a), to allow unhindered acoustic propagation into the far field. Acoustic absorber was positioned inside the funnel, on a plane tilted to the propagation axis, to minimize reflections of the ultrasound from the water surface. The sonoptic chamber was mounted on an M-652 x-y-z micro-translation stage (Newport, UK) for alignment of the HIFU focus to the optical focus, undertaken using a schlieren set-up, described in §3.4 below. Each component of the experimental configuration is addressed individually below, namely; the HIFU source, the pulsed-laser, the high speed cameras and the passive cavitation detector (PCD).

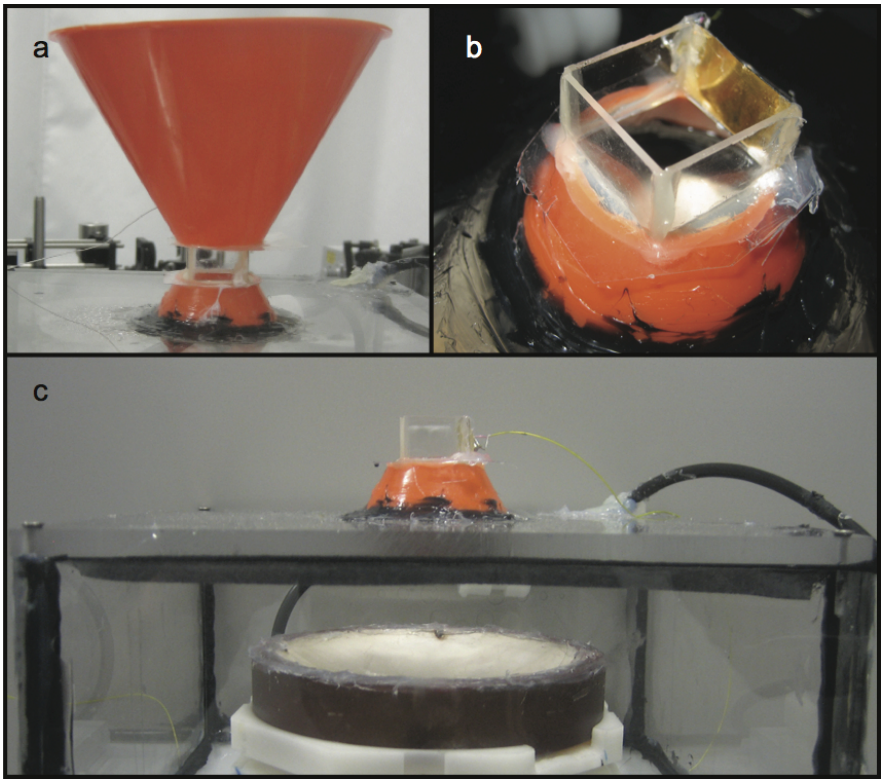

Figure 3.2: Photographs of the sonoptic and cavitation chamber - (a): an inverted funnel allows the HIFU far-field to propagate beyond the focus. Absorbing material placed over the top surface minimizes interference between incident and reflected waves. (b): glass cavitation chamber, located at the HIFU focus; in this early configuration one wall was made out of PVDF for acoustic detection. (c): the HIFU transducer, in position on the base of the sonoptic chamber

3.3 The HIFU source

3.3.1 The transducer

The HIFU source is a single-element, 100 mm diameter, spherically focused piezo-electric transducer (PZT), with a geometric focus of 80 mm (GE Healthcare, USA). This transducer was one of the prototypes built by Selfridge for GE Medical Systems to implement, at the time newly conceived, technique of MRgFUS. This led then to the creation of the spin-off company InSightec Ltd. Originally, the transducer was designed and matched electrically to the third harmonic at 1.471 MHz, with a 40% (PNP up to 8.9 MPa) conversion efficiency from electrical power (W_e) to acoustic power (W_{ac}). A second matching circuit was made *in-house* to stimulate the fundamental resonance frequency (0.521 MHz) at a reduced efficiency of around 20% (PNP up to 1.8 MPa). A transducer can be electrically matched to a value between between electrical and mechanical resonance of the piezo-ceramic. As such the 3^{rd} harmonic frequency-of-operation is not an exact multiple of the fundamental. The device was driven by an AFG3102 (Tektronix, USA) arbitrary function generator, with the signal passed via a 20 dB attenuator to a 3200LA, 55 dB RF amplifier (250kHz-150MHz, Electronics & Innovation, USA).

The frequency-of-operation for the results presented was selected according to the demands of the cavitation phenomena being studied, relative to the frame rate available with a given high-speed camera.

3.3.2 Field scans and simulations

The ultrasound fields at both frequencies were characterized in a three-dimensional ($1 \times 1 \times 1\ m^3$) scanning tank, using a *fibre-optic hydrophone* (Precision Acoustics, UK), with a tapered tip of sensitivity 111 mV per MPa, at 1 MHz. Free-field profiles were generated, and subsequently used to validate the fields for the transducer located within the sonoptic chamber.

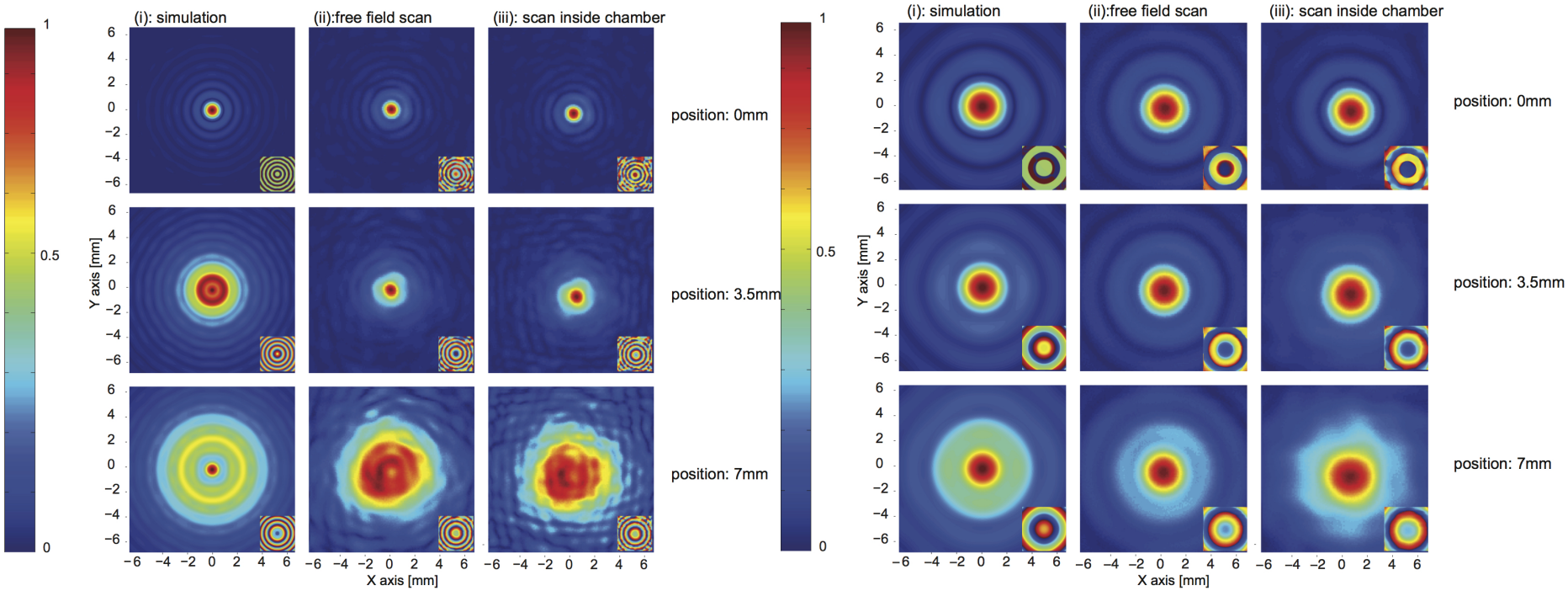

(a) 1.471 MHz

(b) 0.521 MHz

Figure 3.3: HIFU field scans and simulations - Main figures show acoustic pressure amplitude field maps at both driving frequencies. The insets depict complementary phase maps. The normalized colour map is relative to each scan and not absolute for all the sub-figures. The z-axis is arbitrarily defined as positive along the acoustic propagation, away from transducer, with 0 mm at the geometrical focus. Comparison of columns (ii) free field scan and (iii) field-scan within the cavitation chamber, confirm the HIFU field is unaffected by the sonoptic chamber.

The pressure field was scanned at several locations along the ultrasound propagation axis: -7, -3.5, 0, 3.5, and 7 mm, fig. 3.3, in both configurations to ensure that the HIFU field is unaffected by the sonoptic chamber. Furthermore, MatLab simulations of the pressure fields, based on a Fourier acoustics approach (see Appendix 6.3) , demonstrate good agreement with the experimentally determined profiles, columns (i) of fig. 3.3. Each row shows a different z-position, i.e. at 0 mm, at 3.5 mm in and at 7 mm, where 0 mm is the geometrical focus of the transducer. Positive values refer to the same direction as the ultrasound propagation (away from transducer). Column (ii) depicts the free-field scans, which can be compared to scans obtained inside the cavitation chamber, column (iii).

It can be noted that for the driving frequency, $f_0 = 0.521$ MHz the focus to the -6 dB line is at 2.84 mm, and for $f_0 = 1.471$ MHz, at 1.01 mm, see fig. 3.4. Compared to the glass cavitation chamber dimensions of $20 \times 20 \times 14\ mm^3$ indicated that the distortions to the field would be negligible. A final scan was performed in the plane along the ultrasound propagation axis, again with the transducer positioned within the sonoptic chamber, to reveal the pressure gradients existing in the locale, fig. 3.5.

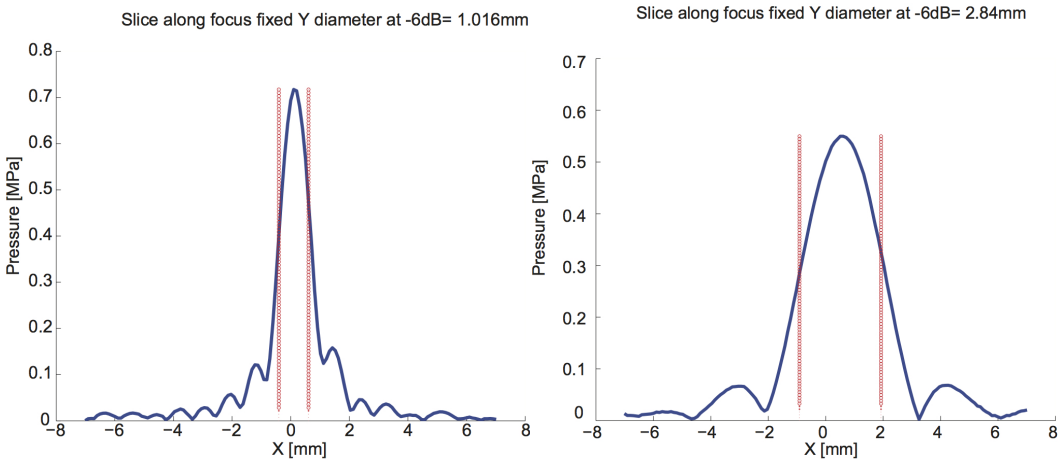

(a) 1.471 MHz **(b)** 0.521 MHz

Figure 3.4: Beam profiles - 0.521 MHz driving frequency the focus is 2.84 mm; 1.471 MHz the driving frequency the focus is 1 mm, at the -6dB line.

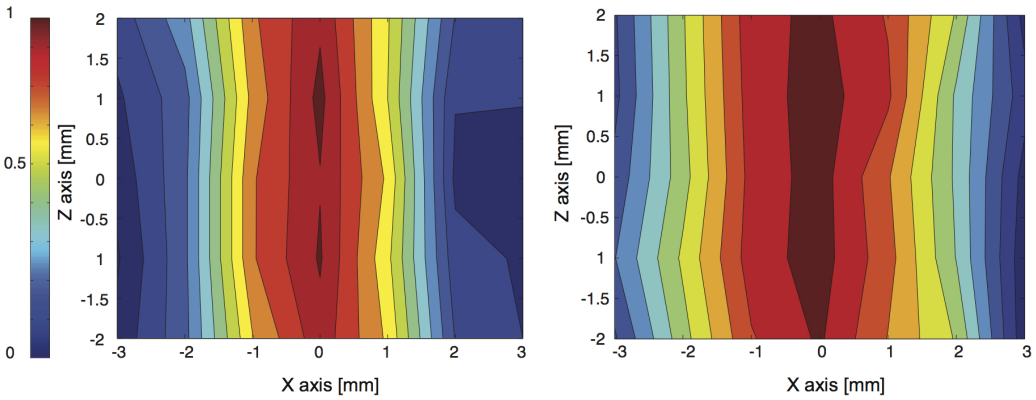

(a) 1.471 MHz **(b)** 0.521 MHZ

Figure 3.5: Manual vertical field scans - These scans were obtained positioning the hydrophone tip inside the glass cavitation chamber, in a similar fashion as represented in fig. 3.6. The tip was scanned across the focus using a micro-translation stage.

3.4 Schlieren arrangement

Alignment between the acoustic and optical foci is critical to obtaining reproducible results. To achieve (coarse) alignment, a monochromatic Schlieren imaging set-up was assembled around the optical windows of the cavitation chamber, orthogonal to the laser propagation axis, see fig. 3.1 (see inset, top right). Schlieren imaging allows the visualization of density, or pressure, variations within transparent media (Neumann and Ermert [92]). A 470 nm light-emitting diode (Lumileds Lighting, LLC, San Jose, CA) was used as a continuous light source in combination with two lenses of diameter 50.8 mm, f150 mm lenses (Comar Instruments, UK) to generate a collimated beam across the optical window. The large lenses were used to fully cover the cavitation chamber. A razor blade, mounted on a vertical translation stage provided the zero-order stop, and the image was projected onto a white screen. A Schlieren shadowgraph showing the laser spot and the acoustic focus during the alignment procedure is shown in fig. 3.6 (top right). The shadow of the needle-hydrophone used to record acoustical data during preliminary experiments, is also apparent in this image.

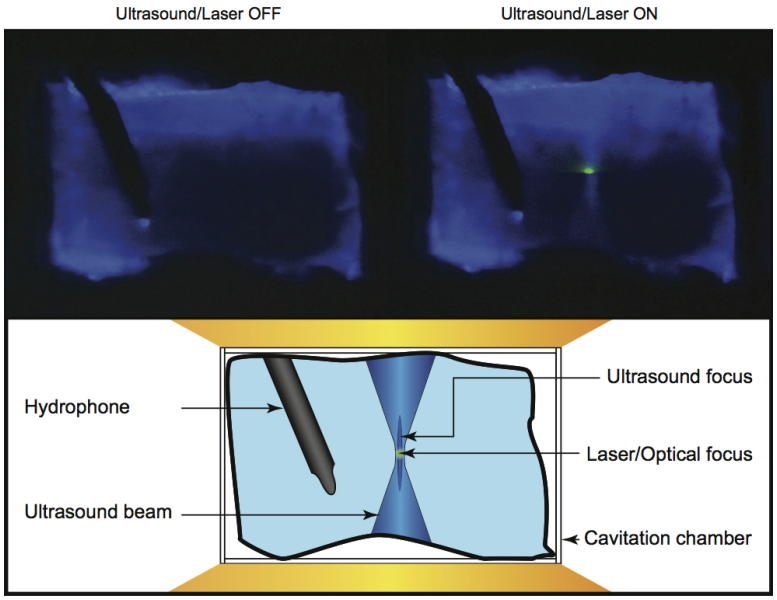

Figure 3.6: Schlieren arrangement - Schlieren image of cavitation chamber, used to align the laser focus (green spot) to that of the HIFU-focus (lighter blue region). The needle hydrophone used to record preliminary acoustical emissions during cavitation activity is also visible.

3.5 The pulsed-laser and optics

The laser source was a Litron TRL 420-10 Q-switched frequency-doubled Nd:YAG pulsed laser (Litron Lasers, UK) emitting up to 210 mJ at 532 nm, with a pulse duration of 6-8 ns and a repetition rate of up to 10 Hz. For an experiment, the laser is switched to single-pulse mode and triggered from the high speed camera, with an appropriate delay accounting for the Q-switch. The repetitive pulse mode, at 10 Hz, is used only for alignment at the beginning of an experiment, fig. 3.6.

To accurately control the pulse energy, two sets 650-1050 nm, 10 mm diameter antireflection coated, polarizing cubes (GL10-B Thorlabs, Ltd., UK) and 532 nm, diameter 12.7 mm $\lambda/2$-wave plates (Thorlabs, Germany) were used. The first cube and wave plate pair provided coarse attenuation, the second used for fine energy adjustments. The beam was expanded to slightly overfill the back aperture of the laser-focusing objective lens (50× 0.42 NA (numerical aperture), M Plan, NIR, infinity corrected lens (Mitutoyo, Japan), ensuring the laser is as tightly focused as possible. This was achieved with a ×2 expansion telescope

constructed from f150 mm and f300 mm antireflection coated lenses. The pulse was redirected with a 532 nm, diameter 25.4 mm dichroic mirror (Thorlabs) into the back aperture of the objective. To control beam collimation prior to entering the objective lens, the pulse was passed through a 4f lens relay system comprised of two f150 mm conjugate lenses.

The laser energy was measured at the back aperture of the focusing objective lens, using a S370C power meter (Thorlabs, Germany). The sensitive optics of the high-speed camera(s) were protected from scattered laser radiation using a dichroic band-pass filter 540 IB 50, 98% at 532 nm (Comar Instruments, UK).

Figure 3.7: Photograph of the entire experimental set-up - In this configuration two high speed cameras are positioned orthogonally around the sonoptic chamber; the Cordin 560-62 to the left of the image, the Shimadzu HPV-1 just visible beyond the inverted funnel. To the right of the picture (from bottom to up) is the power amplifier, flash capacitor bank, signal delay generator, arbitrary signal generator, oscilloscope (for passive cavitation detection recordings) and laser power-meter. The sonoptic chamber is in the centre of the picture, with Shimadzu control computer on the shelf above. Compressed gas canisters (N_2 and He, for Cordin operation) are visible beyond the camera, to the left. On the table: the laser head, optics, laser shutter and laser control boxes.

3.6 The high-speed cameras

High-speed cameras may be incorporated into the experiment via one of the two possible configurations. As depicted in fig. 3.8, imaging can be achieved through the same objective lens (*parallel configuration*) that focuses the laser into the ultrasound field (continuous line). The option of imaging through a second objective lens orthogonal (*orthogonal configuration*) to the laser propagation direction (dashed line, fig. 3.8), offers the distinct advantage of decoupling the observation from the laser focusing for independent micro-translation, once the Schlieren optics have been removed following the alignment procedure. Two infinity corrected objective lenses (5× 0.14 NA M Plan APO, 10× 0.28 NA M Plan APO, Mitutoyo, Japan), were used in an orthogonal configuration (to the laser propagation axis) to provide an alternative viewing perspective and a different field of view. The fibre-optic bundle delivering the flash illumination to the cavitation chamber, must also be rotated through 90°, from the position represented in figs. 3.1 and 3.8.

The choice of high-speed camera is largely determined by the frame rate required to observe a particular cavitation-related phenomenon. The results presented in this thesis are obtained with one of three high-speed cameras: the Shimadzu HPV-1 (Shimadzu, Japan), the Cordin Model 550-62 device (Cordin, USA), and the SIM-16 (Specialised-imaging, UK). The former consists of a single CCD sensor capable of recording 100 frames of 312 × 260 pixels, at frame rates of up to 1×10^6 frames per second (Mfps), with a minimum individual frame exposure time of 250 ns. The second is a compressed gas-driven rotating mirror camera, capable of recording 62 frames of 1000 × 1000 pixels at frame rates up to 4 Mfps, when using compressed helium gas to rotate the turbine. The Model 550-62 has a minimum exposure time of 200 ns. The third is a 16 channel camera equipped with high sensitivity (intensified) CCDs capable, in principle, of framing rates up to 200 Mfps. Each sensor has a resolution of 1360 × 1024 pixels, with light directed to each by way of a 16-faceted prism.

Spatial scales for the high speed images presented were determined by imaging flow cytometry beads, of diameters 10 and 50 μm, *in-situ*.

For high-speed camera data acquisition rates that did not necessitate flash illumination, an LB60 continuous fibre-optic light source (Welch Allyn, USA) coupled to a 4 mm fibre-optic cable; capable of providing 7.96×10^6 lux at the receive end of the fibre-optic cable, was used. For higher acquisition rates, a Model 659 (Cordin, USA) Xenon flash system was used, coupled to the fibre-optic bundle via a condenser lens (Comar Instruments, UK). The flash-head provided 3.23×10^6 lux at 3 m, with an adjustable duration of up to 1 ms. The exit end of the fibre-optic cable was positioned $\sim$ 2 mm from the glass surface of the cavitation chamber. To ensure synchronization of the laser-pulse, flash illumination and high-speed camera operation, each component was electronically triggered with appropriately delayed TTL pulses, fig. 3.8.

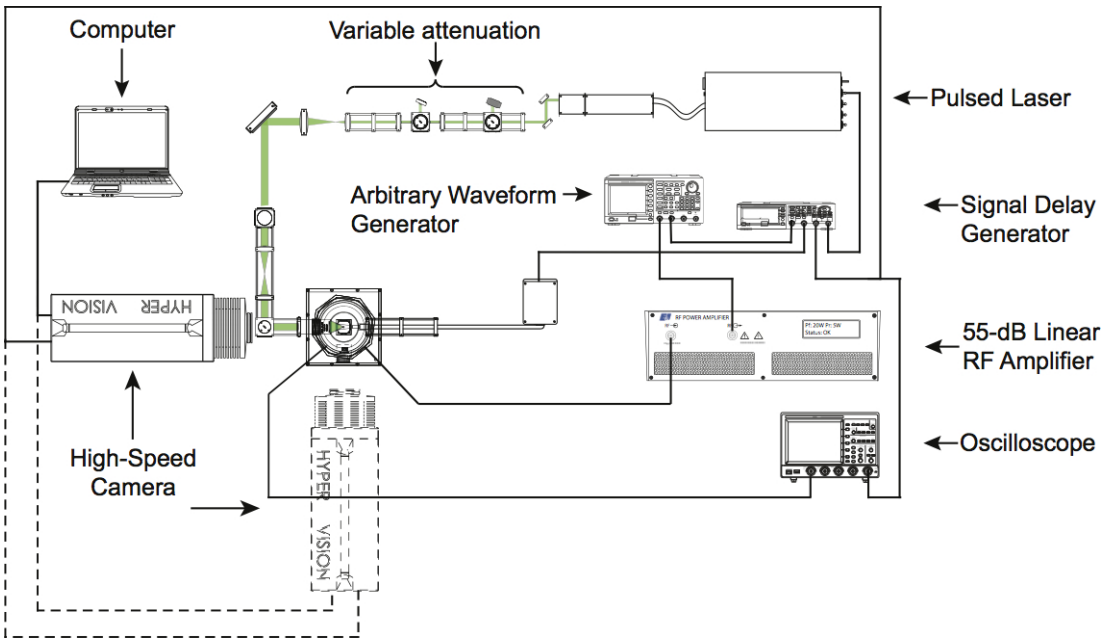

Figure 3.8: Schematic experimental set-up - Schematic overview of apparatus, including BNC trigger lines and ultrasound driving electronics. Continuous lines refer to parallel configuration, where observation and laser path into the chamber coincide. The orthogonal configuration is depicted with a dashed line, for which different observation and laser-focusing objective lens are used.

For most of the results presented below, $t = 0\ \mu s$ is defined as the frame at which the laser-pulse is incident to the cavitation chamber. The waveform generator, in manual trigger mode, was used to initiate an experiment, providing sinusoidal for the HIFU at $t = -70\ \mu s$; $15\mu s$ to allow for transducer 'ring-up' to the required pressure amplitude, and 55 μs for the ultrasound to reach the focus. The waveform generator also provided an initial TTL pulse sent to an Agilent 33250A signal delay generator (Agilent Technologies Ltd., UK). This sent coordinated trigger pulses to the laser at $t = -180\ \mu s$, to account for the Q-switch delay, the flash capacitor bank, to allow the intensity to rise for maximum illumination, and to the high-speed camera, which was set internally, to $t = -10\ \mu s$ to capture a number of frames before cavitation activity was initiated.

3.7 Passive cavitation detection

For preliminary experiments that required acoustic detection (Gerold *et al.* [50]), a custom-made 200 μm PZT needle-hydrophone connected via an amplifier (42× at 1 MHz) to an MSO7104A oscilloscope (Agilent Technologies Ltd., UK) was situated within the cavitation chamber, slightly outside the HIFU focus (see fig. 3.6). During these early experiments, it became apparent that the sensitivity of this type of hydrophone was not sufficient for detailed studies over the frequency bandwidth of interest. To improve acoustic sensitivity, a custom-fabricated *passive cavitation detector* (PCD) was constructed, as described here. The PCD device was used to record the signature acoustic emissions during the cloud oscillation results of §4.2.

For this work, preliminary high-speed observations determined the frequencies of interest (of bubble-ensemble oscillations) to be between 200-400 kHz, for a HIFU driving frequency of $f_0 = 0.521$ MHz. It was also desirable to detect the fundamental frequency and where possible, higher harmonic components. Accordingly, the PCD device was constructed as follows: the active element is

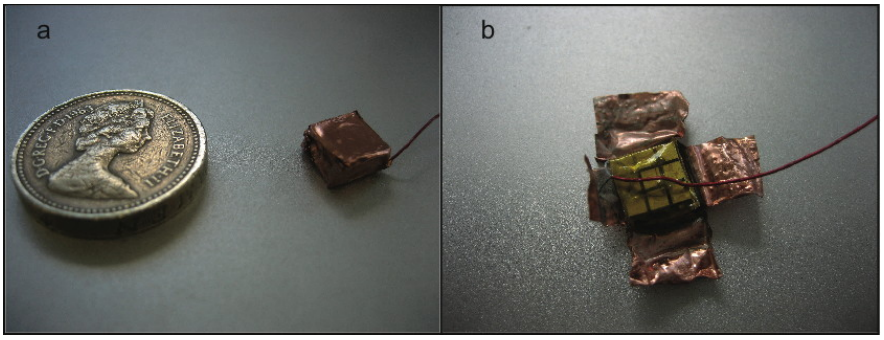

Figure 3.9: Passive cavitation detector - (a) The PCD used to detect acoustic emissions from cavitation clouds in focused ultrasound. (b) With the copper tape peeled back to reveal the kerfed piezo-ceramic composite.

comprised of piezo-ceramic composite, measuring $9 \times 9 \times 3$ mm, cut with kerfs to reduce losses in the material. Copper tape provides ground for the ceramic and also shields the device, particularly from the Q-switch of the pulsed-laser. A second electrode is soldered to micro-coaxial cable and isolated from the shielding. Fig. 3.9 is a photograph of the device. The hydrophone was initially assessed with an electrical impedance analyser, to determine the electrical characteristics. The sensitivity was characterised by positioning the hydrophone in a water tank at ~ 1 m from the focus of a HIFU field, in degassed water. A transducer (ExAblate® 2000, InSightec Ltd, Israel) was driven at a very high power to generate cavitation, which could be observed visually and also produced a characteristic 'fizzing' noise in the audible range. A 1 ms signal was recorded three times for analysis in MatLab. The recordings in the frequency domain were averaged and the driving frequency of 1.17 MHz, filtered out. Finally, a sensitivity characteristic was obtained, depicted in fig. 3.11, following the boundary of the acoustic spectra.

During an experiment, the hydrophone was placed in the glass cavitation chamber of the sonoptic chamber, fig. 3.10, connected to an oscilloscope (MS07104A, Agilent, UK). Data was recorded at a minimum of 1 GS/s, saved in .bin format on a USB stick and transferred to a PC for analysis. This analysis primarily consisted of transforming the time-domain signal via *Fast Fourier Transform* (FFT) into the frequency-domain. This was performed on a computer with a MatLab code (see Appendix 6.3).

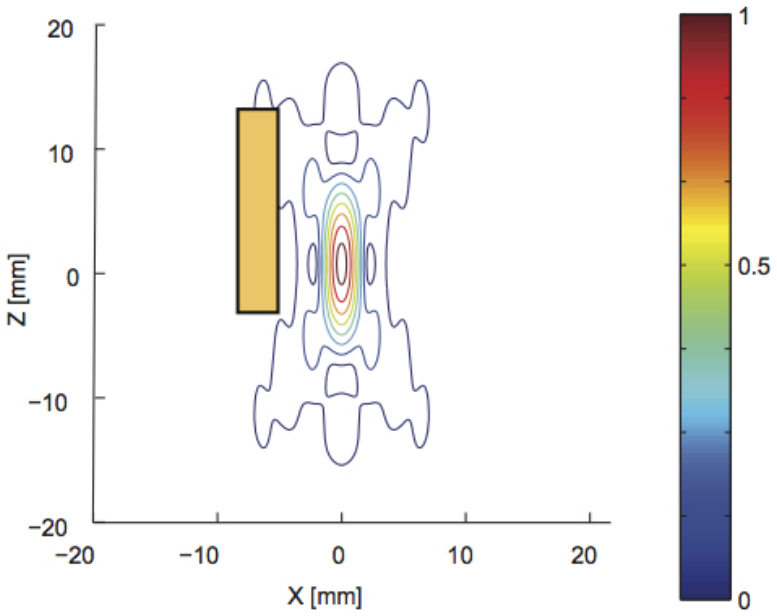

Figure 3.10: Position of the PCD relative to HIFU focus - Schematic representation of the PCD relative to the ultrasound focus at (f_0=0.521MHz depicted). Colour bar on the right of normalized acoustic intensity

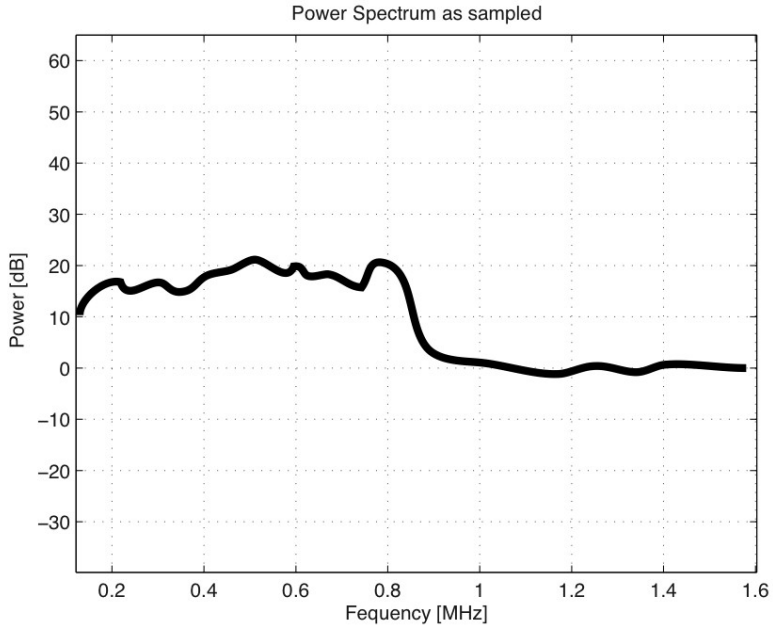

Figure 3.11: The sensitivity characteristic for the PCD - Broadband acoustic noise signals were recorded for 1 ms and analysed in MatLab. The recordings in the frequency domain were averaged and the driving frequency of 1.17 MHz, filtered out.

3.8 Sample results

The experimental set-up described can be used to study three main types of cavitation dynamic: (i) the 'classic' laser-induced cavity (LIC), (ii) the interaction between a LIC bubble and a HIFU exposure, and (iii) a previously unreported mechanism for 'seeding' acoustic cavitation, referred to here as *laser-nucleated acoustic cavitation* (LNAC) (Gerold *et al.* [50]). The laser-pulse energy, relative to the optical breakdown threshold of the host medium (degassed and filtered water), is the parameter that determines which of these regimes occur. The threshold energy value itself is a function of the host medium and also the numerical aperture of the objective lens used. For pulse energies equal to, or slightly above the threshold value, an elliptical plasma forms at the optical focus. The plasma has a much stronger interaction with the laser-radiation than the surrounding water, in the ambient liquid phase. The intense heating that results causes rapid expansion, and thus a classic vapour-filled LIC forms. The strong interaction also acts to scatter some of the incident laser-radiation, which is apparent as a characteristic bright flash during the first few frames of such a sequence (see figs. 3.12 (b)(i) and (c)(i)), despite the optical filter used to protect the camera optics from laser exposure. Laser pulse-energies much higher than the breakdown threshold form elongated plasma regions, from which multiple and overlapping LICs form (see fig. 3.12 (a)(i)). Although interesting dynamics can be occasionally be observed at such high laser energies (Vogel *et al.* [123]), they are uncontrollable and not reproducible, and thus are not discussed further here.

In the absence of HIFU radiation, a laser pulse of energy below the breakdown threshold will have no discernible effect, as no plasma forms to absorb the laser-radiation. If, however, such a low energy pulse is coincident with a pre-established HIFU field (or a HIFU field is generated shortly afterwards), then cavitation activity that is markedly different to the laser-induced cavity results (see figs. 3.12 (d),(e) and (f)). All the data presented as sample results, fig 3.12, was obtained for a HIFU frequency-of-operation of $f_0 = 1.471$ MHz. The ab-

sence of a bright flash indicates that no plasma induced expansion has formed, as expected for a laser-pulse below the threshold energy value. However, clouds of bubbles of much smaller dimensions form, from location(s) along the path of the focused laser-pulse. The details of the mechanism of formation for these bubbles is not currently fully understood, however, cursory inspection indicates that this activity is acoustic cavitation, from the outset. In this regard, a low energy laser-pulse serves to nucleate acoustic cavitation at a pre-determined instant and location, but crucially, without the large vapour bubble conventionally associated with cavities generated via focused lasers. The size of the cloud that develops, and the speed with which it translates upwards (away from the transducer) is directly related to the intensity of the HIFU exposure, as discussed in §4.3.

Fig. 3.12, rows (a)-(f) summarises the various regimes of combined laser-HIFU cavitation activity that may be achieved with the sonoptic chamber. A short discussion on specific observations from the high-speed sequence representing each regime follows. The optical breakdown threshold for the system, defined as the minimum pulse energy for which plasma flash is observed, was determined to be 5.5 $\pm$ 0.02 mJ, where the error is attributed to instrumental fluctuations in the pulse energies generated (according to the user manual, and consistent with *in-house* power-meter measurements).

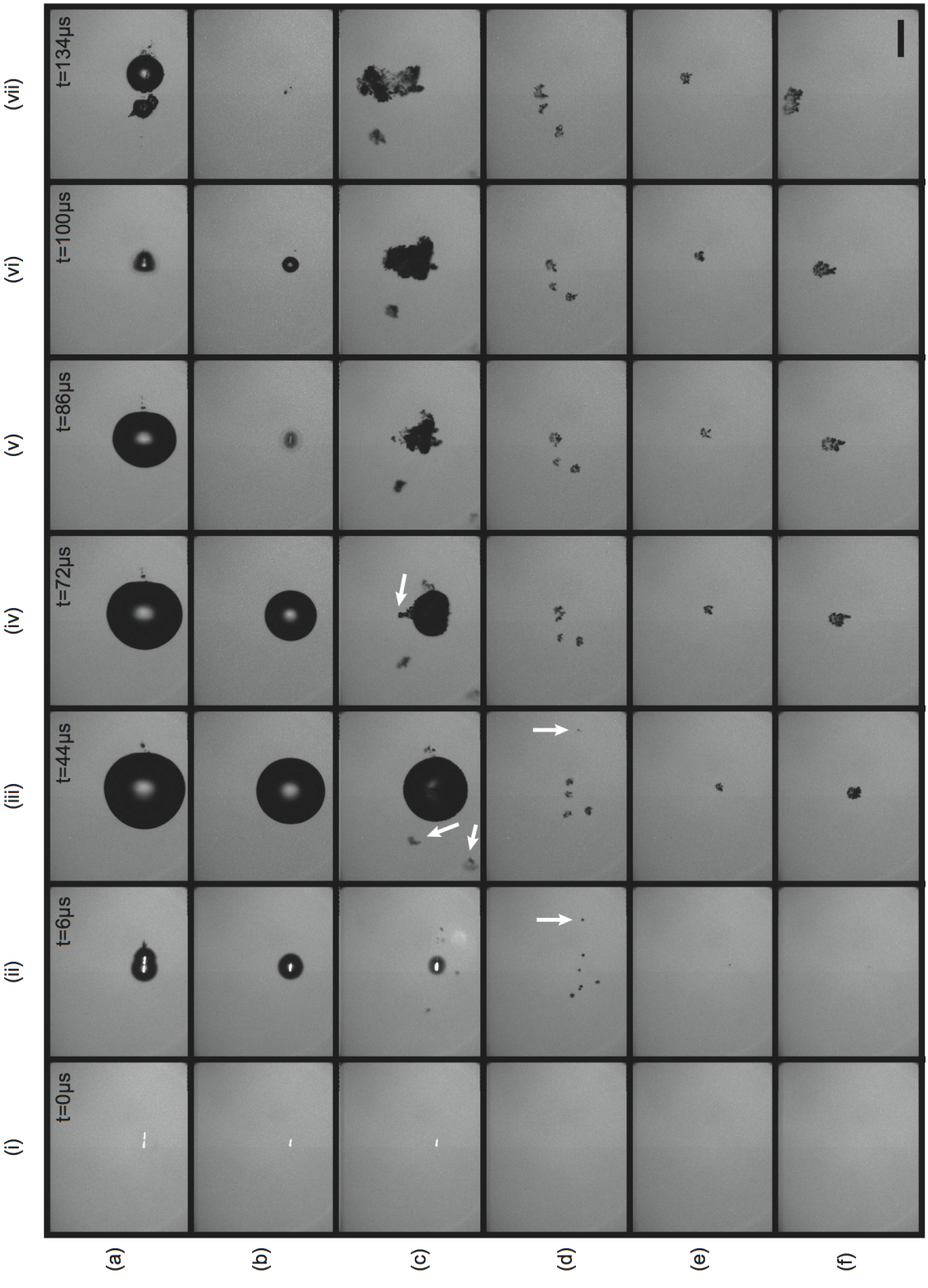

Figure 3.12: Representative frames from high-speed sequences - caption on following page.

Fig. 3.12 **Representative frames from high-speed sequences -** (a) LIC at laser-pulse energy of 6.0 mJ, two plasma regions are created at $t = 0$ μs and lead to asymmetrical expansion and collapse of overlapping bubbles. (b) LIC at laser energy of 5.5 mJ, for which a continuous plasma region, and therefore a single LIC, form. Subsequent symmetrical collapse and rebound oscillations are consistent with reports in the literature. (c) LIC at a laser-pulse energy of 5.5 mJ, in a pre-established ultrasound field of PNP = 8.2 MPa, leads to fragmentation into bubble debris and translation. (d) multiple LNAC clouds, at laser-pulse energy at 1.1 mJ, (e) LNAC at laser-pulse energy at 0.95 mJ, in a pre-established HIFU field of PNP = 4.5 MPa, seeding a single cloud. (f) LNAC at laser energy at 0.90 mJ, in a pre-established HIFU field of PNP = 8.2 MPa, whereby a single nuclei is seeded by the laser and a single cloud develops under the higher intensity HIFU-field. The scale bar is 400 μm.

(i) the 'classic' laser-induced cavity (LIC) fig. 3.12, row (a) is a recording of the cavitation activity that resulted from a 6.0 ± 0.02 mJ laser-pulse focused into the water. In this case two plasma regions form, resulting in two overlapping laser-induced cavities. The asymmetrical behaviour at $t = 134$ μs is therefore attributable to the excess of optical energy, above the threshold breakdown energy value measured for the host medium. Fig. 3.12, row (b) is representative of a conventional LIC, as described in the background section (see §2.2.1). In this case, a 5.5 ± 0.02 mJ pulse is focused into the water, forming a spherical cavity of gas and vapour, that expands for ~ 40 μs to a maximum radius of $R_{max} = 380 \pm 15$ μm, at $t_{max} = 44$ μs. The cavity appears dark on a brighter background as it scatters the flash illumination from the image. Once the bubble reaches R_{max}, the inertia of the water overcomes the internal pressure within the expanded bubble. The bubble then, accelerates into a collapse phase, in fig. 3.12 row (b) from $t \sim 72$ μs. The moment of collapse occurs at $t \sim 84$ μs after laser-incidence, which agrees well with the prediction of eq. 2.8 (see §2.2.1). The internal pressure rises sharply during collapse, which acts as a hard spring to force subsequent re-inflation known as *rebound* (Fujikawa and Akamatsu [46]). Finally at $t \sim 134$ μs the bubble starts to dissolve. It should be noted that the effect of buoyancy on the system bubble at this time-scale is minimal.

(ii) Laser-induced cavitation exposed to HIFU fig. 3.12, row (c) shows an LIC produced with a laser-pulse of energy similar to that in fig. 3.12, row (b). This time, however, a pre-established HIFU burst (f_0 = 1.471 MHz, PNP = 8.2 ± 0.8 MPa) is applied to the cavity throughout the expansion and collapse. The early stages of the dynamics are clearly dominated by LIC, with rapid bubble expansion to an R_{max} = 380 μm, again at t_{max} = 44 μs. The collapse-time of the LIC bubble is also apparently unaffected by the ultrasound. At 6 μs, the plasma flash that initiates the LIC is apparent, however, extra cavitation activity is also nucleated, in the form of two clouds in the pre-focal region of the laser-pulse (arrowed white). The uppermost cloud in the image, increases in size, throughout the observation as it translates upwards, along with the bubble-debris created on collapse of the primary LIC. In contrast, the second cloud to the bottom left of the image, translates from t = 86 μs to the edge of the field-of-view, which can be reconciled to the acoustic pressure gradients in the region (see fig. 3.5). The post-collapse cavitation debris of the LIC, and the upwards translation of the centroid of activity, occur due to the presence of HIFU-radiation focus (see §2.1.4 and §2.2.4)

A further noticeable effect of HIFU exposure is the emergence of a protrusion from the upper edge of the LIC, at t = 72 μs, (arrowed white). In §4.4, this observation is explored in some detail. It will be shown that the radiation-force imposed by the HIFU burst causes an asymmetric collapse on the LIC bubble, which results in *jet-formation*. Careful manipulation of the LIC position relative to the HIFU focus, confers a degree of control to the characteristics of the jets that form.

(iii) Laser-nucleated acoustic cavitation (LNAC) fig. 3.12, rows (d) and (e) demonstrate that incrementally decreasing the laser-pulse energy, acts to nucleate acoustic cavitation more reliably toward the centre of the HIFU focus, for a given PNP. For a pulse-energy of 1.10 mJ, fig. 3.12 row (d) - just below the

breakdown threshold - no plasma formation can be observed, but several clouds are nucleated at various positions along the laser-pulse beam path. For the purpose of collecting data for analysis, this is an unwanted effect as the interactions between clouds from multiple and random nucleation locations, prevent meaningful comparisons and conclusions being made. Further reducing the laser energy to 0.95 mJ, fig. 3.12 row (e), at HIFU PNP = 4.5 MPa, *reduces the number of nucleation points to one*, located on the HIFU propagation axis; i.e. at the geometric centre of the focal volume, where the intensity is a maximum. The reproducible laser-nucleation of a single acoustic cavitation cloud allows direct comparison between observations taken under varying HIFU exposure parameters, and provides the basis for the results presented in §4.2 and §4.3.

Fig. 3.12, row (f) represents a single nucleation event in a HIFU field of PNP = 8.2 MPa. In comparison to the cloud developing in fig. 3.12, row (e), a larger cloud evolves, which translates more rapidly. Both these effects are directly attributable to the higher intensity of the HIFU for this observation. In experimental practise, the precise laser-pulse energy required to nucleate a single cloud in HIFU of a given PNP, is actually a function of the PNP itself. Many tests were undertaken at the start of this project to determine the delicate balance of laser-pulse energy and HIFU intensity, required to reliably generate single clouds.

Further examination of fig. 3.12 row (d), however, reveals several other interesting phenomena. At 6 μs up to 7 cloud-nuclei, of around 10 μm each, are distinguishable. All clouds are under the influence of the acoustic radiation force of the primary-HIFU field, and the inter-cloud forces generated via coupling to the re-radiated acoustic fields, from each of the other clouds. The primary radiation force is responsible for the upwards translation of the clouds closer to the HIFU propagation axis, away from the transducer. The cloud nucleated to the right of the image, however, is seen to translate further to the right, at t = 44 μs (arrowed white). Comparison to fig. 3.5, indicates that this translation occurs along the pressure gradient that exists at this position in the HIFU focus.

At t = 44 μs the three clouds to the top left have already merged to form a single cloud, indicating attractive inter-cloud forces acting on clouds in close proximity. This effect can again be observed between the two central clouds at t = $72 - 134$ μs, where the translation towards merging is slower on account of the clouds being initially further apart.

3.8.1 Shock-waves from LICs

The frames selected from the high-speed sequences of fig. 3.12, best represent the bubble activity in the various cavitation regimes. Other frames from the sequence, not included, reveal the effects of shock-waves in the sonoptic chamber that have little consequence on the results that follow, but are discussed here for completeness. It is well known from previous LIC experiments (see §2.2.1), that shock-waves are emitted: (i) at laser-absorption/plasma formation and (ii) at LIC collapse. Fig. 3.13 shows radial shock-wave propagation from the laser-focus equivalent to (i) for the experimental configuration here. This sequence was recorded with the SIM camera (see §3.6) at inter-frame time of 100 ns, and exposure time 25 ns, representing the most rapid framing used in this work. Specifically the shock-wave is apparent as a dark shadow radiating form the plasma location (arrowed white in the direction of propagation). The shadow effect is due to the refractive index change due to the local pressure fluctuation. From the three frames which the shock-wave is apparent the propagation speed maybe estimated as $\sim$ 1700 m/s.

Fig. 3.14 (a) represents the hydrophone trace recorded for the LIC of 3.14 (b), with the tip located in the cavitation chamber. This trace is dominated by four distinct shock-wave profiles, the detail of which is provided in the insets of fig. 3.14 (a). The first at 189 μs corresponds to the moment of laser-pulse absorption t_0 and is the hydrophone recording of the shock wave visualized in fig. 3.13. The leading edge of this profile is a sharp positive pressure, followed by a slightly extend tensile phase. 107 μs later t_{R1} is detected. Assuming a speed of sound of

1500 m/s, this equates to a total propagation distance of 160 mm, or a reflection from an object at 80 mm from the laser focus. Consideration of the sonoptic chamber reveals that the reflecting surface is provided by the HIFU transducer (see 3.3.1), which is a spherically curved surface. This acts to effectively reflect and refocus back the radially propagating 'shock-wave' to the plasma location. This analysis indicates that the *acoustic transient* generated on laser absorption only travels at supersonic speeds, fig. 3.13, for a very short time.

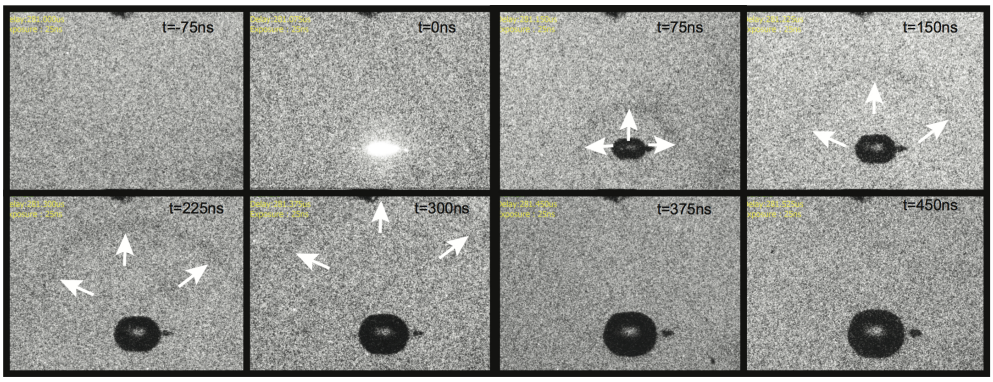

Figure 3.13: Shock wave from optical breakdown - Inter-frame times of 100ns and an exposure of 25ns

At $t = 267\ \mu s$ a further shock-wave is detected, which corresponds to the time collapse, t_c, of the LIC. This acoustic transient is characterized by a leading tensile phase consistent with collapse event. Again, 107 μs later, this transient is detected following reflection from the surface of the transducer. Smaller features detected with the trace may be attributed to the walls of the cavitation chamber, but are less prominent as they are not refocused from the plane surfaces.

Fig. 3.14 (b) are frames selected from the high-speed sequence of the LIC generated to represent the secondary excitation effects of the acoustic transients described on the recorded bubble activity, note no HIFU is present. The effect of the acoustic transients is a brief inflation of the debris bubbles toward the end of the sequence. For laser-nucleated acoustic cavitation (LNAC) the laser-energy is below the breakdown threshold value, so no plasma is observed. As such the acoustic transients associated with plasma formation and collapse of the primary

LIC have are not generated in this regime. The jetting observations of §4.4, occur over a time frame less than that required for the reflected acoustic transients to reach the cavitation chamber. So for all the results section that follow, any influence of acoustic transiences can be dismissed. Nonetheless they provided some interesting insights to the acoustic properties of the sonoptic chamber.

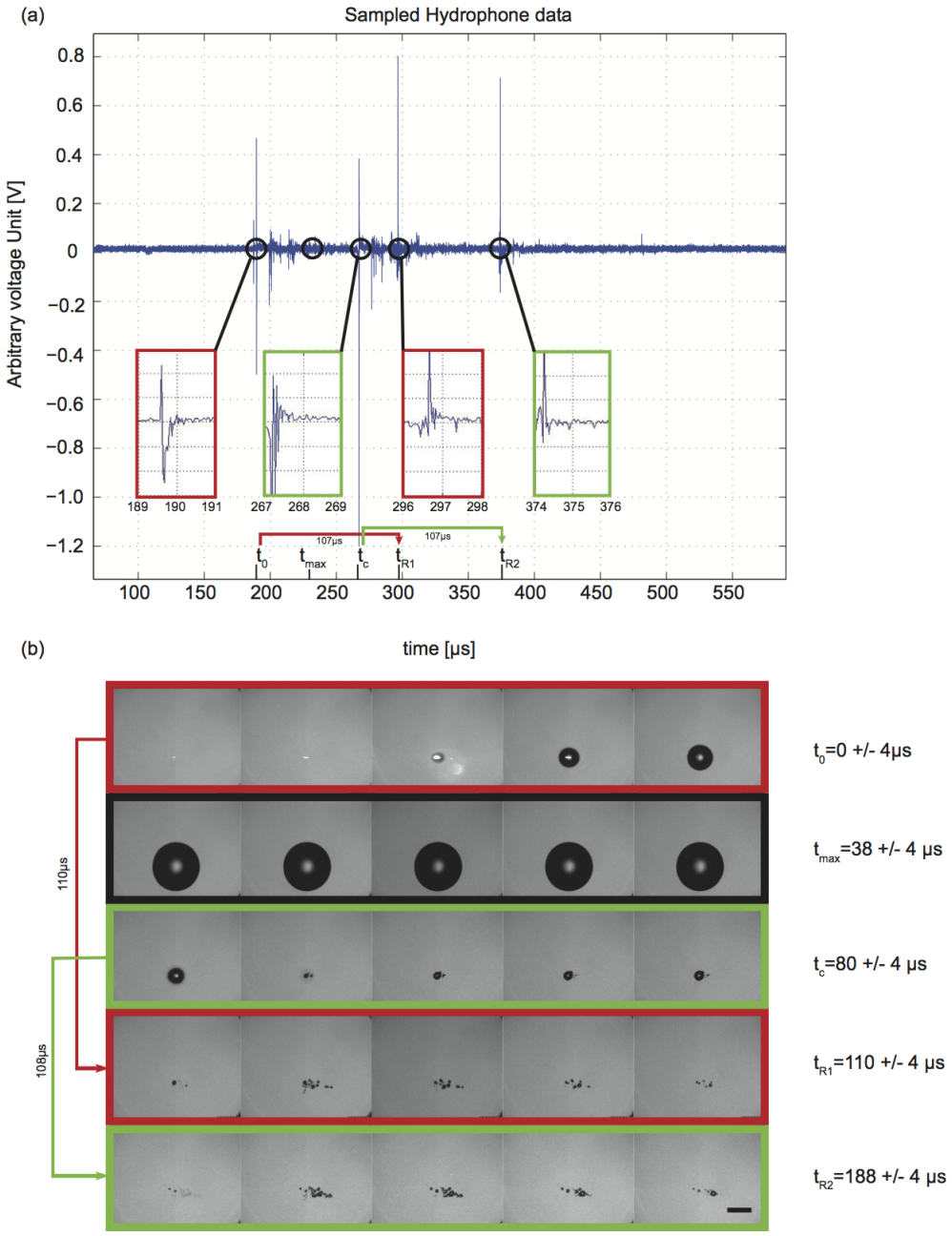

Figure 3.14: Hydrophone detection of shock-wave - hydrophone recording of the shock-waves produced by the formation and the collapse of an LIC. t_0 time of laser-absorption which provides the first shock wave (red). t_c is the time of collapse which produces a second shock-wave (green). t_{R1} is the time at which the first shock-wave reflects and refocuses back to the cavitation chamber. Correspondingly t_{R2} is the time at which the collapse shock-wave returns to the field-of-view.

4

Results

4.1 Overview of result sections

The following chapter provides a detailed analysis of various observations discussed in §3.8. Sections 4.2 and 4.3 summarise LNAC cloud dynamic, specifically oscillatory behaviour and the translational response to the primary HIFU field. In §4.2, acoustic recordings are taken in parallel to the high-speed data, allowing direct correlation between the two. For these results, a HIFU frequency of $f_0 = 0.521$ MHz is employed to fully resolve dynamics around the half sub-harmonic, at an imaging frame rate of 1 Mfps, thus satisfying the Nyquist sampling criterion. Section 4.3, describes the rate of cloud translation as a function of the HIFU intensity. These experiments were not constrained by an equivalent sampling rate requirement, and were therefore undertaken with HIFU of frequency $f_0 = 1.471$ MHz, which provided a much larger intensity range for exploration. Section 4.4, focuses on the action of HIFU radiation force upon LIC bubbles, formed from laser-pulses of above the breakdown threshold energy, entering the collapse phase. Again, comparatively large HIFU PNPs were determined to provide the most pronounced effects and as such, HIFU of $f_0 = 1.471$ MHz was employed. The dependence of the resulting collapse asymmetry and the jets that result, on the relative position to the HIFU focus and the intensity of the field is described.

4.2 Cavitation cloud oscillation dynamics and acoustic emissions

4.2.1 Overview

The ability to nucleate single acoustic cavitation clouds and observe at very high frame-rates, paves the way for research into the evolution of cavitation clouds during the early, formative phases, in HIFU (and ultrasound generally). Detection of cavitation occurrence in tissue is, however, limited to acoustic detection techniques. In current FUS procedures, single elements in phased array transducers (see §2.1.6) are set to receive-mode, to detect characteristic acoustic emissions, for avoidance purposes. In the brain application, sensitive hydrophone devices are required to detect these signals through the skull, particularly as cavitation is a significant issue at the low frequencies typically employed (see 3).

For this work, a custom fabricated hydrophone was designed and constructed for the purpose of detecting specific acoustic emission frequency content, for direct correlation to the high-speed observation of resolved cavitation clouds. To date, the seminal experimental study on the topic of cavitation acoustic emissions is described in the paper entitled *'Sub-harmonic route to acoustic chaos'* by Lauterborn and Cramer [75]. In this study a cylindrical transducer with a resonance frequency, f_0 of 23.56 kHz was used, to produce cavitation activity in the high-intensity acoustic standing field generated in its interior. The drive amplitude was gradually increased over a duration of 250ms ($\sim$ 6000 cycles) and the acoustic noise produced recorded via a broadband hydrophone for analysis. The sub-fundamental emitted frequencies (f_e's $< f_0$) were particularly investigated. At the lower intensities, at the beginning of the exposure, that region of the emitted spectrum was dominated by the half-harmonic line (see 4.2), at $f_e =$ 11.78 kHz. At intermediate intensities, a bifurcation in this signal to emissions to odd sub-harmonics, given by n$f_0/3$ and n$f_0/8$ lines was reported. Increasing the

drive amplitude further resulted in n$f_0/4$ lines, which descended into the chaotic broadband noise associated with inertial cavitation (see §2.2.2), at the highest amplitudes, toward the end of the 250 ms exposure.

The current work extends the principle of monitoring the acoustic emissions with the significant capability of correlating to them optically observed and resolved dynamics, via the laser-nucleated technique. There is also the significant advantage of observing cavitation activity from inception, through the early stages of evolution, in a typical HIFU frequency exposure at a constant pressure amplitude throughout. This is distinct from the Lauterborn and Cramer work, in that cavitation clouds do already exist from a previous, lower intensity period of a continuous exposure. Moreover the propagating wave configuration facilitated by the sonoptic chamber is more representative of a FUS procedure.

The results presented below detail cloud oscillation dynamics that become established within 100 acoustic cycles of the nucleation event, that are directly correlated to specific features in the acoustic emission spectrum, detected with the PCD hydrophone device (see §3.7). Laser-nucleation permits optical interrogation at 1 Mfps at a HIFU frequency of 0.521 MHz, and ensures acoustic data is collected from the observed cloud in isolation. The effects of increasing the intensity (PNP) of the exposure, on cloud dynamics and emissions is assessed, in terms of the degree of non-linearity of the response. Analysis of cloud response to HIFU insonation is therefore conducted via three approaches:

(i) The frequency of bubble-ensemble oscillation, extracted from the high-speed imaging sequences. For this approach, a 'dark-pixel' counting algorithm (see Appendix 6.1) is implemented to the entire high-speed image sequence of a cloud under a given HIFU exposure, to evaluate the temporal dependence of bubble-ensemble response. An FFT (see Appendix 6.3) generated a spectrum taken to represent the frequency of ensemble oscillation.

(ii) The frequency content of the acoustic emissions detected. To achieve this, the acoustic signal was recorded via the PCD (§3.7) at a sampling rate of 1Gs/s

(10^9 samples per second) or more, over the duration of high-speed observation. The signal was then transformed via FFT to deliver a power spectrum exposing the *acoustic signature frequencies* for each regime of cloud response.

(iii) Finally, the acoustic emission spectra were compared to a single bubble model based on the Rayleigh-Plesset equation (see §2.2.3), of a *selected quiescent radius* comparable to that of the cloud. Single bubble models have been used previously (Lauterborn and Cramer [75]) to assess cloud 'breathing modes' for the central region of a 'streamer' in an ultrasound cleaning bath.

4.2.2 Cloud oscillations and acoustic emissions in response to increasing HIFU intensity

Experimental parameters the laser was incident with an energy of 0.9 ± 0.1 mJ (< 0.1 mJ adjustments for each PNP) (see §3.8), to the focal region of the pre-established HIFU field. Crucially, this is below the breakdown threshold for the host medium of de-ionised water, which avoids the comparatively large, plasma-mediated, vapour bubble. The transducer was driven at $f_0 = 0.521$ MHz. A total of 160 HIFU acoustic cycles were generated, with the laser-pulse incident after 70 μs, 15 μs (~ 22 cycles) to allow for transducer 'ring-up' to the required pressure amplitude, and 55 μs for the ultrasound to reach the focus. High-speed camera operation is triggered to capture a few frames prior to nucleation of cavitation activity, such that cloud development is observed from inception through ~ 50 HIFU cycles.

High speed observations fig. 4.1 (a) and (c) are sample high-speed imaging data, recorded at 1 Mfps, illustrating cloud behaviour in response to HIFU. They show cavitation dynamics at PNP $= 0.72 \pm 0.1$ (instrument error, according to manufacturer) and at 1.04 ± 0.1 MPa, respectively. These are sequential images acquired over a duration of 12 μs, approximately 75 μs following laser-nucleation, during which the cloud has become established and initiated periodic

behaviour. Slight upward translation is attributable to the acoustic radiation force of the HIFU insonation, as buoyancy is negligible over the time-scale of the observations. Inspection indicates that the quiescent component bubble radius is comparable for both clouds, as expected for acoustic cavitation at a given driving frequency (Leighton [80]) (see §2.2.2). Both coalescence of component bubbles (during expansion), and fragmentation (following collapse), within the clouds is observed. The latter is the mechanism by which the number of constituent bubbles increases, at a rate dependent on the intensity of the HIFU field.

Several 10's of μs following laser-nucleation, quasi-spherical breathing mode oscillations for the bubble-ensembles, closely related to the dynamics of the individual component bubbles, are apparent. The effect is particularly evident toward the latter stages of the movie representation of the high-speed sequences sampled for fig. 4.1 (a) and (c), (available as supplemental material in the CD accompanying this thesis). It is well known that oscillating bubbles exert either mutually attractive or repulsive forces via coupling to the radiated acoustic field to other bubbles in the vicinity, such as secondary Bjerknes effects (see §2.2.4). This applies to oscillating bubbles that are distal relative to their radii. For the clouds of fig. 4.1 the constituent bubbles (formed from the collapse of previous constituent bubbles) are in very close proximity from the outset. As such the interaction between neighbouring bubbles can be attributed to the physical action of the oscillations themselves. For example the collapse of any individual will act to draw it nearest neighbour closer. If extended to all the bubbles within the ensemble oscillation in phase, this yields an overall compression of the cloud. In this manner, the oscillations of the component bubbles and the oscillations of the bubble-ensembles can be considered synonymous.

Fig. 4.1 (a) [(iv), (viii) and (xii)] depict consecutive compressive phases, for the cloud at lower PNP = 0.72 MPa, with approximately one HIFU cycle propagating during the time taken to acquire two high-speed images. This constitutes

an ensemble response at $f_0/2$, the half-harmonic of the driving frequency, also known as period-doubling (Lauterborn and Cramer [75], Lauterborn and Kurz [76], Leighton [80], Parlitz *et al.* [102]). Fig. 4.1 (c) is the equivalent high-speed data for a cloud nucleated at higher PNP = 1.04 MPa, whereby a larger bubble-ensemble has developed due to increased levels of fragmentation over the preceding 75 μs. As well as the HIFU intensity-dependent size of the clouds of fig. 4.1 (a) and (c), a further notable difference is the additional deflation phases, captured in fig. 4.1 (c) [(i), (iii), (v), (vii), (ix) and (xi)]. The full sequence recorded for the cloud at higher PNP (available in movie format in the CD accompanying the thesis), clearly illustrates the ensemble pulsating at more than one frequency.

To quantify the ensemble oscillations, a dark-pixel counting algorithm (see Appendix 6.1) is implemented to each of the 100 images captured within a high-speed sequence. This effectively yields a *summed bubble area* variation with time, for every observation of cloud evolution, at each PNP investigated. This approach does not explicitly distinguish between ensemble response and constituent bubble dynamics. However, for the high void-fraction clouds being investigated, constituent bubble dynamics and ensemble response are synonymous, as discussed previously. For inflation phases of the cloud this is a valid approximation. For compressional phases sum of the constituent bubble may have collapsed to sizes below the resolution of the optical set-up. As such the summed bubble area will be under estimate for the size of the cloud. Nonetheless, the application of a Fast Fourier Transform (FFT) to the summed bubble area-time curve from each sequence, is taken to provide the frequency of the ensemble oscillations, at the given HIFU PNP. The *resulting high-speed sequence spectra* for the clouds of fig. 4.1 (a) and (c) are presented in red (inset top left) of fig. 4.1 (b) and (d), for direct comparison to the frequency content of the acoustic emissions (green) collected from each of the clouds. A summary of all experimentally detected acoustic and high-speed sequence spectra spectral data is provided in fig. 4.3 below. The signal

resolution for this analysis is inherently limited by the number of samples available (100 frames per high-speed sequence). Moreover, the frequency of oscillation signal will only become available once the cloud has entered its periodic response phase, typically 20-30 μs following the initial nucleation event. Nonetheless at lower PNP = 0.72 MPa a clear oscillation frequency at 260 kHz is apparent. At the higher PNP = 1.04 MPa, the oscillation signal is not so clear, but two small peaks can be observed at 175 and 350 kHz.

Acoustic detection The acoustic emissions from individual clouds are detected for the duration of high-speed observation, via the PCD device described (see §3.7). Fig. 4.1 (e) is an FFT of a PCD recording of the primary HIFU field at PNP = 1.04 MPa, without the nucleation of cavitation activity (i.e. no laser-pulse incident). High-speed observation showed that no cavitation was present, within the field-of-view. The fundamental driving frequency at $f_0 = 0.521$ MHz is the dominant feature in this spectrum, with a smaller peak at $2f_0$, the second harmonic. The potential influence of the higher harmonics on the cavitation cloud behaviour is discussed below.

The green traces of fig. 4.1 (b) and (d) are the spectra of the acoustic emissions collected for the clouds of fig. 4.1 (a) and (c), respectively. The sub-fundamental peaks (arrowed black) are only detected when cavitation activity is nucleated with a laser-pulse, with structure detail dependent on the PNP of the HIFU field driving the activity. As such, we refer to the frequency of these features as emitted frequencies, f_e, for the purposes of this thesis. The cloud at lower intensity exhibits $f_e \approx 260$ kHz (7 kHz FWHM; acoustic data), which corresponds to the $f_0/2$ sub-harmonic. Fig. 4.1 (d) reveals spectral lines at $f_e \approx 175$ (40 kHz FWHM) and 350 kHz (30 kHz FWHM), which correspond to $f_0/3$ and $2f_0/3$ respectively, emitted from the cloud depicted in fig. 4.1 (c).

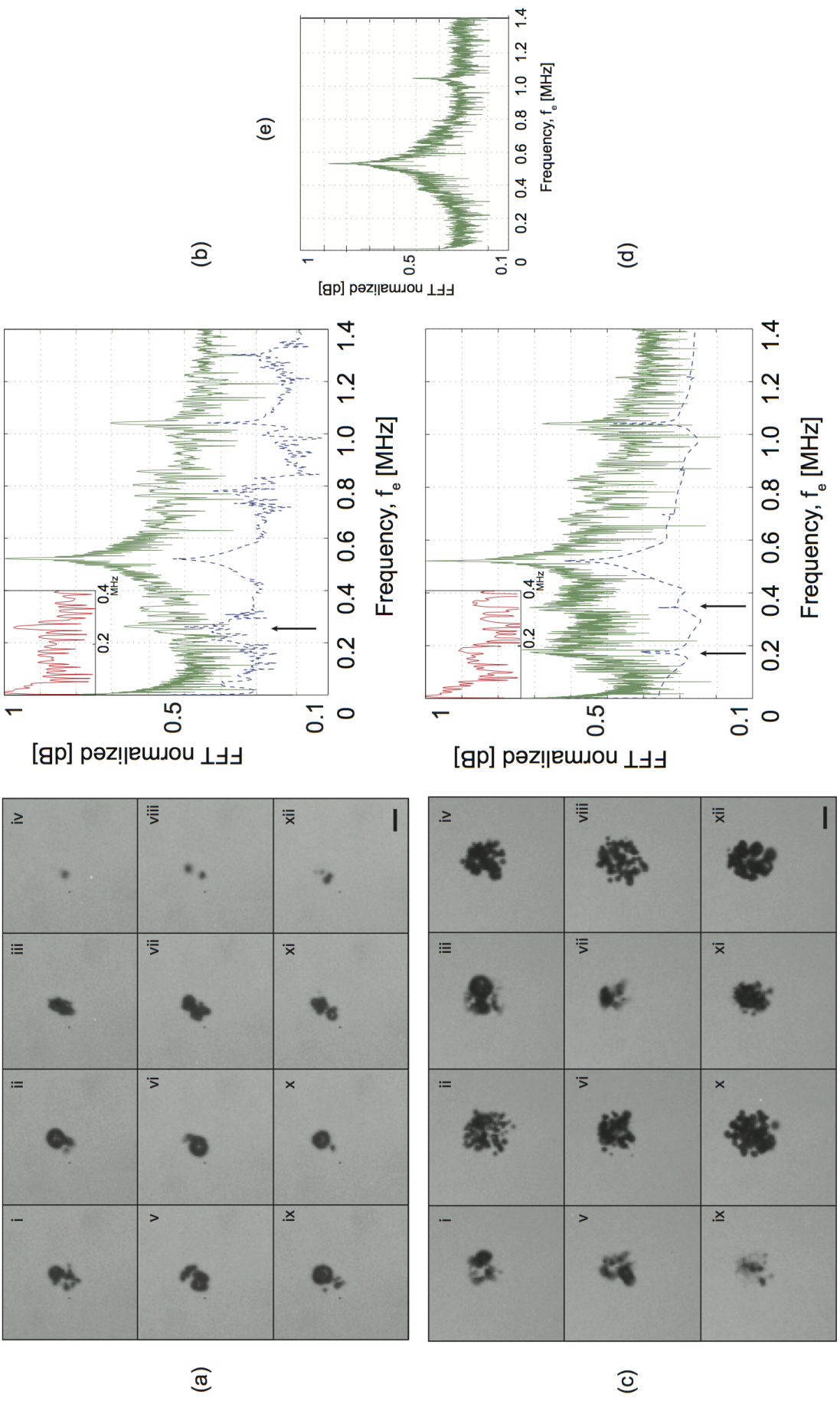

Figure 4.1: High-speed sequences and oscillation analysis - caption on following page.

High-speed sequences and oscillation analysis - Consecutive frames extracted from high-speed sequences recorded at 1 Mfps, of cavitation clouds evolving in HIFU in (a) a stable regime at PNP = 0.72 MPa and (c) a more pronounced non-linear regime at PNP = 1.04 MPa, $\sim 75\ \mu s$ following the laser-nucleation event. (b) and (d) are FFTs of the PCD signal (green) collected from the clouds of fig. (a) and (c), respectively. The inset (red, at same frequency scale) represents the ensemble dynamics deduced from a FFT of the dependence of 'summed bubble area' (dark pixel count) on time, throughout the high-speed imaging sequence. An FFT of the Rayleigh-Plesset radius-time curves for a single bubble of selected R_0 (blue), under equivalent ultrasonic conditions is also presented. (e) control experiment with no cavitation activity nucleated, depicting the PCD detection of the primary HIFU field. Scale bar: 50 μm.

This 'frequency-bifurcation' in the acoustic emission for increasing HIFU PNP is strongly reminiscent of the observation made by Lauterborn and Cramer [75]. Extending from their conclusions, the bifurcation is therefore attributable to a transition for the HIFU-cloud system to a regime of more pronounced non-linearity, at higher PNP (Gerold *et al.* [51]).

4.2.3 Analysis

Fig. 4.1 (b) and (d) demonstrate excellent agreement between the sub-harmonic structure of the high-speed sequence spectra and the acoustic emissions. This indicates a direct correlation between the two detection modalities.

Single bubble Rayleigh-Plesset model To investigate the origin of the emitted acoustic frequency content, a Rayleigh-Plesset (RP) formulation for a single bubble model (see eq. 4.1, see §2.2.3) is implemented (Lauterborn and Kurz [76], Leighton [80]). This form of analysis for cloud breathing modes has been undertaken previously for the central region of a 'streamer' in the standing field of an acoustic cleaning bath (Lauterborn and Kurz [76]). A remarkable degree of agreement between the time-varying radius of the cloud, observed at 0.1 Mfps at a driving frequency of 12.96 kHz, and those obtained from an RP formulation was demonstrated. Accordingly, the experimental data here is presented in parallel with equivalent model predictions, for a *selected quiescent radius*, R_0, that

matches the features of the experimentally measured frequency spectra to the single bubble model oscillations.

$$R\ddot{R} + \frac{3\dot{R}^2}{2} = \frac{1}{\rho}((p_0 + \frac{2\sigma}{R_0} - p_v)(\frac{R_0}{R})^{3\kappa} + p_v - \frac{2\sigma}{R} - \frac{4\eta\dot{R}}{R} - p_0 - P(t)) \quad (4.1)$$

where R is the time-varying radius of the bubble undergoing oscillation and R_0 is a selected quiescent radius, $p_0 = 100$ kPa is the hydrostatic pressure, $p_v = 2.33kPa$ and $\kappa = 5/3$ are the vapour pressure and polytropic exponent of the gas within the bubble. $\rho = 10^3\ kg/m^3$, $\eta = 72 \times 10^{-3}$ N/m and $\sigma = 0.894 \times 10^{-3}$ Pa.s are the density, surface tension and liquid viscosity of the host medium, respectively. $P(t)$ represents the HIFU excitation, given the form

$$P(t) = PNPsin(2\pi f_0 t) \quad (4.2)$$

at frequency f_0 and PNP amplitude, matching those of the experiments. An analysis of the appropriateness of using a linear expression for the HIFU insonation, is provided below.

Specifically, quiescent R_0 radii are implicated by fitting RP model sub-fundamental spectral features to the measured emitted frequencies, for each PNP investigated. Example model spectra from this approach are presented (blue dash) in fig. 4.1 (b) and (d), whereby R_0's of 20.2 and 26.3 μm yield sub-fundamental structure at f_e's of 260 kHz for a PNP of 0.72 MPa, and 175 and 350 kHz for 1.04 MPa (at $f_0 = 0.521$ MHz). A robustness analysis confirms that variation (including in combination) of the other parameters of eq. 4.1 is unlikely to deliver spectral features that resemble those experimentally observed. Sample analysis results for variation of host medium viscosity, η and surface tension, σ are available below.

The dependence of the model R_0's required to deliver the experimental spectra structure on HIFU PNP, is given in fig. 4.2 (blue line). The PNP amplitude is both an input parameter to the RP model via the HIFU excitation expression of eq. 4.2, and the experimental factor that determines the rate of fragmentation

within the bubble ensemble, and therefore the time-averaged size of the observed clouds. It is not possible to deduce a quiescent radius for the clouds explicitly from the high-speed sequences. For comparative purposes however, approximations of maximum and minimum cloud radii are also represented, fig. 4.2 (red data), using the highest and lowest values of the dark-pixel count, averaged over all the high-speed sequences acquired at each PNP investigated.

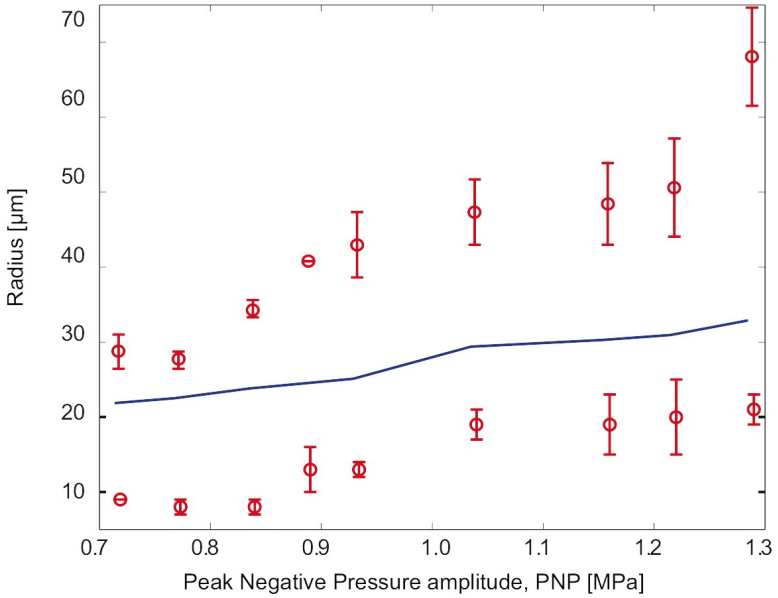

Figure 4.2: Selected model R_0 vs. PNP amplitude - Variation of model R_0 (blue line) with PNP amplitude required to yield frequency content from the RP model oscillations matching those emitted from the cavitation clouds, detected with the PCD. The experimental data (red circles) depicts the maximum and minimum radii approximations for the clouds, as discussed in the text. Error bars are standard deviation for the approximate cloud size at each PNP ($n \geq 6$).

During this process, dark pixels are rearranged into a circle, to homogenize cloud morphologies and effectively assume a void fraction of ~ 1, which is reasonable for the ensemble at maximal expansion. The approximation for the minimum cloud radius should not be interpreted literally as some of the collapsed constituent bubbles within the ensemble are likely to be below the imaging resolution for the high-speed camera set-up. Nonetheless, the comparison between the experimental radii approximations and selected single-bubble model R_0's, which were coupled through the PCD spectra for the acoustic emissions, is compelling,

and may be taken to indicate that the frequency content of the acoustic emissions originate from the response of the cloud, acting as a bubble-ensemble.

Fig. 4.3 represents an overview of the experimental acoustic and high-speed sequence, and RP model, spectral information obtained for each PNP investigated. The bifurcation of f_e, both in terms of the emitted acoustic frequencies and the ensemble oscillations, at PNP = 0.78 MPa is clearly visible. The blue dotted region represents sub-fundamental RP model oscillation frequencies matched to the experimentally detected f_e values, which agrees well with both the bifurcation PNP threshold, and the degree of frequency splitting throughout the bifurcation transition.

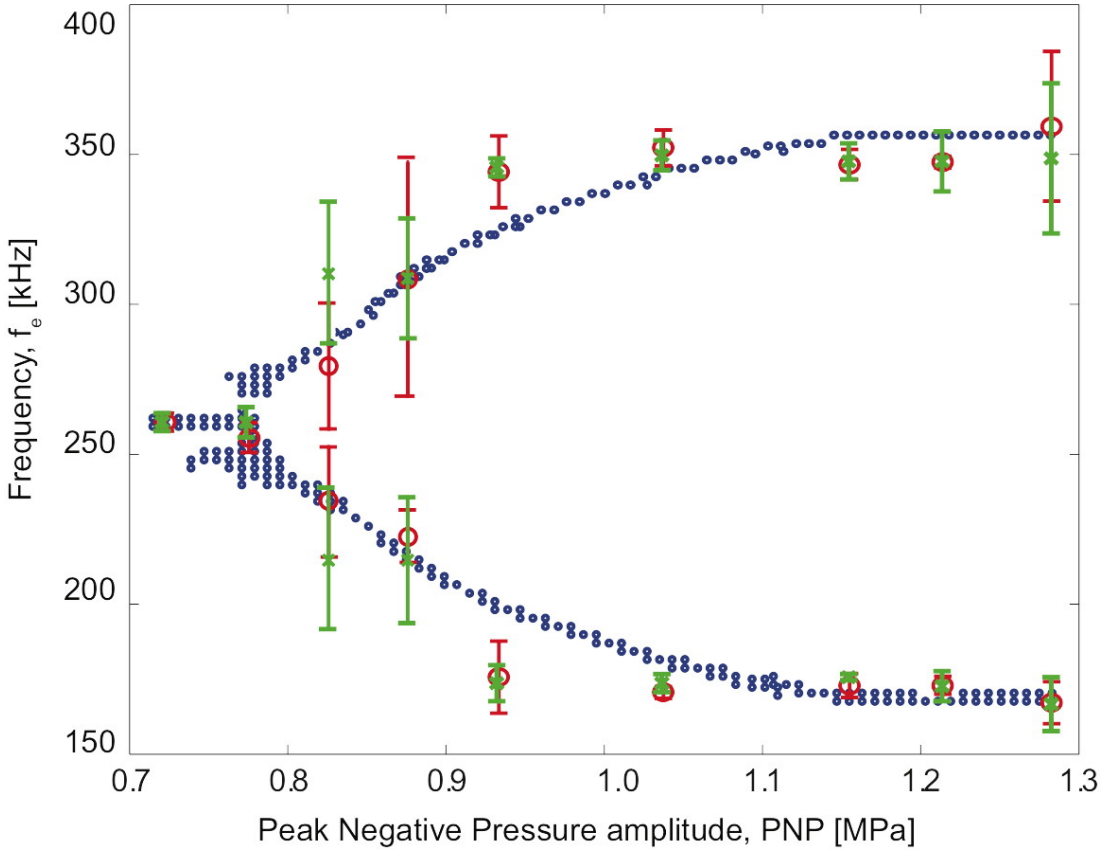

Figure 4.3: Summary of all experimental data - All experimental frequency content information obtained, including PCD detection of acoustic emissions (green) and high-speed sequence analysis of ensemble oscillation dynamics (red), for each of the eight PNP's investigated. Error bars are the standard deviation for each data set, with n $\geq$ 6. The blue dots represent the spectral features above a threshold value derived from the Rayleigh-Plesset model, fitted with selected values of R_0 (see fig. 4.2).

Rayleigh-Plesset robustness analysis To ensure the sub-fundamental spectral features could not arise from the variation of parameters (including in combination) in the RP model for single bubble dynamics, other than R_0 for a given HIFU PNP amplitude, a robustness analysis is conducted.

The matrices of model spectra are presented for the R_0's and PNP's of interest, through parameter space for surface tension σ, and liquid viscosity η, fig. 4.4 (a) and (b), respectively, are presented to demonstrate proof-of-principle. A short discussion on the relevance of the parameters to the observations follows.

The surface tension of a liquid is related to its temperature, such that the range presented corresponds to water at 0 °C ($\sigma = 76 \times 10^{-3}$ N/m) and > 100 °C ($\sigma = 50 \times 10^{-3}$ N/m). Although collapsing cavities are known to generate high core temperatures, including in multi-bubble configurations (McNamara *et al.* [87]), the energy is very localised both spatially and temporally, to the location and moment of collapse. We therefore assume room temperature of 25 °C and thus surface tension, $\sigma = 72 \times 10^{-3}$ N/m, for eq. 4.1.

Increasing the host medium viscosity acts to suppress the amplitude of all spectral features, fig. 4.4 (b), as expected. In the extremity, where $\eta = 10$ Pa.s, the model single bubble predominantly oscillates at the fundamental driving frequency, $f_0 = 0.521$ MHz, irrespective of R_0 or PNP. The viscosity of tissue is often approximated to that of glycerol, $\eta_{gl} \sim 1.5$ Pa.s (Segur and Oberstar [111]). However, whole blood has viscosity, $\eta_{wb} \sim 4 \times 10^{-3}$Pa.s (Rosenson *et al.* [109]), a region of parameter space for which the sub-fundamental frequency structure is apparent across the full range of R_0's and PNP reported. As such, the signature acoustic emissions identified may have application for cavitation clouds forming within the vasculature, under HIFU exposure.

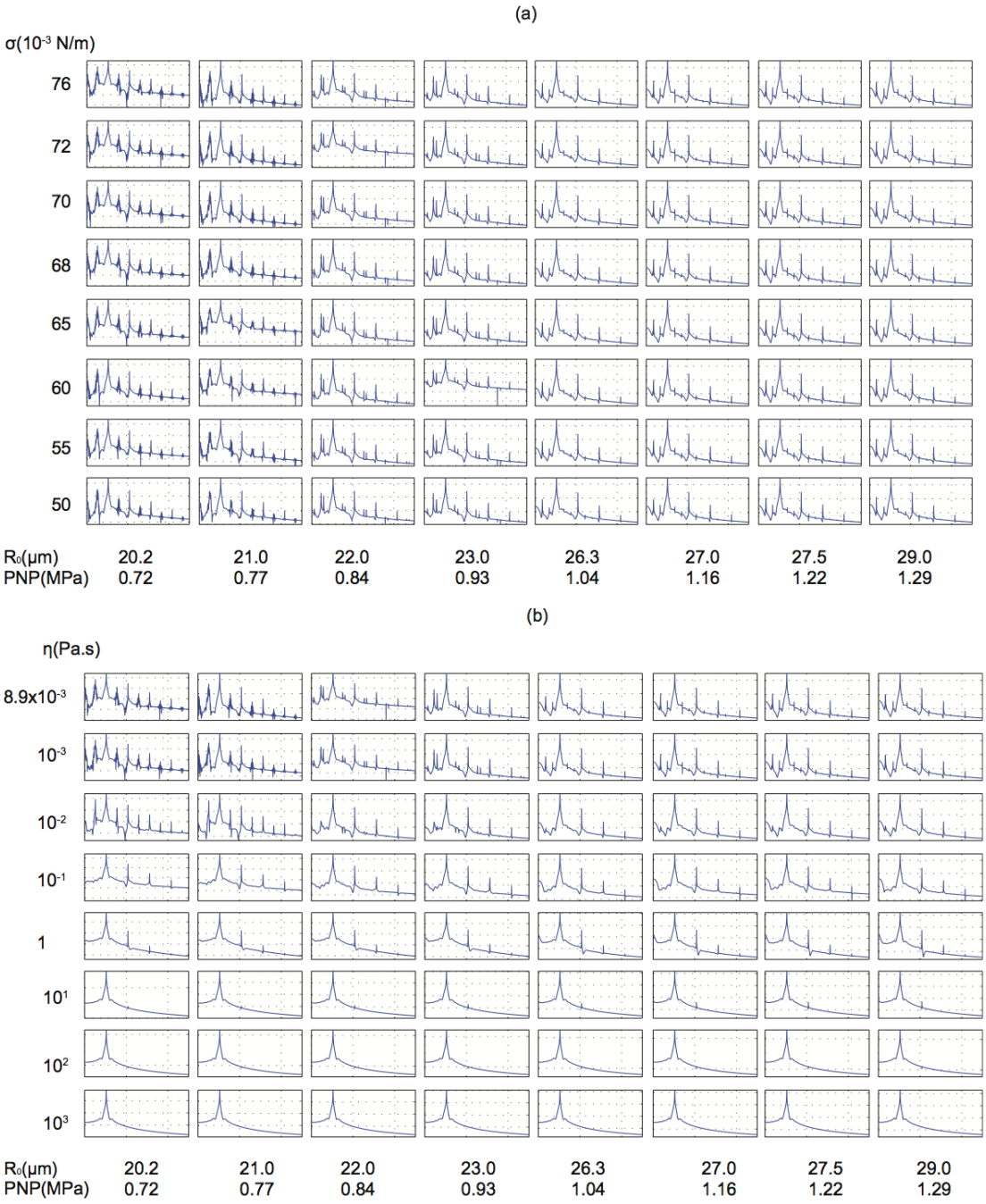

Figure 4.4: Robustness analysis - (a) for surface tension, σ ranging from 50×10^{-3} to 76×10^{-3} N/m, over the values of selected R_0 and PNP of interest. (b) Robustness analysis for liquid viscosity, η ranging from 8.9×10^{-3} to 1×10^{3} Pa.s. Power (dB) spectra are presented in the range of 0-2.5 MHz.

4.2.4 Assumption of HIFU non-linearity

The expression used for the HIFU excitation, eq. 4.2, assumes a linear monochromatic wave. It is well known that ultrasound at therapeutic intensities is often non-linear with potentially strong high frequency harmonic components. In terms of cavitation dynamics, these additional components may result in extraneous oscillations that need to be eliminated as a possible mechanism for the ensemble response observations reported. The HIFU field was analysed for non-linear components. The assumption of linearity for the HIFU expression in the model can be justified by factoring high frequency terms into the RP equation, at the experimentally determined levels (see eq. 4.3). This showed minimal qualitative changes of the resulting spectra. Fig. 4.5 (a-c) are *in-situ* fibre-optic hydrophone recordings of HIFU bursts representative of those used to excite cavitation activity, at PNP = 0.72, 1.04 and 1.29 MPa, representative of the range used in this work. Cursory inspection indicates that the positive pressure amplitude is of approximately the same magnitude as the negative pressure amplitude, commonly taken as an indication of linearity (see §2.1.5). Fig. 4.5 (d-f) are the associated amplitude spectra in the frequency domain, generated by FFT implementation, which reveal slight higher frequency components exist at $2f_0$ and $3f_0$, increasing for the larger pressure amplitudes as might be expected.

To determine that the harmonic components do not have a significant effect on the model oscillation dynamics, eq. 4.2 are modified to include higher frequency terms at the level recorded in the spectra of fig. 4.5 (d-f), according to

$$P(t) = \sum_n a_n P_0 sin(2\pi n f_0 t) \tag{4.3}$$

where n denotes the harmonic and a_n is a scaling factor representing the amplitude of the component. Implementing the RP model with eq. 4.3 as the excitation expression, in a HIFU field of PNP = 1.29 MPa (the highest pressure amplitude used, and therefore most non-linear HIFU generated) for the funda-

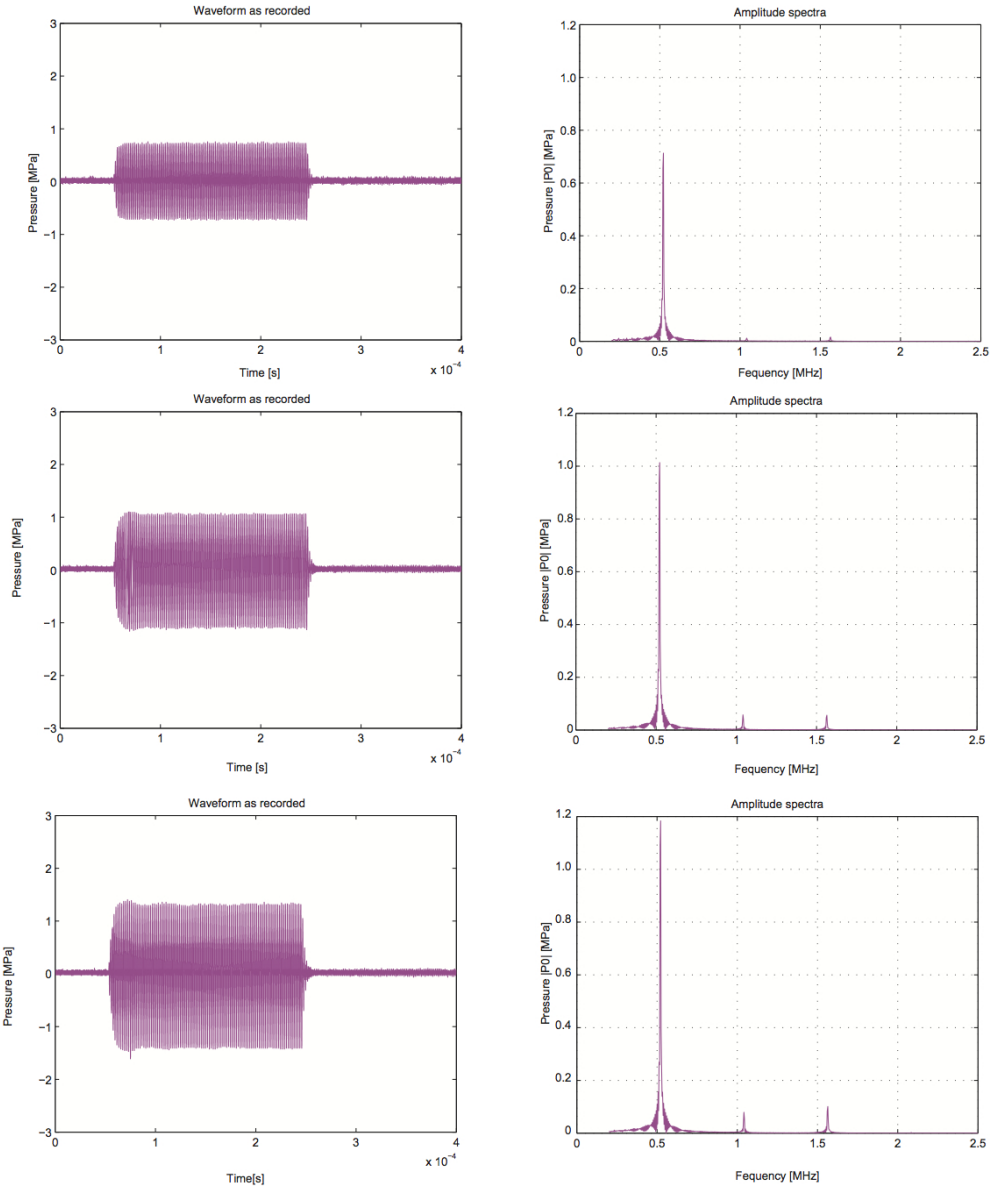

Figure 4.5: Non-linearities in HIFU field - Pressure measurements recorded at the HIFU focus at PNP amplitude of (a) 0.72 MPa, (b) 1.04 MPa and (c) 1.29 MPa. (d-f) Associated amplitude spectra from 0 2.5 MHz after Fast Fourier Transform

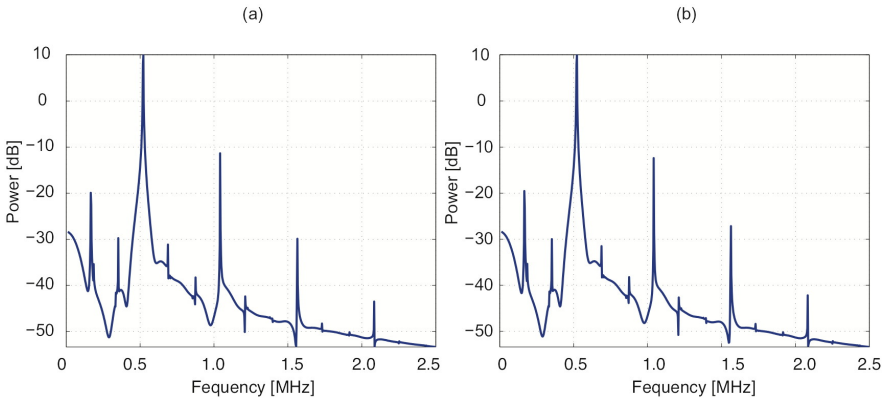

Figure 4.6: Non-linearities input in the RP model - Rayleigh-Plesset model spectra for bubble oscillations HIFU of PNP = 1.29 MPa (a) under a linear approximation of HIFU, according to equation 4.2 of the main manuscript and (b) incorporating higher frequency harmonic components via equation 4.3 above, according to the spectrum of fig. 4.5 (f).

mental frequency $f_0 = 0.521$ MHz yields the bubble-oscillation spectrum of fig. 4.6 (b). Also included as fig. 4.6 (a), is the equivalent spectrum without the higher frequency harmonic components, as applicable for the linear approximation. Comparison of the spectra indicates that the higher frequency harmonic components of the non-linear HIFU have no discernible influence on the sub-fundamental peaks in the model bubble oscillations, which match the experimentally detected frequency content of the cloud acoustic emissions. As such, it is concluded that the observed frequency splitting in the model oscillation are due to the single bubble itself entering a regime of more pronounced non-linearity at higher driving pressure amplitudes.

The minimal influence of the harmonics is attributed to the relatively small associated amplitudes, and that the higher frequencies are further from resonance with the selected values of R_0 for the model single-bubbles.

Jetting from peripheral bubbles The increased non-linearity of the ensemble dynamics at higher PNP's is underscored by frequent observation of jet, and counter-jet formation (Lauterborn and Bolle [74]), from bubbles on the periphery of the clouds, figs. 4.7 and 4.8; a number of examples are arrowed white. Inwardly directed jetting from bubbles that formed at hydrophobic pits, etched in

a 2-dimensional array on a surface has been reported before (Bremond *et al.* [10]), albeit under comparatively controlled and idealised conditions. The observations of figs. 4.8 and 4.7 represent the sufficient temporal and spatial resolution to identify jets from bubbles at the periphery of a cloud, that are constituent to it, particularly at a typical HIFU driving frequency. Jetting activity is not observed at HIFU PNP's < 1.0 MPa.

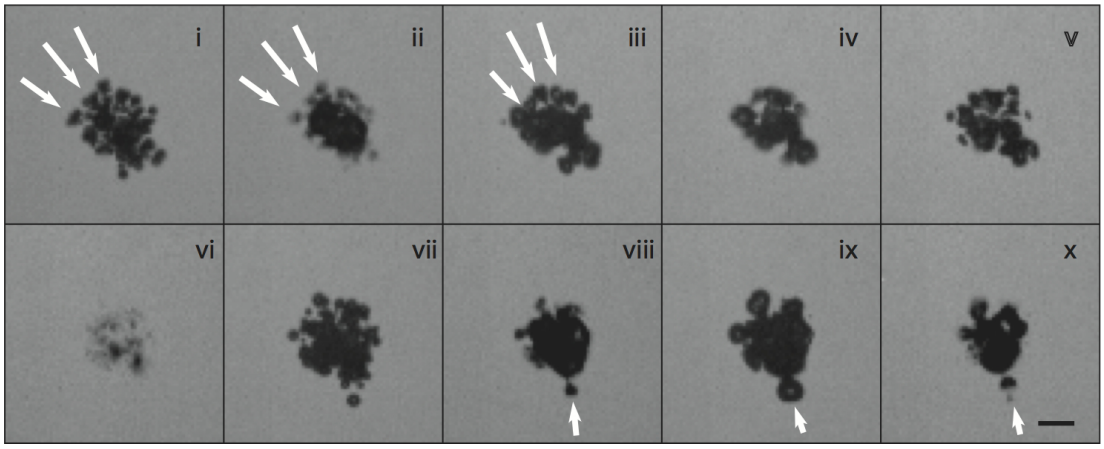

Figure 4.7: Jets in bubble clouds - sequential images extracted $\sim 80\ \mu s$ after the nucleation event, in HIFU of PNP = 1.29 MPa, rich in jetting activity from bubbles peripheral to the cloud (examples arrowed white). Scale bar bottom right: 50 μm.

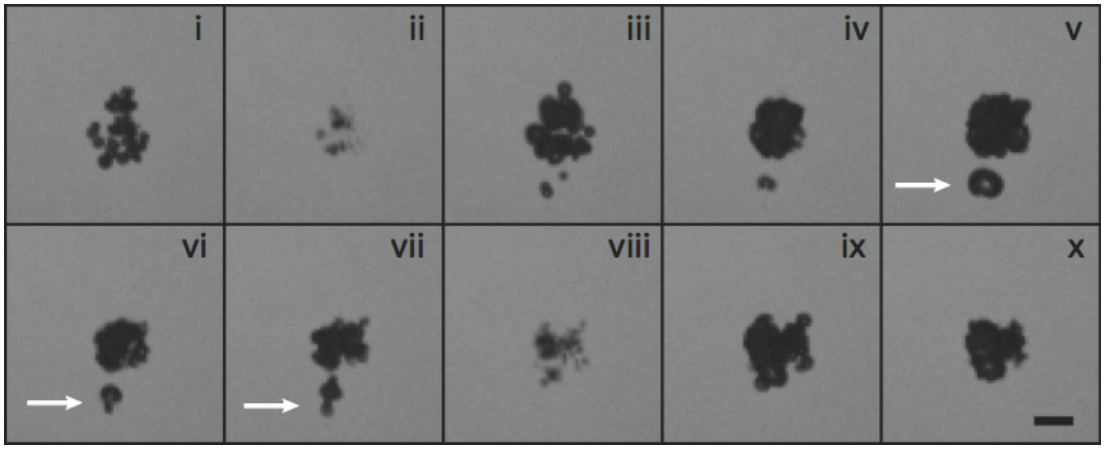

Figure 4.8: Jets in bubble clouds - a particullary prominent jetting event from an outlying bubble, below the cloud (arrowed white). Scale bar bottom right: 50 μm.

4.2.5 Discussion

Temporally resolved and directly correlated optical observations and acoustic recordings are presented, of single cavitation clouds developing at a very early stage of evolution in focused ultrasound, for the first time. The frequency of the physical bubble-ensemble oscillations translate directly to frequency content within the acoustic emissions, detectable via hydrophones custom-fabricated for sensitivity over the required bandwidth.

The analysis undertaken does not distinguish between the individual constituent bubble dynamics within the cloud, and the dynamics of the cloud itself. Inspection of fig. 4.1 (a) and (c) indicates that constituent bubbles oscillate as part of the ensemble and that the expansion and collapse phases are synonymous for both. The range of quiescent radii inferred from the RP model indicate that the frequency content within the acoustic emissions collected from the clouds, originate from a source of radius comparable to that of the cloud, rather than that of the constituent bubbles. Taking the speed of sound in water as 1500 m/s, implies a wavelength of $\lambda_0 \sim 2.7mm$, for the HIFU frequency used in this work. As $\lambda_0 \gg R_0$, the quiescent radius required for the RP model, it is concluded that this is a reasonable assumption for the purpose of analysing the acoustic emissions, in terms of scattered primary field.

The HIFU PNP amplitude threshold for cloud response transitioning from a stable regime exhibiting $f_0/2$, into one of more pronounced non-linearity with associated frequencies at $f_0/3$ and $2f_0/3$ is identified, in terms of the frequencies of the observed ensemble dynamics and in the acoustic emissions detected. The emitted frequencies may be fitted to existing models for bubble dynamics and information regarding the cloud size, relative to the driving frequency and pressure amplitude of insonation, extracted.

This work demonstrates that cavitation clouds can be characterised in terms of signature acoustic emissions, which could potentially be translated for monitoring of cavitation-mediated drug delivery from the vasculature, for focused ultrasound

therapy. Tissue represents a much more inhomogeneous and viscoelastic host medium than the one used for this work. However, cavitation activity in blood vessels, from microbubbles delivered intravenously for example, may undergo similar evolution on HIFU exposure.

4.3 Bubble-cloud translation

4.3.1 Overview

In the sample results of fig. 3.12 (see §3.8), the upwards (away from the HIFU transducer) translation of the LNAC clouds is clearly evident. As buoyancy is negligible over the timescales of observation, this translation is attributable to the acoustic radiation force of the propagating HIFU insonation (radiation force (see §2.2.4), as the unique sonoptic chamber configuration is specifically designed to avoid standing wave formation.

In this section, an analysis of the dependence of translation velocity (v_t) with intensity of exposure (PNP) is presented. In §4.2 above, the HIFU frequency-of-operation, f_0, was effectively determined by the high-speed imaging frame-rate available (1 Mfps). As such, 0.521 MHz was employed in order to satisfy the Nyquist sampling rate, for fully resolving cloud oscillations at $\sim$ 250 kHz ($f_0/2$). For the cloud translation observations presented here, resolution of cloud oscillations is not necessary, and therefore the HIFU frequency-of-operation value is not limited to that used for §4.2. As discussed in §3.3.1, there is the option of driving the same transducer at the 3^{rd} harmonic ($f_0 = 1.471$ MHz). This HIFU frequency permits a much larger range of intensities to be investigated, and is therefore used throughout the results presented in this section.

Using the Cordin camera at 3.0 MHz framing rates, equivalent cloud oscillations at this f_0 have been observed. However, imaging artefacts associated with this device prevent this data from being scientifically admissible at this time (ref: private correspondence with Dr Paul Campbell *et al.* PhD thesis Hans Rolfsnes

2012).

In §4.2 above, the value in approximating a cavitation cloud as a single bubble, for analysis of the acoustic emissions (scattered field), was demonstrated. Here, the approach is extended to provide a theoretical framework for the translation of a cloud in a given HIFU intensity. The favourable comparison between experimental observation and model analysis for each of the cloud dynamics, is taken as validation for the general technique.

Radiation force effects on bubbles have been investigated before. Palanchon *et al.* [100] concluded that there is a linear relationship between acoustic power and displacement after a given time, for single bubbles, and that the bubble diameter is crucial. If the bubbles are at resonance with the field, the displacement is maximal, fig. 2.11 (see §2.2.4). Utilising high-population density ultrasound contrast agent microbubbles, Kotopoulis *et al.* [68] determined that once microbubbles have aggregated under secondary radiation force effects, they can behave as a single entity. Accordingly, the contrast agent 'cluster' can be treated as a single bubble, in terms of the primary radiation force effects. The behaviour of such 'bubbly liquid' has been studied on many occasions, however, the observation of single bubble clouds, has only ever been partially achieved (Parlitz *et al.* [103]). The focus of previous experiments has been on investigating the physical parameters of the liquid/bubble mixture (Prospetti [106]).

The novelty of the work presented here, arises from the capability of nucleating single cavitation clouds, in well characterised HIFU fields of a controllable intensity. This allows a precise analysis of the translation speed of cavitation clouds over a wide range of HIFU PNPs.

Experimental parameters for the data presented, the laser-pulse was incident with an energy of 0.9 $\pm$ 0.1 mJ (adjusted slightly for each PNP, (see §3.8), to the focal region of the pre-established 1.471 MHz HIFU field. A total of 360 acoustic cycles were generated, with the laser-pulse incident after 70 μs, 15 μs ($\sim$

22 cycles) to allow for transducer 'ring-up' to the required pressure amplitude, and 55 μs for the ultrasound to reach the focus. High-speed camera operation at 500 kfps, is triggered to capture a few frames prior to nucleation of cavitation activity, such that cloud development is observed from inception through $\sim$ 285 cycles.

4.3.2 High-speed observation of translating clouds

Fig. 4.9 depicts sample high-speed observations of cavitation cloud translation, for HIFU PNPs from 1.1 to 8.9 MPa, with t = 0 μs defined as the moment of laser-incidence. Two features of cloud response are immediately apparent for increasing HIFU PNP: (i) an increased size and (ii) an increased rate of translation. The former conforms to the observations of cloud oscillation under lower frequency HIFU (f_0 = 0.521 MHz) of §4.2.2, whereby larger model quiescent radii were required to match the experimentally measured spectral features. As discussed there, the larger clouds at higher PNP's are attributable to increased levels of component bubble fragmentation following collapse, throughout the observation.

The more rapid translation is due to the higher acoustic radiation force. This effect is, however, somewhat reduced by the action of a drag-force on the cloud as it translates upward through the host medium (water), which will be more pronounced for larger clouds, moving more rapidly. The balance of these of these competing factors receives theoretical attention in §4.3.3 below.

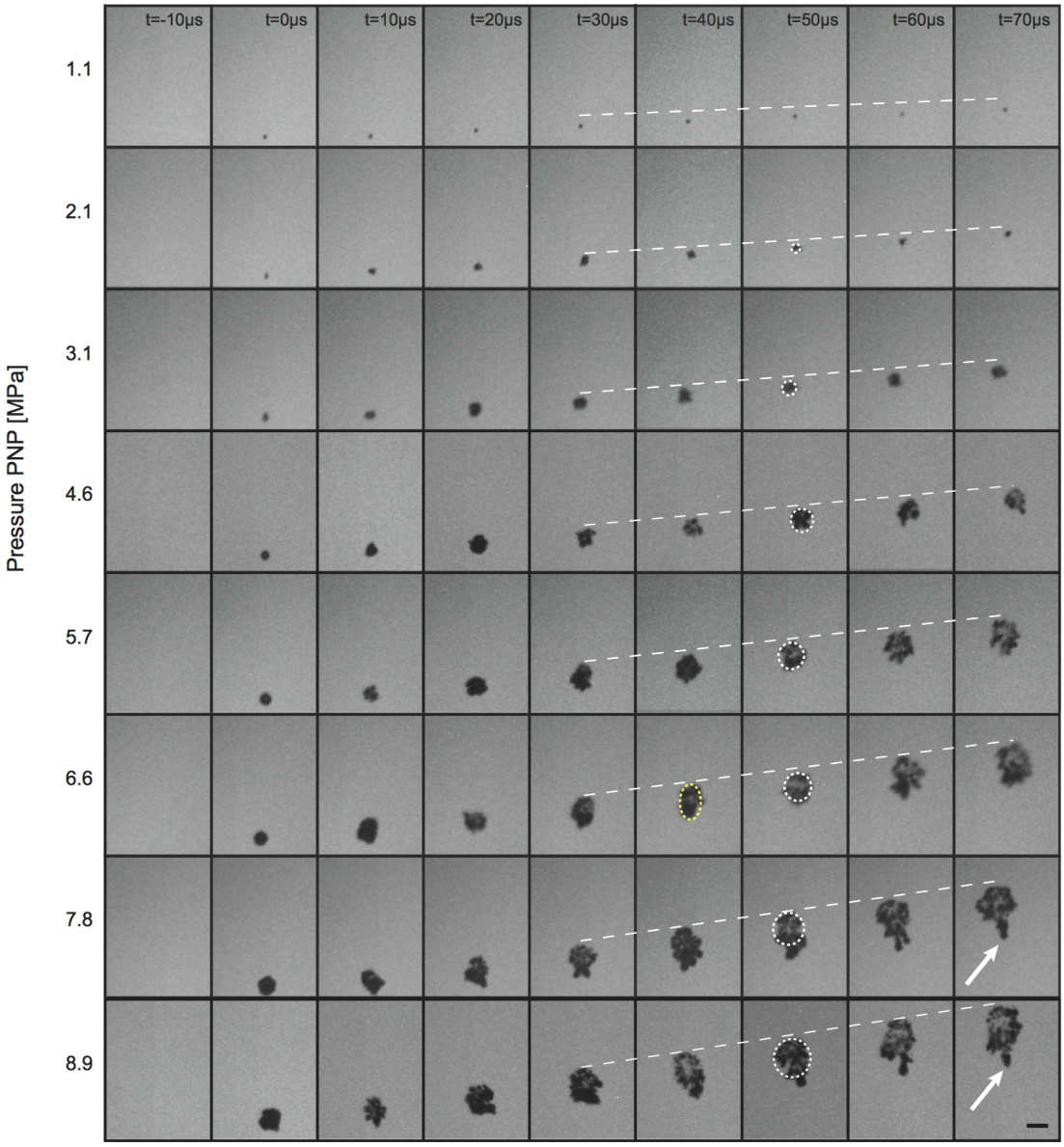

Figure 4.9: Translating cavitation clouds - High-speed observation of cavitation cloud translation in HIFU of varying intensity. Laser nucleation at $t = 0$ μs. Peak negative pressure (PNP) from 1.1 to 8.9 MPa. Scale bar: 50 μm.

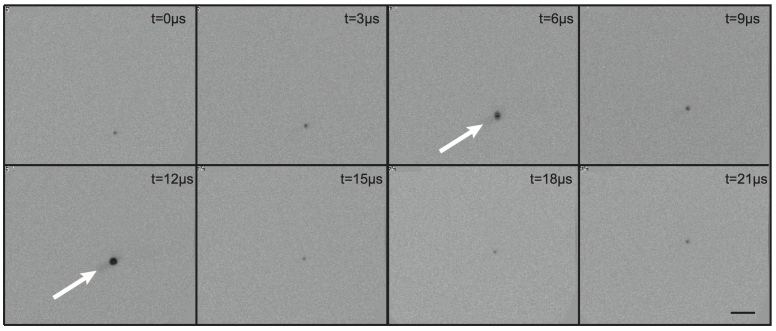

Figure 4.10: Minimum cavitation level - High-speed observations of the minimum level of cavitation activity, recorded through the strongest objective lens available, in a HIFU field of PNP = 0.6 MPa. Inflated phase marked by white arrow. Scale bar: 20 μm

A further observation of fig 4.9, is the morphology of the translating cavitation cloud, under incrementally increasing HIFU PNP. At relatively low driving amplitudes (up to 4.6 MPa), a small number of constituent bubbles retain a quasi-spherical geometry throughout the observed translation. Again, this conforms to the observations of cloud oscillations in §4.2, in comparable intensity HIFU exposures, which allowed the clouds to be approximated to single (spherical) bubbles via the Rayleigh-Plesset model. For intermediate PNPs (5.7 and 6.6 MPa), the sphericity is broken some $20-30$ μs after nucleation, as the cloud adopts an elliptical morphology, elongating along the HIFU propagation axis. This is perhaps a somewhat surprising observation, as one might expect the component bubbles of the cloud proximal to the HIFU transducer to 'shield' the bubbles distal to the transducer, from radiation force effects. At the highest PNP amplitudes used (7.8 and 8.9 MPa) the clouds adopt a distinctive 'mushroom' shape, following the elliptical phase, from ~ 60 μs. This morphology resembles those previously reported by Chen *et al.* [21]. They used a single element 1.2 MHz transducer generating 196 acoustic watts, and observed cavitation activity at 100 kfps with an exposure time of 10 μs. The field of view of was 2.3×1.5 cm and a total of 7 images were acquired per sequence recorded. This 'snap-shot' approach is incapable of resolving the cloud evolution dynamic that produces such complex cloud morphologies, such as those of fig. 4.9.

The cloud shape observations are likely attributable to intra-cloud bubble-bubble interactions, host medium viscosity, and possible non-linear effects, as well as the action of the acoustic radiation force from the primary HIFU field. The analysis below is restricted to the observed rate of translation, and assumes a single spherical bubble of dimensions matching those observed for the clouds.

The range of HIFU PNPs used for the observations described above, correspond to those at which cavitation clouds could be reliably nucleated and observed. Fig. 4.10 are frames extracted from a high-speed sequence recording LNAC at HIFU PNP = 0.6 MPa, and is representative of the lowest recorded level of activity. LNAC at this PNP was only observed with the 50× objective lens (note the different spatial scales of figs. 4.9 and 4.10), in the parallel viewing configuration, (see §3.6). In this arrangement, it is imperative that the laser-pulse nucleates the cavitation event in the same plane as that observed in the image relayed to the high-speed camera used. From the orthogonal observations, it is clear that cavitation does not always nucleate in the same position (± 10s of μm) along the laser axis. This combination of factors meant that although LNAC may be reliably achieved at this intensity, it was not always observed. The spatial resolution of the 10× objective lens, in the orthogonal configuration, was insufficient to image this level of activity. Nonetheless, a number of such observations were obtained, that are included in the following analysis, for completeness, and as a key feature for the model to encompass.

In events similar to fig. 4.10, a single bubble (or very small number of constituent bubbles) forms, that translate very rapidly, despite the low intensity (and therefore low radiation force) associated with the primary field. Significantly, the bubble/small bubble cloud has a different radius at different stages of the translation, with inflated phases captured at t = 6 and 12 μs. At a frequency-of-operation, f_0 = 1.471 MHz, and a framing rate of 1 Mfps, this dynamic is clearly not fully resolved. However, the unexpectedly rapid translation, combined with the observation of a time-variant radius, suggests that the bubble(s) may be

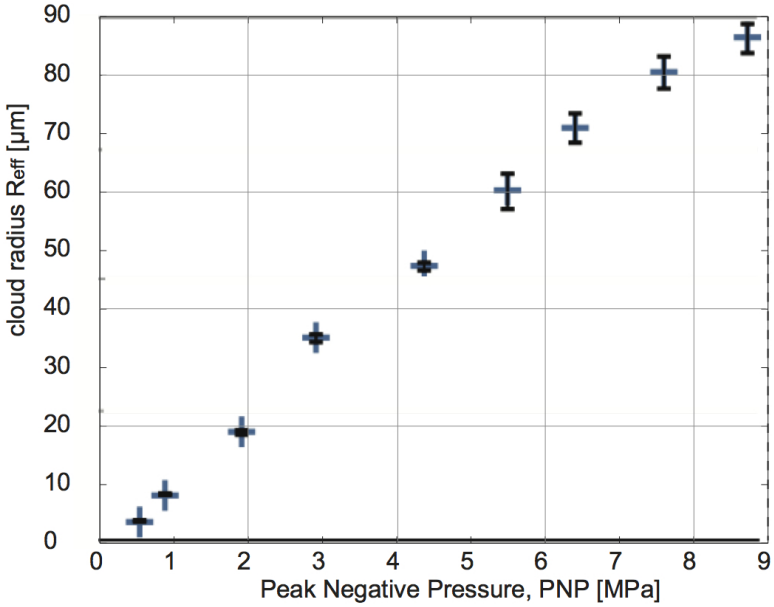

Figure 4.11: PNP vs. effective cloud radius - Experimental data of average radius at different increasing intensity levels . The error bars depict the standard deviation over n = 15 (n=6 for 0.6 MPa) observations.

undergoing linear oscillations in response to the primary field. As described in §2.2.4, there is a resonance condition whereby an oscillating bubble will couple to the primary field, to greatly accentuate radiation force effects (Leighton [80]).

As for §4.2 previously, the cavitation clouds represented by fig. 4.9 are approximated to single spherical bubbles, subject to equivalent HIFU exposure. In terms of the cross-section 'presented' to primary field, the clouds at higher PNPs are well approximated by a 'hemispherical head', as depicted with white dotted circles, fig. 4.5. The 'effective cloud radius' R_{eff}, for a given HIFU intensity, was therefore estimated as an average between measurements taken at $t = 30\ \mu s$ and 90 μs. The results are summarised by fig. 4.11, which empirically suggests a linear relationship between the HIFU PNP and R_{eff} effective average cloud radius. As discussed previously, clouds at the highest HIFU PNP's evolve to an unspherical morphology in the latter stages of the insonation. To include experimental data for comparison to the model at these intensities, a value of R_{eff} is estimated from the leading hemi-spherical head of the cloud, in the direction of translation.

The translational velocity ($\bar{v_t}$) for each cloud was measured in the same time

interval (t=30 μs to 90 μs). The velocity is approximately uniform for this time interval, confirmed by the dashed-lines drawn on fig. 4.9. This assertion is further supported via inspection of fig. 3.5 (a)) (see §3.3.2), where it can be seen that there is no significant pressure gradient in the region of the field that the clouds occupy over this time interval, ($\nabla P \sim 0$). A constant radiation force, according to eq. 2.16, F_r (§2.2.4), can therefore be assumed.

4.3.3 Analysis

The translation velocity v_t, of a bubble in a steady fluid subjected to an ultrasound field can be calculated using (Dayton *et al.* [30]):

$$F_r + F_d - \frac{d(mv_t)}{dt} = 0 \tag{4.4}$$

where F_r is the primary radiation force, F_d the drag force, and m the displaced mass of the bubble, calculated as $m = \frac{2}{3}\pi\rho R_0^3$, where R_0 is equilibrium radius and ρ is the density of the surrounding fluid. F_r as eq. 2.16 in §2.2.4 cannot be sim ply applied to this case, but needs adapted to account for the moving boundary (Yoisioka and Kawasima [140]) and the elasticity of the bubble (Hasegawa and Yosioka [55]). Averaging over one acoustic cycle, the primary radiation force F_r, is given by (Dayton *et al.* [30]):

$$F_r = \frac{(PNP)^2 R_0}{\rho c f_0} \frac{\delta(\frac{f_r}{f_0})}{[(\frac{f_r}{f_0})^2 - 1]^2 + [\delta(\frac{f_r}{f_0})]^2} \tag{4.5}$$

where c is the speed of sound, PNP is the peak negative pressure, δ is a dimensionless total damping coefficient, f_0 is the driving frequency, and f_r is the bubble resonance frequency. This is related to R_0 via the Minneart equation, (see §2.2.2).

It can be seen from eq. 2.5, that as seen in fig. 2.11 (§2.2.4), the radiation force on a bubble of a certain size, is strongly dependent on the frequency of the acoustic field, according to a resonance condition.

The drag force is given by (Dayton *et al.* [30]):

$$F_d = -\frac{\pi\eta}{4} C_d Re R_0 v_t(t) \tag{4.6}$$

where η is the shear (dynamic) viscosity of the fluid, Re the Reynolds number and C_d the drag coefficient. Combining eqs. 4.4, 4.5 and 4.6, and integrating over time, results in an expression for the translation speed of a single bubble, in a given ultrasound field, as:

$$v_t = \frac{4(PNP)^2}{\rho c f_0 \eta C_d Re} \frac{\delta(\frac{f_r}{f_0})}{[(\frac{f_r}{f_0})^2 - 1]^2 + [\delta(\frac{f_r}{f_0})]^2} [1 - e^{-(\frac{3\eta C_d Re}{8\rho R_0^2} t)}]. \tag{4.7}$$

Eq. 4.7 can be simplified according to the current experimental parameters as $R_0 \ll 1$, $e^{-(\frac{3\eta C_d RE}{8\rho R_0^2} t)} \to 0$, and $C_d Re \sim 24$ (Kotopoulis and Postema [68]). Further adapting eq. 4.7 for the bubble clouds the dependence of effective cloud radius, R_{eff}, on HIFU PNP, must take into account. The radius of the bubble, or in this case the effective cloud radius, R_{eff}, is not explicitly used in eq. 4.7, but the corresponding effective cloud resonance frequency, f_{eff}, is a key term. The effective cloud resonance frequency is inferred from from $f_{eff} = 3/R_{eff}$ eq. 2.10 (see §2.2.2), and is a function of PNP, $f_{eff}(PNP)$, as discussed. From eq. 4.7, the translational velocity for the cloud is given as

$$v_t \sim \frac{(PNP)^2}{6\rho c f_0 \eta} \frac{\delta(\frac{f_{eff}(PNP)}{f_0})}{[(\frac{f_{eff}(PNP)}{f_0})^2 - 1]^2}. \tag{4.8}$$

From the observations of §4.2 oscillation results section, it may be assumed that component bubbles, which are of resonant size, are oscillating within the cloud as it translates. However, the physical interaction between the bubbles acts to preserve the integrity of the cloud, such that it responds to the acoustic radiation force of the primary field as a single bubble, of significantly larger radius. Accordingly, application of this model to the cloud observation data of figs. 4.9 and 4.10 is conducted via the dependence of cloud size on HIFU PNP of fig. 4.11,

and the single bubble approximation for the cloud.

Fig. 4.12 summarises results from the model, with experimentally observed cloud $\bar{v_t}$ data, overlaid for comparison. Each of the coloured lines represents how sample model v_t depends on PNP, for single bubbles of differing size (according to the R_{eff} value at top of each line), in an acoustic field of $f_0 = 1.471$ MHz, corresponding to that used experimentally. The v_t's for larger R_{eff}'s increase less rapidly with PNP because these bubbles are further from the resonant size. The red (tick-shaped) line therefore represents the model predictions of v_t for single model bubbles of R_0 matching R_{eff}, for the clouds that develop in a given PNP, *at that PNP*. The data points (blue +'s) represent cloud $\bar{v_t}$'s experimentally measured with high-speed photography, at known HIFU intensity.

4.3.4 Discussion

This chapter provides an analysis of perhaps the most obvious feature of LNAC cloud activity in a propagating HIFU field; that of translation in response to the primary radiation force. The experimental data of figs. 4.9, 4.10 and 4.12 indicates that the translational velocity is in the range of 1-10 m/s for the clouds investigated here. Higher PNPs result in more rapid translation as may be expected, although the formation of larger clouds also results in a more pronounced drag effect, that must also be taken into account. A key observation of unexpectedly rapid translation for the very small clouds that evolve in lowest HIFU PNP investigated (0.6 MPa), is accounted for through identification of a resonance condition for these clouds, with the primary field. The perceived volumetric pulsations of fig 4.6, suggest that the rapid translation is due to a coupling between pronounced oscillations and the pressure fluctuations of the primary field. §4.2, and observations taken with the Cordin 550-62 camera, indicate that although cloud oscillations are not resolved in the data of fig. 4.9, they are undoubtedly occurring, at off-resonance to the primary field, and therefore the translation ve-

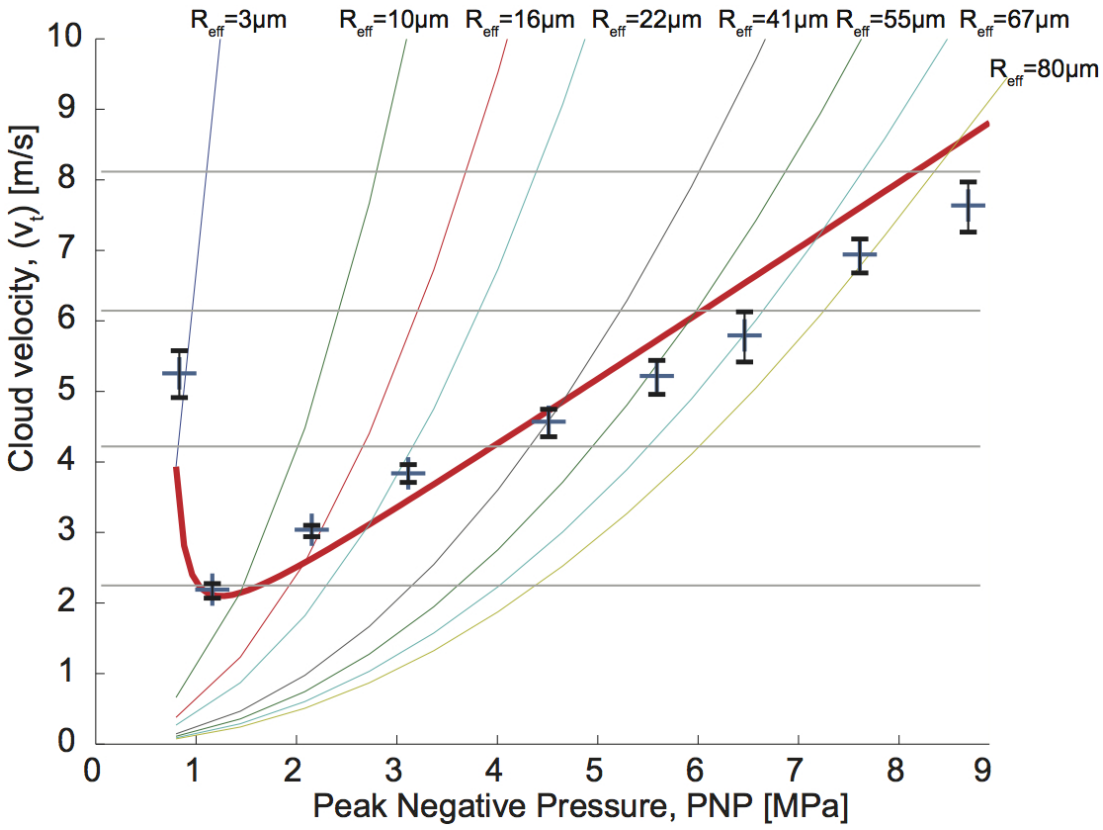

Figure 4.12: PNP vs. translation velocity, v_t (model) and $\bar{v}_t$ (experimental) - Experimental data of measured translation speed (blue crosses). The error bars depict the standard deviation (n=15 for each PNP except 0.6 MPa, for which n=6). The coloured lines represent the model predictions for v_t with increasing PNP for single bubbles of $R_0 = R_{eff}$, the effective cloud radius at a given PNP, according to fig. 4.11. The red tick-shaped line therefore represents the model predictions for comparison to the experimental data.

locity actually reduces for increasing PNP, before increasing again for the higher PNPs investigated. This effect gives rise to the characteristic tick-shape of the model prediction for cloud translation, of fig. 4.12.

The significance of these observations to FUS procedures is likely restricted to cavitation activity occurring in the vasculature. As discussed in §4.2, tissue has a much higher viscosity than water, the host medium used here. As such, the drag force of eq. 4.6 will dominate the radiation force, and physical translation of a cloud will not occur. Nonetheless, a radiation force will be exerted, which could act to displace tissue in the manner discussed for ARFI imaging (see §2.5). At higher HIFU intensities, this displacement could conceivably result in tissue fracture effects, which could have significant implications for FUS procedures. Further investigation of this would require the LNAC technique be adapted for cavitation studies in a host medium of representative viscosity, such as a tissue-mimicking gel or phantom (discussed in Chapter 5).

In the vasculature, cavitation activity is known to cause membrane permeabilisation effects, under investigation for drug-delivery applications (see §2.2.5). Ultrasound contrast agent microbubbles are often used to provide cavitation nuclei to mediate this effect, via bolus injection. Preliminary work undertaken with microbubbles in a capillary tube model (see Appendix §6.2), placed inside the sonoptic chamber, suggests cavitation clouds develop with marked similarities to those observed via the laser-nucleation technique, for similar HIFU PNP's. As such, the observations of cloud translation here, are highly significant for assessing potential vasculature wall permeabilisation and/or damage, in terms of how rapidly cavitation will move through a blood vessel, and the ensuing interaction with the endothelia. Particularly the resonance effect identified could be key for HIFU frequency selection for microbubbles of specific and defined radii.

4.4 Controlled jetting from LIC's exposed to HIFU

4.4.1 Introduction to cavitation jetting

The remarkable formation of a liquid jet from a collapsing cavity, fig 4.13, is a highly energetic and dynamic event. *Jetting* is implicated as a mechanism underpinning a wide range of processes, many deleterious such as erosion of surfaces in hydrodynamic systems, and some potentially beneficial such as kidney stone destruction, during lithotripsy.

A jet forms from a collapsing cavity when the liquid at one region of the wall is accelerated preferentially, generating an involution that evolves through the body of the cavity. On impacting and penetrating the far-side of the cavity, the rapidly moving liquid of the involution becomes a jet, consisting primarily of host medium liquid, with an envelope of bubble material known as the vapour jet (Blake *et al.* [9]) (shaded areas fig. 4.14). In energy terms, the potential energy of the expanded bubble is converted to kinetic energy of the jet, via this process. Jet velocities in the region of 100's m/s have been recorded (Leighton [80]), via high-speed photographic approaches. The 'water-hammer pressure', associated with the impact of a jet-tip on a surface, has been estimated to be in the GPa regime, and is known to pit surfaces such as aluminium (Philipp and Lauterborn [104]). The extent of the contribution of jet-formation to cavitation erosion of, for example, ship propellers remains the subject of some debate.

Jet-formation from collapsing cavities has been observed to occur in three distinct scenarios, fig. 4.14: (i) when a shock-wave is incident to it (Field and Walton [42]), (ii) in the presence of boundary (Lauterborn and Bolle [74]) and (iii) in the presence of other bubbles (Tomita *et al.* [119]).

The feature common to each of these scenarios is the existence of a pressure gradient across the bubble, which is responsible for the preferential acceleration

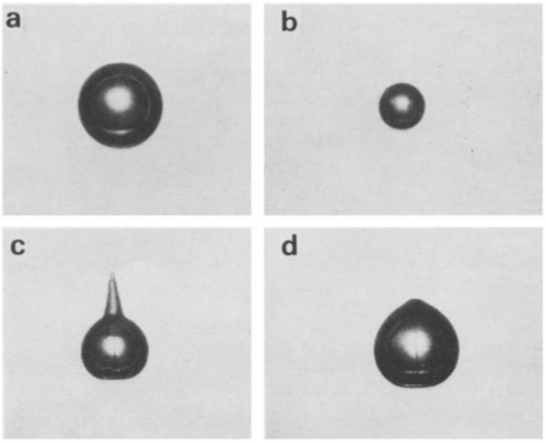

Figure 4.13: The first recorded example of jet-formation from a cavity - Spherical bubble collapsing (a, b) and rebounding (c, d) far from boundaries. The framing rate is 500 frames per second. From Benjamin and Ellis [5]

at one region of the cavity-wall. In the former case, a shock-wave consisting of a leading positive pressure phase, will act to collapse the cavity asymmetrically from the region of the cavity-wall that it first encounters, fig. 4.14 (i), thus generating a jet in the direction of shock propagation. This may also be considered as the action of radiation pressure on the cavity, due the pressure gradient in the shock, leading to a conservation of impulse which causes the cavity to translate and jet in the direction of motion.

In the latter cases, the existence of a constraining influence on the liquid between the object bubble, and a surface or second bubble, acts to retard the inward flow of liquid at the proximal point on the cavity-wall, during the collapse phase. The unconstrained liquid at the cavity-wall opposite, flows freely during the collapse, thus forming the involution in a direction toward the constraining object (the surface or second bubble). In this manner, the resulting jet is directed toward the constraining object, and may ultimately impact upon it. The microfluidic flow local to the jetting bubble in both these scenarios is equivalent, fig. 4.14 (ii) and (iii). Accordingly, a (solid) boundary placed halfway between a bubble binary system, induces a similar jetting dynamic in the object bubble, which can be analysed through a 'Method-of-Images' technique, such as that often used for electrostatics. It is notable that for all cases, there is also translation

of the bubble centre in the direction of the jet that forms, throughout the jetting process.

For biomedical applications, jetting from contrast agent microbubbles has been the subject of investigation, as a possible mechanism for damage to vasculature (during contrast-enhanced diagnostic imaging), and potential therapeutic drug delivery to cells (sonoporation, see §2.2.5). For the latter case, the underlying principle is that a microbubble jetting in response to ultrasound exposure, might provide a self-actuating 'syringe' for the delivery of drug particles into a cell, or across a membrane, such as the blood-brain-barrier (see §2.1.6), to a site of pathology. In the presence of a compliant boundary however, a reversal of the jetting direction, away from the surface is known to occur (Blake *et al.* [9], Philipp and Lauterborn [104]). This is due to the effect of the surface deformation in response to the bubble oscillation. Chen *et al.* [20] observed that reverse-jetting occurs for microbubbles in *ex-vivo* blood vessels, perfused with a contrast agent and exposed to HIFU. The associated flow of the liquid away from the vasculature wall was observed to cause strong deformation (invagination). Sankin *et al.* [110] used tandem laser-induced cavity interactions to delivery fluorescent molecules cultured cells *in-vitro*.

The results presented in the following sections detail the interaction between LIC's and a burst of HIFU. A new mechanism for cavity-jetting is identified, mediated by the action of acoustic radiation force, on the cavity throughout the collapse phase. The key effect of the position of the LIC, relative to the HIFU focus, on the characteristics of the resulting jets is investigated. Preliminary results on jet manipulation from cavities in proximity to a surface are presented, along with a discussion of possible significance to biomedical applications.

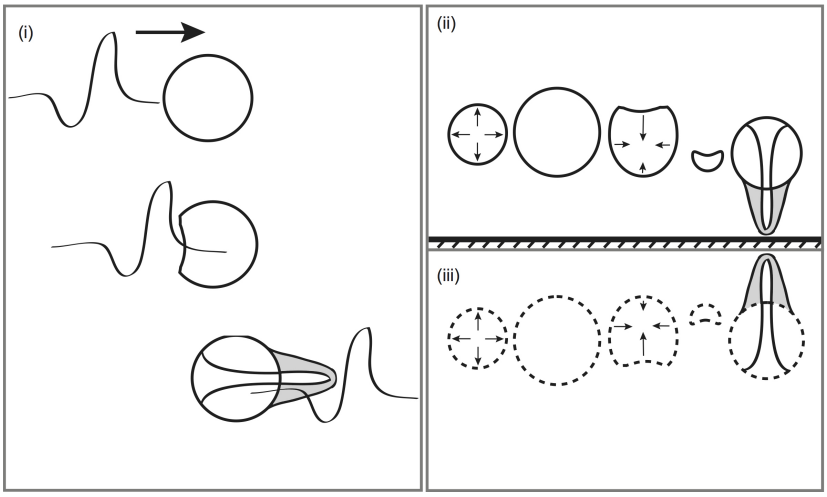

Figure 4.14: Jetting mechanisms - the imposition of pressure gradient across a collapsing bubble will cause it to jet. Three configurations are know to result in this dynamic: (i) a shock-wave incident to the cavity collapses the wall it first encounters. The bubble will collapse towards the lower pressure region. (ii) a bubble expands and collapses close to a boundary. The surface restricts the flow of the intermediate fluid, creating a low pressure region between it and the boundary. (iii) a second bubble with equivalent dynamics can substitute the function of the boundary. Mutual jetting directed toward to the second bubble in the binary pair, results.

4.4.2 Experimental parameters

For all results presented in this section, a laser-pulse energy measured at the back aperture of the focusing objective lens, of 5.0 ± 0.5 mJ was used. The error associated with this value is due to instrumental (pulsed-laser) fluctuations, according to the manufacturers guidelines and consistent with *in-house* power-meter measurements A direct consequence of the energy fluctuations is a distribution for the size of the LICs generated, at maximal expansion, of $R_{max} = 385 \pm 20\ \mu m$. Nonetheless, single spherical cavities were reliably produced. The most noticeable repercussion for the results presented, is a variation in the collapse time of LIC's of $\tau_c = 36 \pm 3\ \mu s$, via eq. 2.8 (see §2.2.1), with larger cavities taking longer to collapse. The transducer is driven with a single burst of 1000 cycles at f_0=1.471 MHz, to access a wide range of HIFU intensities (and therefore radiation forces) (see §3). Preliminary experiments indicated that the optimal jetting results were obtained when the HIFU was incident to the LIC *during the collapse* phase only, in contrast to the sample results of §3.8, where a pre-established HIFU field is

propagating throughout the expansion and collapse. As such, the HIFU burst is electronically triggered to reach the focus $\sim$ 44 μs after laser-incidence to the water in the cavitation chamber. The laser-pulse was focused via the 50$\times$ long working distance objective lens (Mitutoyo, 0.42NA), mounted on a micro-translation stage. This provided the capability for generating LICs at various positions relative to the HIFU focus, by manual scanning of the laser-focusing lens. The high-speed observations presented were imaged through a second 10$\times$ lens (Mitutoyo 0.28 NA) orientated orthogonally to the laser propagation axis, fig. 3.8 (see §3.6), with the Shimadzu camera operating at 0.5 Mfps.

4.4.3 Jetting from LICs exposed to HIFU of variable intensity

Fig. 4.15 is representative high-speed data illustrating LIC behaviour in response to bursts of HIFU at varying intensity. The peak negative pressure at the focus (see §3.3.2) increases from PNP = 0 MPa, row (a), to PNP = 11 $\pm$ 1.0 MPa, row (j). Images are selected from each sequence to represent the LIC dynamic at key stages, within the constraints of the temporal distribution described previously. Relative timings (at the top of each column) are therefore denoted with the '$\sim$' symbol.

Fig. 4.15 row (a) depicts an LIC with no HIFU (PNP = 0 MPa) incident, representing a control experiment. As described previously, §2.2.1, a plasma forms on laser-incidence, from which a classic vapour bubble (LIC) expands to a maximum radius of $R_{max} = 380$ μs at $t_{max} \sim 44$ μs, fig. 4.15 (a) (ii). A collapse phase of $\sim$ 36 μs follows, under the inertia of the host medium, with energy being dissipated from the system primarily via the emission of shock waves and acoustic transients (see §3.8.1), and heating effects incurred during the collapses.

For all other data represented, fig 4.15 row (b)-(j), a HIFU burst reaches the LIC around the instant of maximum inflation (R_{max}), column (ii). At higher intensities, PNP $>$ 2.1 MPa, the arrival of the HIFU burst is particularly evident

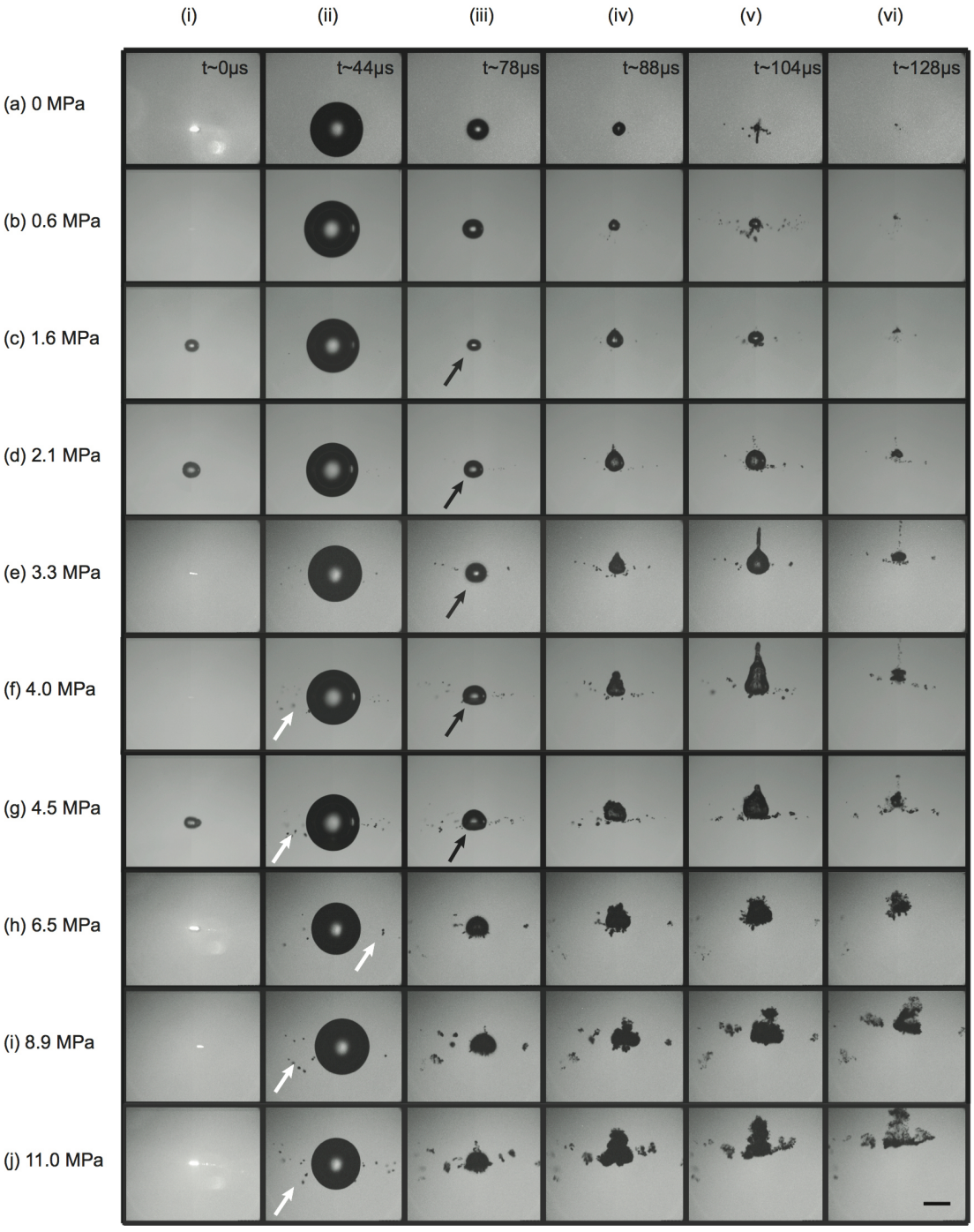

Figure 4.15: LICs exposed to different PNPs - high-speed data,recorded at 500 kfps, illustrating LIC behaviour in response to HIFU, PNP amplitude according to the values listed to the left. Scale bar: 350 μm

from the nucleation of secondary LNAC clouds, from locations along the optical path of the laser-pulse, around the main bubble (arrowed white, column (ii)). This was the first indication that the cavitation nuclei formed by the laser-incidence were indeed stable, and could be activated by a delayed HIFU insonation (see §5), in contrast to the pre-established fields of §4.2 and §4.3. These clouds do not have a significant influence on the dynamics of the primary LIC bubble itself (see §3.8), but are a good indicator for the presence of a strong ultrasound field in the region. For HIFU of PNP = 0.6 MPa, row (b), the HIFU has no tangible influence on the LIC dynamics, other than a slight upward translation of the centre of mass of the bubble, equivalent to the cloud translation observations of §4.3. For HIFU of PNP = 1.6 and 2.1 MPa, row (c) and (d), the first signs of jetting can be observed, at $t \sim 88\ \mu s$ column (iv), as protrusions evolving from the uppermost surface of the LICs. Inspection of the frames at $t \sim 78\ \mu s$ (iii) reveals the effect of the radiation force acting on the bubble wall during the collapse. As expected for jet-formation generally (Ellis [38]), 'flattening' of a region of the cavity wall is observed during the collapse (arrowed black, figs. 4.15 and 4.16), at the wall opposite to that from which the jet later emerges. In this case, the bubble is compressed by the additional force $< \vec{F_r} >$ eq. 2.16 (see §2.2.4) acting only on the side of the bubble proximal to the transducer. This interaction over the duration of the collapse satisfies the asymmetry requirement for a jet to form (Gerold *et al.* [49]).

To verify that the pressure gradients of the individual phases of the ultrasound burst do not in themselves result in jet formation, short tests bursts of 5 cycles were generated, which had no discernible influence on the primary LIC (and did not result in jetting activity). As such, the jetting observations of fig. 4.15 can be attributed to the accumulated action of the radiation force on the LIC over the collapse time, equivalent to ~ 50 acoustic cycles. The bubble dynamics are also unaffected by the shock waves and transients reflected from the HIFU transducer, initiated at laser-incidence and bubble collapse (see secondary excitation effects,

§3.8 and fig 4.15, (a) (v)).

For the observations presented, the jets become apparent during the first rebound phase, following the initial collapse. For HIFU of PNP = 3.2 and 4.0 MPa, row (e) and (f), particularly prominent jets form, with 'jet stagnation' occurring at $t \sim 104\ \mu s$, column (v). In fig. 4.15 (f) (v), a filamentous structure is apparent through the centre of the rebounded bubble, which is the jet-structure internal to the cavity. The inverted funnel-shaped protrusion at the top of the cavity is the vapour-jet, previously identified by Blake [9], which is comprised of intra-cavity vapour displaced as the jet pierces the top wall. Following stagnation, the long cylinder of gas and vapour becomes unstable and breaks up into debris, along the length of the jet. The centre of the bubbles also translates upwards during the collapse and rebound phase, in the direction of jet-formation, with the rate of displacement dependent on the HIFU intensity.

Further increasing the HIFU pressure amplitude acts to destabilise the bubble during the collapse phase. This is first evident as a 'rippling' effect on the bubble surface, which instigates a pre-collapse disintegration into bubble-debris, of component size comparable to that which is resonant with the HIFU field §4.2 and §4.3. Nonetheless, jet-like activity, superimposed onto the debris, remains apparent for PNPs > 6.5 MPa. This can be taken to infer that involution of the cavity wall occurs from the primary LIC, under the action of the radiation force, prior to and during disintegration. HIFU of on-axis PNP = 3.3 MPa was found to yield the most pronounced jetting.

4.4.4 Directed jetting from LICs at varying transverse locations

For all the jetting observations of the previous section, the LICs were generated in the centre of the HIFU focus, on the axis of propagation. To investigate the effect of the relative positioning of the LIC to the acoustic focus, the laser-focusing objective lens was manually adjusted along the laser propagating axis, via a micro-translation stage. In the orthogonal viewing configuration, fig. 3.8 (see §3.6), this results in LIC's forming at various lateral positions, relative to the HIFU field focus, in the imaging plane of the 10× objective lens. In this way, the interaction between off-axis HIFU and LICs can be studied.

Fig. 4.16 are selected images from high speed sequences, recorded at 0.5 Mfps, of LIC's initiated at five lateral positions, denoted L2 , L1, M, R1, R2, including control C; LIC with no ultrasound generated. As before, laser-nucleated acoustic cavitation (LNAC) clouds (arrowed white, fig. 4.16) are observed around the primary LIC, indicating HIFU has propagated to the focal region. Again, this activity has little bearing on the jetting behaviour itself, but the clouds do serve to provide incidental information on the ultrasound radiation forces in action, around the locale. Comparing the direction of translation of the clouds with fig. 3.5 (see §3.3.2), (also provided as background in column (iii)) indicate that they follow the pressure gradients away from the point of highest intensity, irrespective of the flow induced by the primary LIC dynamic. For example, the collapse of the primary LIC of fig. 4.16 row (a), should act to translate the cloud to the left. The actual translation, to the right of the image, is due to the radiation forces imposed by the intervening HIFU focus.

The principal features in fig. 4.16 are the jetting directions and jet-lengths at $t \sim 88\ \mu s$, column (vii). These are clearly a function of the lateral location of the LIC, with respect to the HIFU focus. Columns (iii) and (iv) illustrate the relative positioning, schematically as per model analysis of §4.4.5.

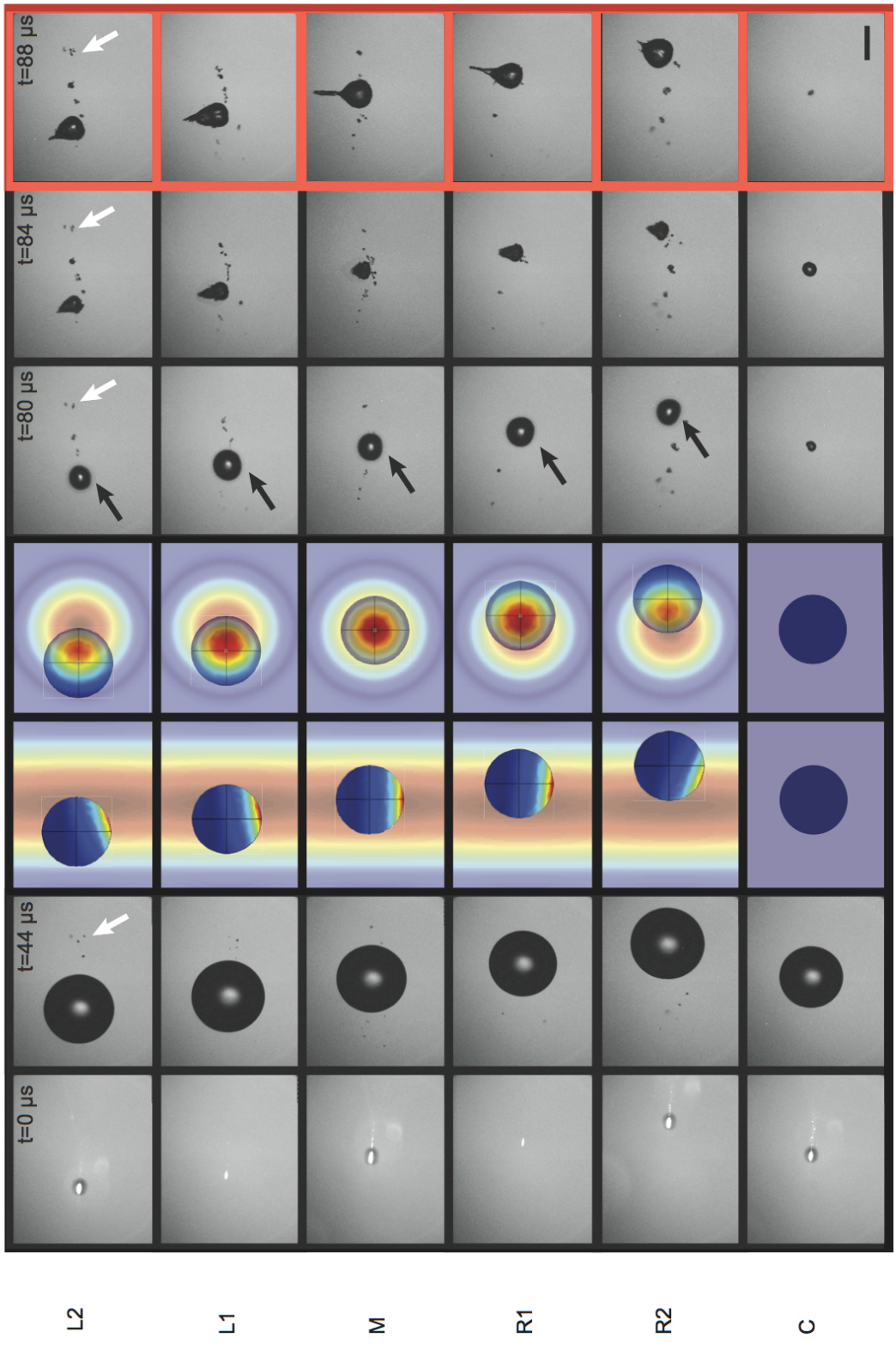

Figure 4.16: LICs exposed to HIFU at varying transverse locations - caption on following page.

LICs exposed to HIFU at varying transverse locations - (ii) LICs at maximum inflation at various transverse locations across the focus. Modelled radiation pressure exerted by the HIFU burst across the cavity surface, (iii) as per camera view (higher forces represented darker red), (iv) showing the view from below, superimposed over the simulated ultrasound focus, (without the presence of a cavity, and highest intensity represented darker red) (v-vii) Images of the subsequent collapse extracted from high-speed sequences recorded at 0.5 Mfps, demonstrating the dependence of jet-formation on the location of the LIC, relative to the ultrasound focus. Scale bar: 400 μm.

Column (iii) depicts the equivalent viewing perspective of the high-speed camera, with the HIFU field map in the background obtained by simulation (see Appendix 6.3), and in agreement with *in-situ* hydrophone scans, figs. 3.5 (see §3.3.2). Note that the simulations are undertaken in the absence of LIC's, which would be expected to add significant scattered components. Column (iv) shows the relative location of the LIC bubble to the HIFU focus, as viewed from below (see also fig. 3.3 in §3.3.2). For all pressure amplitudes used, the most prominent jets are actuated from cavities collapsing on the ultrasound axis, in a direction parallel to that of ultrasound propagation (see fig. 4.15). LICs generated to either side of the axis result in progressively shorter jets forming, at larger angles to the ultrasound axis. The flattening of a region of the cavity is observed during the collapse (arrowed black, figs. 4.15 (iii) and 4.16 (v)), at the wall opposite to that from which the jet later emerges. The variation in the position at which flattening occurs is attributable to the action of radiation pressure at the different positions, due to the accumulated radiation force imposed on the cavity, within the HIFU focus. Fig. 4.17 summarises all experimental observations undertaken (n>10 for each position L3-R3), detailing jetting angle to field axis, and jet-length at tip stagnation. Standard deviations in angle (dashed lines) and length (small arrow-heads) are depicted. The coloured background is the normalised simulated ultrasound pressure field (scale right) at the focus, via a projection technique, based on transducer geometry, with *in-situ* measured PNP contours superimposed (in MPa).

Also depicted (x) are the positions of the plasma flash on absorption of the

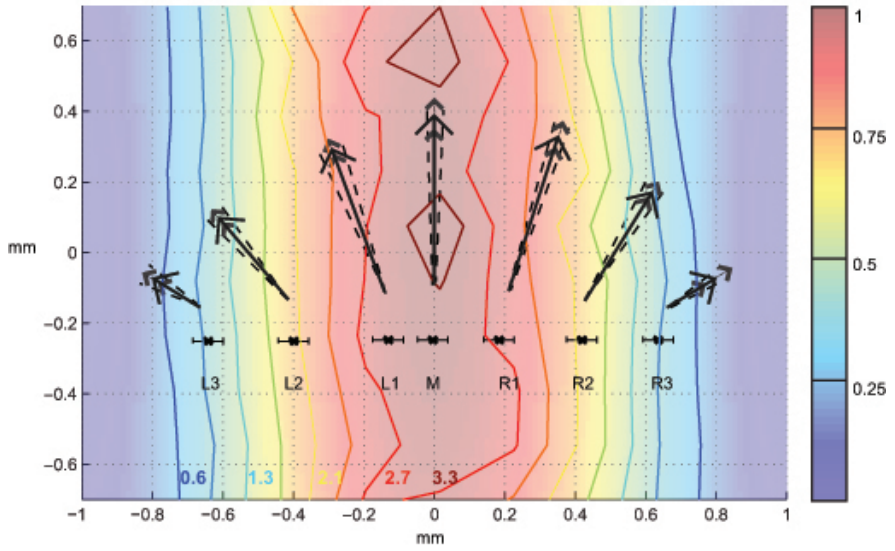

Figure 4.17: Summary of all experimental observations at varying transverse locations - Experimental observations (n>10) for each position (L3-R3), detailing jetting angle to field axis, and length. Standard deviations in angle (dashed lines) and length (small arrow-heads) are depicted. The coloured background is the normalised simulated ultrasound pressure field (scale on the right) at the focus, via a projection technique. (x) are the positions of plasma formation on absorption of the laser pulse, which can be observed as bright regions in the first few frames (i) of fig. 4.16

laser-pulse, which can be observed as bright regions in the first few frames in fig. 4.16. The translation of the LIC from the plasma location during the jetting phase (collapse), also due to HIFU radiation force, may be inferred.

A qualitative ray acoustic depiction of the radiation force interaction with the surface of a LIC is shown in fig. 4.18. The Gaussian distribution of the HIFU intensity is represented with coloured arrows matching the axial field map of fig. 4.17. Less 'intense rays' are predominately reflected (coloured dashed lines) off the surface at angles closer to the normal of the bubble surface, at the point of incidence. More intense rays, towards the centre of the distribution, are reflected obliquely from the surface and therefore do not impart as high a proportion of the incident momentum. Greatest momentum transfer therefore occurs halfway along the arc of the LIC-HIFU interaction, resulting in an involution as depicted (dashed line).

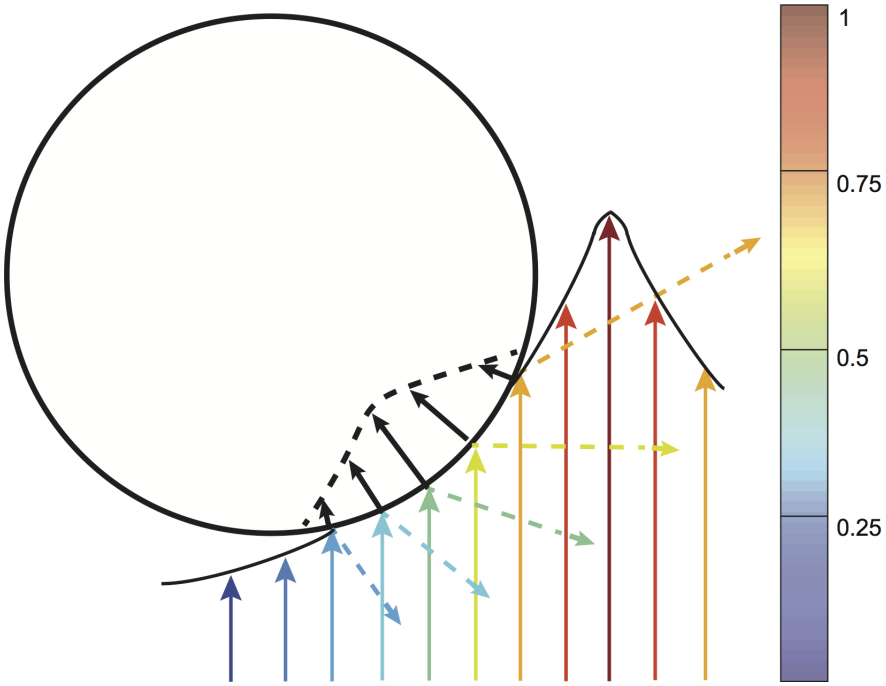

Figure 4.18: Ray acoustic approximation of LIC-HIFU interaction - a lateral position of L2 fig. 4.16 is depicted

4.4.5 Analysis

In order to support the hypothesis that radiation forces are responsible for the controlled jetting direction, a finite element model[1] can be used to predict the radiation force distribution across the surface of the cavity at maximum inflation. The results are shown in the form of a 'force-distribution map' on the simulated bubbles depicted in columns (iii) and (iv) of fig. 4.16. The HIFU radiation pressure is strictly a stress tensor in the Eulerian frame (but the term pressure is conventionally used) and is a second-order time-average quantity resulting from the non-linear terms in the Navier-Stokes (N-S) equations. In the non-viscous approximation, this second order force can be approximated as a function of the first order acoustic variables obtained from a linear scattering analysis, which is computationally simpler than solving the N-S equations directly. The situation is further complicated by the fact that the cavity boundary itself is moving. The time-average radiation force $< \vec{F_r} >$ on a section dA of a moving boundary can

[1]this model was implemented by Dr P. Glynnne-Jones, Engineering Sciences, University of Southampton. His contribution is gratefully acknowledged.

be approximated by eq. 4.9, evaluated at the boundary's mean position.

$$\frac{< \vec{F_r} >}{dA} = n(< V > - < K >) + \rho < (\vec{n} \cdot \vec{u_1})\vec{u_1} >, \tag{4.9}$$

where $< V >$ and $< K >$ are the first order (i.e., linear) time-averaged potential and kinetic acoustic energy densities respectively, ρ the fluid density, $\vec{n}$ the surface normal, and $\vec{u_1}$ the first order acoustic velocity vector. Theoretical analysis of the instantaneous radiation force distribution acting on the LICs at the various positions within the ultrasound field was performed with a 3-D linear acoustic model of the cavity, constructed in COMSOL v4.1. The spherical cavity is surrounded by a cuboidal domain of fluid of side 2.5 mm. The fluid is terminated with non-reflecting boundary conditions which allow an incoming wave to be introduced, of PNP selected according to the experimental conditions, and outgoing energy to be absorbed. The particle and fluid domains are coupled such that only normal velocity components are transmitted across the boundary, as depicted qualitatively in fig. 4.18. The model is solved using a harmonic analysis at the frequency of interest. The properties inside the bubble are based on the equilibrium pre-collapse temperature and pressure condition used in the expression for the Rayleigh collapse time eq. 2.8 (see §2.2.1). Where p_0 is the hydrostatic pressure and p_v the vapour pressure of water (2330 Pa at 20°) inside the bubble at R_{max}. For the LIC's of figs. 4.15 and 4.16, eq. 2.8 yields collapse times (τ_c) of 36 μs. The cavity and the surrounding water were therefore modelled as fluids with densities of 0.8, 1000 kg/m^3, and associated speeds of sound 435, 1500 m/s, respectively. In any case, the modelled result is dominated by the water properties and insensitive to changes in cavity properties over several orders of magnitude. The radiation forces normal to the boundary are evaluated from eq. 4.9 and show good qualitative agreement with the experimentally observed jets, fig. 4.16 column row (vii), both in terms of the direction of emergence and with stronger force distributions resulting in longer jets.

The largest angle of jetting observed is $\theta = 58°$) at 640 μs from the ultrasound axis. Assuming cylindrical ultrasound symmetry around the axis, this indicates that jet direction can be controlled through a solid angle, $\Omega \sim 0.94\pi$ steradians, with the focused ultrasound field used here. Jetting may occur at distances further from the axis (and therefore at still larger angles), but the secondary re-inflation of the LIC following the initial collapse, prevents meaningful measurements being taken.

4.4.6 Discussion

In this chapter, the interaction between an LIC formed with a laser-pulse of energy above the threshold value for optical breakdown, and a burst of propagating HIFU is investigated. The principle finding is that a jet results from this interaction, with length and direction characteristics dependent on the intensity and relative positioning, respectively, of the HIFU field. Previously accepted jetting mechanisms that rely on a pressure gradient to induce asymmetrical collapse do not adequately explain the observations made. For example, inspection of fig. 4.17 reveals that for an LIC at the central location, M, there is little or no pressure gradient existing along the axis of the focus, and yet the most prominent jetting occurs from bubbles at this position. Moreover, the pressure gradients within individual wavelengths of the propagating HIFU do not provide a convincing mechanism as very short bursts of HIFU did not yield observable jetting effects. Rather, the action of the radiation force exerted upon the cavity throughout the collapse, is implicated. The added acceleration at one region of the cavity wall provides the asymmetry required for a jet to form. An acoustic radiation force model provides supportive analysis for the case of LIC's at various lateral positions across the HIFU focus.

4.5 Jet-manipulation with HIFU in proximity to a surface

As detailed in §2.2.1, much of the early cavitation research was undertaken in an effort to elucidate the mechanism of cavitation erosion, such as that which affects ship propellers, fig. 1.1. Jet-formation from cavities in the proximity of a surface, represented in fig. 4.14 (ii) above, has been a prime candidate for the bubble dynamic responsible.

In this section, results from a pilot study into the feasibility of manipulating the natural tendency for jets to form directed toward a surface, with a burst of HIFU, are presented. The rationale was that the fine control afforded by the radiation force via the HIFU intensity (see §4.4.3) and focal alignment (see §4.4.4) actuation mechanism, might be used to suppress, or indeed enhance, surface-jetting effects. A crucial parameter for the consideration of surface-jetting is the dimensionless 'stand-off parameter', defined as $\gamma = d/R_{max}$, where d is the distance of the bubble centre normal to the surface and R_{max} the maximum radius of the oscillating bubble. γ and the Young's Modulus of the surface material are the principle factors that determine the jetting dynamic, in a liquid such as water. A $\gamma < 1$ indicates the bubble expands into contact with the surface, before R_{max} is reached. Bubble-surface systems with $1 < \gamma < 3$ generally yield the most pronounced jetting effects, with γ's > 10 tending to produce little or no jetting activity.

Introducing a surface to the sonoptic chamber for the results presented below, a 155 μm thick glass microscope coverslip (Scientific Laboratory Supplies Ltd., UK) was mounted horizontally within the sonoptic chamber, in the vicinity of the HIFU focus. The LIC may be precisely located relative to the surface, pre-determining γ for a given laser-pulse energy (and therefore R_{max}), via micro-translation of the surface. Two configurations are investigated, (i) HIFU-LIC-

surface, for which the LIC is located below the coverslip, and (ii) HIFU-surface-LIC, whereby an LIC is generated above the coverslip.

In both situations, it is important to assess the effect of the coverslip on the HIFU propagation. To achieve this, fibre-optic hydrophone measurements were conducted on-axis, at the centre of the focus, with and without the coverslip located just below the hydrophone tip. This simple test indicated that, for the range of intensities employed here, $\sim 30\%$ of the HIFU is attenuated by the coverslip. A significant portion may be reflected back to the LIC, in the HIFU-LIC-surface configuration. For the proof-of-principle demonstration here, however, reflected components are neglected and a propagating HIFU field assumed. For the HIFU-surface-LIC configuration, the HIFU intensity reaching the bubble is compensated by increasing the gain of the power amplifier, appropriately. In this way, the results generated below may be considered qualitatively comparable, to a first approximation.

4.5.1 High-speed observations of jet-enhancement

Fig. 4.19 row (a), are selected images extracted from a high-speed sequence recorded at 0.5 Mfps, representing an LIC-surface configuration (with no HIFU incident), for $\gamma \sim 2.55$. The lower surface of the glass coverslip is just visible across the top of these images, and becomes blurred as it extends out of the imaging plane of the viewing objective lens. The constraining influence of the surface on the collapse of the LIC is apparent at $t = 74\ \mu s$, as a flattening of the cavity wall distal to the surface. During the rebound, an upwardly directed jet forms, clearly visible at $t = 94\ \mu s$, consistent with reports in the literature. For this particular jetting event, γ is too large for the jet to make contact with the surface and it disintegrates, around $t = 100\ \mu s$, after jet stagnation.

Figs. 4.19 row (b) illustrates the effect of a HIFU burst of PNP = 3.3 MPa, incident to the LIC on the axis of propagation, and around the moment of maximum inflation, representing a HIFU-LIC-surface configuration. As for §4.4.3

and §4.4.4, the moment of HIFU arrival is apparent through the formation of secondary LNAC clouds around the primary LIC. At $t = 74\ \mu s$, the collapsing cavity exhibits a much higher degree of flattening at the wall distal to the surface, attributable to the additional acceleration conferred by the radiation force, from the HIFU incident from below. At 94 μs, a jet protrusion is apparent, of a similar length to the jet in the equivalent image of row (a). However, a vapour-jet envelope is also evident which may have acted to reduce the jet-velocity, following cavity wall penetration. Interestingly, the LNAC clouds appear to flow inwards toward the jet-funnel, however, the primary HIFU radiation force may also act to propel the clouds in a similar direction. Most notably at $t = 104\ \mu s$, the jetting has been sustained such that the longer jet that results actually makes contact with the surface, prior to disintegration. The reflection of the jet-tip, from the glass surface, is just visible it approaches the coverslip.

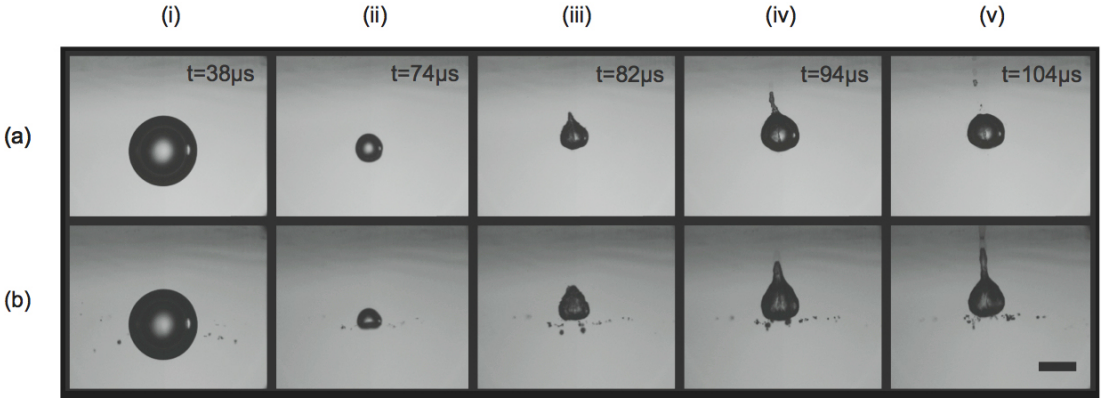

Figure 4.19: LIC-surface configuration with $\gamma \sim 2.25$ - The glass coverslip is mounted in the cavitation chamber, above the focal position of the laser-pulse. (a) the collapsing LIC forms a jet directed toward the surface, but γ is too large for the jet to make contact. (b) A HIFU burst of PNP = 3.3 MPa is incident to an equivalent system from below. The 'enhanced' jet, aided by the HIFU interaction, is longer-lived and makes contact with the glass surface. Scale bar: 400 μm.

Fig. 4.20 presents equivalent observations for a LIC-surface system of $\gamma \sim 2.05$, small enough for the jet to make contact (unaided by HIFU exposure), row (a) at = 98 μs. For this system, a counter-jet also forms (Blake and Robinson [8]), visible at 86 μs. For the HIFU-LIC-surface system of row (b) the added influence of the burst is again apparent at 76 μs, with the extra compression

yielding a deeper involution. As for fig. 4.19, the HIFU interaction results in a distinct vapour-jet forming. At 98 μs, the jet-interaction with the surface is notably more pronounced, with at least the vapour-jet envelope spreading out along the horizontal surface, following impact. This may also be the reason for the cavity disappearing at $t = 122$ μs, as the vapour-jet interaction may provide a release mechanism for the vapour and gas internal to the bubble.

For the HIFU-LIC-surface systems above, the radiation force jet-actuation is complementary to the tendency for the jet to form directed toward the surface. Depending on γ, the HIFU interaction can either increase the jet length such that it impacts on the surface (when it otherwise would not have) or accentuate the interaction of the jet with the surface, likely generating a higher water-hammer pressure. Accordingly, the term *jet-enhancement* is applied.

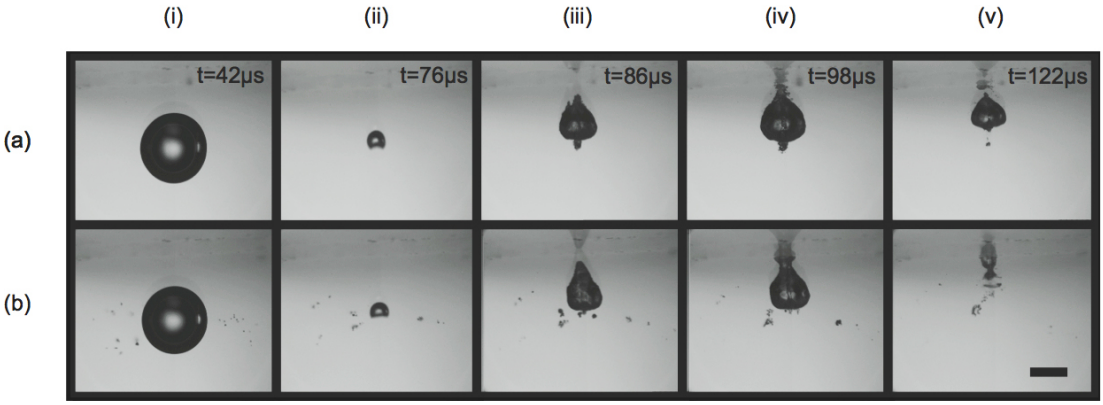

Figure 4.20: LIC surface configuration $\gamma \sim 2.05$ - Surface above the LIC (a) no HIFU incident, contact is made between the jet and the surface. (b) 'enhanced' jetting at equivalent γ results in a more energetic impact of jet onto the surface. Scale bar: 400 μm.

4.5.2 High-speed observations of jet-suppression

In the second configuration, HIFU-surface-LIC, the glass coverslip is lowered towards the transducer by ∼2mm, to provide a surface just below the centre of the acoustic focus. Fig. 4.21 row (a) depicts surface induced jet-formation from an LIC at $\gamma \sim 2.05$, i.e. the inverted geometry to fig. 4.20 row (a). In a mirror

image of that dynamic, a downwards directed jet forms with γ small enough for contact with the surface to be made. The bubble is notably elongated along the axis normal to the surface, during the collapse at $t = 64\ \mu s$. An upwardly directed counter-jet is also apparent at $t = 96\ \mu s$. Fig. 4.21 row (b) represents and equivalent surface-LIC configuration, with HIFU of PNP = 6.5 MPa (measured without the coverslip present) incident to the system. At $t = 64\ \mu s$, the bubble has retained a spherical shape, in contrast to the case where no HIFU was present, row (a). Nonetheless, a downwards directed jet-like structure emerges from the apex of a 'hot-air balloon' shaped bubble, at $t = 96\ \mu s$. The secondary LNAC clouds that form on HIFU arrival to the region, adopt positions strongly suggestive of the streaming that might be anticipated around the jet-funnel region. In contrast to 4.20 row (a), the HIFU radiation force will act to displace the clouds away from the primary LIC, and does so for clouds at the edges of the image. The clouds closer to the primary bubble, which will be shielded from the primary field to an extent, are free to follow the local flow of the host medium. 4.21 row (c) again represents an equivalent HIFU-surface-LIC configuration, but with HIFU of PNP = 7.7 MPa (measured in the absence of the coverslip). At 64 μs, an upwardly directed involution structure (arrowed white) has developed from the cavity wall closest to the surface, visible within the collapsing LIC. Closer inspection indicates this structure may have already disintegrated, likely as a consequence of intense HIFU propagating through the glass coverslip. The centroid of the bubble-debris left when the primary LIC has collapsed, at $t = 96\ \mu s$, is around the same distance from the surface as the centre of the previously expanded cavity, $t = 38\ \mu s$. Increasing the HIFU intensity further, to a PNP = 8.9 MPa, fig. 4.21 row (d) produces a similar unstable involution, and the rippling effect along the cavity surface closest to the surface, reported above §4.4.3 for HIFU of PNP > 6.5 MPa (with no surfaces present). Despite the disrupted involution, jet-like behaviour imposed onto the bubble debris is apparent, at 96 s. The 'upside-down T' shaped cloud has translated away from the surface by

$t = 126\ \mu s$, with the central region displaying dynamics reminiscent of the LNAC translational dynamics reported, §3.8.

These results suggest that HIFU propagating across a surface can act to reduce, row (a), neutralise, row (b) and reverse, row (c), surface-jetting from a proximal cavity, aligned to the propagation axis. The HIFU-surface-LIC configuration presents competing mechanisms for jet-formation from a cavity, and as such, the term *jet-suppression* is used.

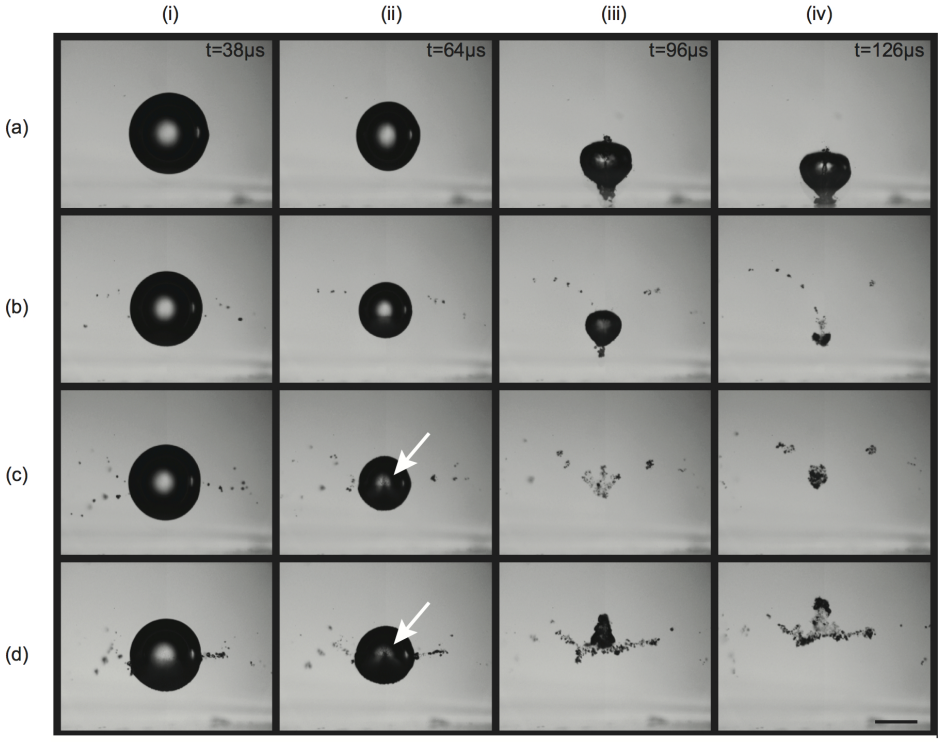

Figure 4.21: HIFU-surface-LIC configuration - with $\gamma = 1.72$ (a) Downward directed jetting toward the surface below the LIC. (b d) Radiation force actuation competes with the surface-induced jet mechanism, to (b) reduce the jetting dynamic, at PNP = 6.5 MPa incident to coverslip, (c) neutralise jet-formation for PNP = 7.7 MPa incident and (d) effectively reverse the jetting direction, at PNP = 8.9 MPa incident to coverslip. Scale bar: 500 μm

4.5.3 Discussion

Introducing a surface to the sonoptic chamber facilitated a preliminary study of LICs subjected to dual jetting mechanisms. The degree of control over radiation force actuation afforded via the intensity of the HIFU generated, can be superposed to the dual-mechanism case, such that surface-jetting can be enhanced or suppressed according to the HIFU orientation.

The observations of fig. 4.21, might suggest a potential application for the approach to the protection of surfaces, that would otherwise be subject to cavitation erosion. However, the complexity involved with implementing a detection and HIFU-administration system deems this highly infeasible. Medical applications would seem likely to provide the context for which the results may have significance. Lithotripsy refers to procedures undertaken to fragment urinary tract calculi, for removal by natural means, or via a stent. Two approaches are adopted clinically; Extra-corporeal Shock-Wave Lithotripsy (ESWL) and laser-lithotripsy, each of which result in cavitation activity in the region of the stone. ESWL involves delivering focused hydraulic shocks to the target region, with contributing mechanisms of spallation, compression and cavitation effects identified (Coleman and Choi [23], Ikeda *et al.* [60]). Laser lithotripsy refers to the delivery of optical energy directly to the site of the stone, through an optical fibre coupled to the source, typically a Holmium:YAG laser ($\lambda = 2.1\ \mu m$). The role of jetting from cavities formed from either of these modalities is not entirely known, however, a burst of HIFU for jet-enhancement, §4.5.1, could act to break stones more efficiently.

As discussed previously, cavitation is of particular interest for the purpose of drug-delivery to cells, including *in-vivo* (see §2.1.4). A particularly promising approach is the combination of HIFU and (contrast agent) microbubbles delivered intravenously. Again, the contribution of microbubble-jetting to such an approach to therapy is not fully resolved, although a number of studies have indicated the dynamic is feasible (Prentice *et al.* [105]), including in *ex-vivo* vasculature (Chen

et al. [20]). Indeed, the latter reported reversed microbubble-jetting, away from vessel wall, and attributed the observation to the proximity of a compliant boundary. It was not clear from this paper what the orientation of the HIFU transducer to the vessel-microbubble system was, during exposure. However, the surface-jet suppression detailed in §4.5.2 may be significant. Certainly the HIFU pressure amplitudes used were comparable to those employed for the jet-manipulation observations here. In any case, the dependence of jet characteristics on HIFU intensity and alignment, is an important consideration for future experiments undertaken to progress this field, ultimately toward clinical application.

5

Conclusions and future work

Overview The novelty of this work comes from the capability of observing acoustic cavitation at framing rates sufficient to resolve key behaviour in response to MHz HIFU driving frequencies. Previous observations have invariably used lower driving frequencies and more often than not, involve standing wave configurations.

The following summarizes the key conclusions from the preceding results chapters. A short discussion follows for possible future work, that may be considered.

- The conceptually simple innovation of the sonoptic chamber, facilitated the development of the laser-nucleation technique that underpinned the observations. The key feature of this chamber is that the acoustic-standing waves, associated with vast majority of observations reported in the literature, are avoided.

- The significant advantage conferred through direct observation of cloud behaviour is highlighted by §4.2, the cloud oscillation results, for which preliminary observation of bubble-ensemble oscillations guided the target bandwidth required for acoustical detection. The corroborating spectral features in the acoustic spectra, and the process of extracting cloud-size information from this data, is considered to be the most important result emerging from this research.

- The physical translation of cavitation clouds under the action of the radiation force exerted by the primary field, is analysed as a function of HIFU intensity. A resonance 'coupling phenomenon' is identified to account for the unexpected rapid translation of small clouds, at low intensity.

- For laser-pulses above the breakdown threshold, HIFU incident to the LIC that results, mediates jetting that is a function of the intensity and relative positioning to the HIFU focus. Analysis reveals a radiation force mechanism underpins the jetting process. Preliminary observations indicate HIFU-actuated jet-formation can be used to control jetting in LIC-surface configurations.

In the following 'Future Work' section, discussion is limited to how the key observation of cloud oscillation, and directly correlated acoustic emissions, might be progressed and developed, to provide a platform for the next generation of FUS-procedures whereby enhanced therapy is mediated by cavitation. This is divided into two subsections: (i) *cavitation-on-demand* and (ii) *translation toward clinical application*. The former is a discussion of various adaptations that could be implemented in the existing experimental set-up, with a view to achieving the capability of monitoring, controlling and manipulating cavitation. An overriding objective to the suggestions made would be the demonstration of sustaining a certain level of bubble activity, possibly indefinitely. For translational work, (ii), a number of modifications could be attempted to allow for the assessment of bioeffects from 'characterised' cavitation clouds. This was the ultimate purpose of this work from the outset - however, it should be emphasised again here that cavitation developing in tissue may be expected to be somewhat different to the activity in water, observed during this work - although some direct relevance may be expected for cavitation in blood and other bodily-liquids such as urine in the bladder and cerebral spinal fluid (CSF).

Although the subsections are treated separately, any progress made toward cavitation-on-demand will almost certainly aid the goal of translation and imple-

mentation of cavitation for therapy.

(i) Cavitation-on-demand cavitation is universally considered as a somewhat random and uncontrollable (and potentially violent and destructive) phenomenon. The results presented in this thesis hint at the possibility that cavitation could in fact be monitored, possibly controlled and even manipulated.

In an application such as a FUS-procedure (or anywhere the host medium is not transparent), for which cavitation activity cannot be observed optically, the two principle unknown factors are the precise location of activity and the volume throughout which it has spread. The latter is somewhat addressed through the results of §4.2, which indicate cloud size can be inferred from the frequency content of the acoustic emissions.

To address the former issue, a spatially configured hydrophone-array could feasibly deliver a signal-triangulation approach, to pin-point the exact location of activity. The combination would thus provide a 'characterised cavitation field', that for FUS, could be mapped to an anatomical image obtained by diagnostic ultrasound, MRI or CT (computed tomography).

For 'naturally' occurring cavitation, the nucleation of single cavitation clouds is an unlikely scenario. Generally, there will be multiple nuclei (see §2.2.1, in the host medium, each of which may provide an origin for cavitation activity. Assessment of cloud-cloud interactions is therefore important for the application of the results gathered here to 'real' situation where cavitation occurs.

This could be achieved with a simple beam-splitter configuration added to the beam path for the laser-pulse, before it is focused into the cavitation chamber to nucleate cavitation. In this way, two (or more) LNAC sites may be controllably and reconfigurably generated, for exposure to the primary HIFU field. Factors such as the spacing between the clouds that form, and the orientation relative to the primary field, could be systematically investigated.

In terms of physically controlling a single cavitation cloud, of the type de-

scribed here, the option of introducing secondary HIFU sources would seem an attractive option. For example, the addition of a second HIFU transducer to the sonoptic chamber (in the upper inverted funnel, fig. 3.1 (see §3.2)), confocally aligned to the cavitation chamber, in opposition to the existing transducer, would allow a second radiation force to be exerted on the cavitation clouds, to retain the cloud position within the field of view. Moreover, novel acoustic landscapes such as an acoustic 'vortex beam' may also be applied to constrain activity.

Other HIFU parameters, not explored in this thesis, would also warrant investigation. The effects of (continuous) intensity exposure on the rate of translation of clouds under the HIFU radiation force, is documented in §4.3. However, intensity modulation would permit active control over the extent of cavitation development. For example, a higher intensity at the start of an exposure would act to grow a cloud rapidly (via promoted fragmentation) up to a certain level, following which a reduced intensity could be applied to sustain the required level of activity. Pulsed wave HIFU, whereby a certain duty-cycle is applied to the exposure, may also provide a control mechanism for the extent of cavitation activity delivered.

In combination, this 'suite' of cavitation control mechanisms could feasibly deliver cavitation-on-demand. The outstanding challenge for this work would be to maintain a cavitation cloud for a fixed amount of time, possibly indefinitely.

Furthermore there is the possibility of implementing a rapid response, automated control feedback-loop system to do this independently. Here the input to the system would be the hydrophone signal (array), which provides information on the cloud size (location). Automated parameter modulation from the various driving and manipulation sources would then control the development to a user-defined level.

In conjunction with the experimental advances outlined above, a portfolio of cavitation models is critical to provide theoretical understanding for the observations made. Particularly, the intra-cloud bubble interactions and the factors

determining the level of fragmentation needs attention, as they are central to cloud response to a given HIFU exposure. The Rayleigh-Plesset robustness analysis of §4.2.3, confirmed that the host medium material properties have a key role in determining the evolution of clouds. As such, models should accommodate variation of these parameters, especially around the values applicable for across a range of tissue types and pathologies.

(ii) Translation towards clinical application Although significant insight into HIFU-driven cavitation activity in water is provided through the results of this thesis, the relevance of the observations to cavitation in tissue is limited - although they may still be applicable to cavitation in vasculature for drug delivery and permeabilisation applications. Certainly, in bulk tissue, cavitation clouds may be expected to evolve quite differently on account of material properties, unknown nuclei characteristics and the effect of anatomical structures such as bone, or lung, on both the HIFU and the cavitation activity itself. A substantial effort will be required to translate the *in-vitro* observations gathered here, to enhanced therapy for FUS-procedures.

Nonetheless, once the development of the strategies and devices outlined in (i) above have been tested and refined on known cavitation fields (observed through high-speed photography), proof-of-principle studies, involving tissue-mimicking materials (TMMs) and *ex-vivo* tissue, would provide a significant step toward realising this objective.

Evidently, using a laser-pulse to nucleate cavitation activity in turbid media (such as tissue) is unlikely to be feasible. Pseudo-transparent TMMs, however, could provide a platform from which cavitation-enhanced heating effects could be assessed. Moreover, TMM samples seeded with fluorescently loaded drug delivery vehicles (liposomes and microbubbles, for example) could be used to investigate drug delivery potential. Further translation to re-perfused animal and cadaver models would then be feasible, as a precursor to human-trials.

6

Appendix

6.1 Appendix A: Dark pixel counting

This appendix provides a detailed description of of the dark pixel technique, used to analysis the high-speed camera data for the bubble-ensemble oscillation dynamics §4.2. Fig. 6.1 is the entire high-speed sequence recorded from which sequential frames were extracted for fig. 4.1 (see §4.2, outlined red). Consistent with the name of the technique the simple algorith in MatLab (below) searches for pixels that are not a part of the background inside a set of threshold values. The output of the algorithm is a temporal dependence of the bubble-ensemble (summed bubble area) with time, fig. 6.2.

For a system that is responding circa $f_0/2$ (for stable cavitation driven at $f_0 =$ 0.521 MHz the Nyquist sampling requirements for full resolution is f_0. Therefore a high-speed imaging rate of 1 Mfps is sufficient. Inspection of fig. 6.2 suggests that perhaps some of the compression phases are not exactly identified, but the method holds for the general purpose. In this case the yellow arrow indicates the frame identified as the minimum summed bubble area value for the cloud in question (also outlined in green in fig. 6.1 which cursory inspection confirms). Likewise for the yellow arrow. The values for R_0 in fig. 4.2 are determined in

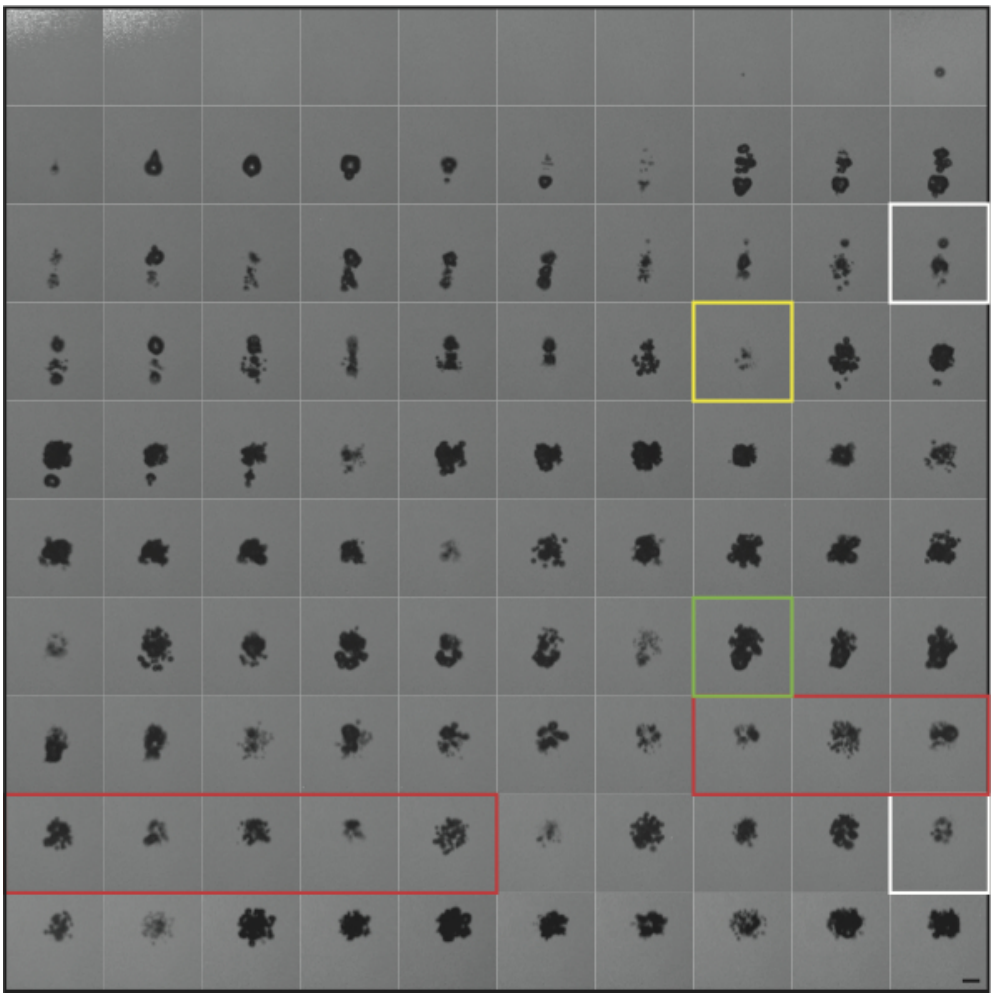

Figure 6.1: Complete high-speed sequence for LNAC cloud 4.1 (c) - in pre-existing HIFU of PNP = 1.04 MPa, captured with the Shimadzu camera operating a 1 Mfps. Individual frames relevant to dark pixel counting technique are highlighted: in white start and end point for spectra analysis (see fig. 6.3); yellow frame has lowest pixel count (see fig. 6.2); green highest pixel count (see fig. 6.2); red shown in fig. 4.1. Scale bar 50 μm.

the interval between the two frames marked in white from t= 30μs to t=90 μs, during which a stable cloud of resonant bubbles size has been established.

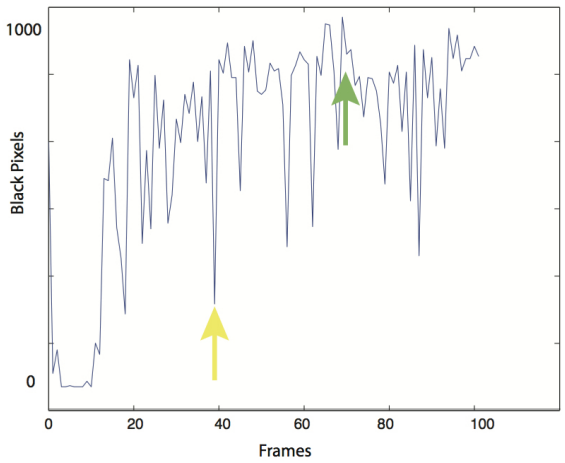

Figure 6.2: Variation of summed bubble area with time - The output of the dark pixel counting algorithm plotted against the frames

The Fourier transform of fig. 6.2 yields the high-speed spectra of fig. 4.1, also presented below as fig. 6.3. All speed sequence spectral information gathered in this way demonstrated remarkably good agreement with the corresponding acoustical data, despite the stated limitations.

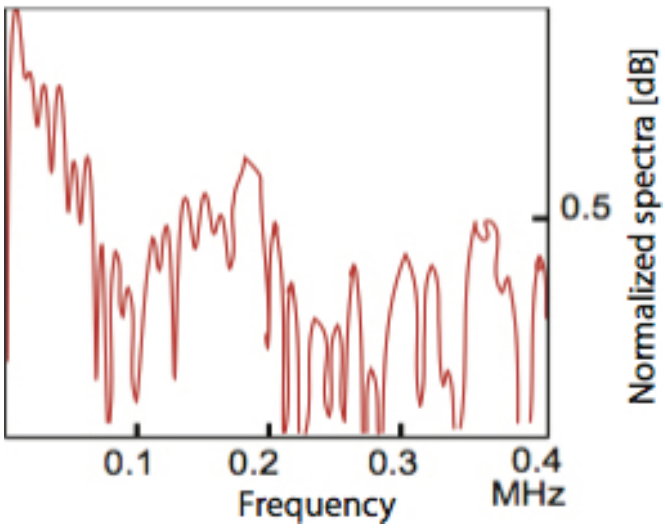

Figure 6.3: Bubble-ensemble oscillation frequencies - obtained from implementation of a FFT to fig. 6.2

```
function cloud_scillation_analyzer(Pathname,fps)

%------------------load frames into ...
    matlab-----------------------------------
home=pwd;
cd(Pathname);
jpgfiles=dir('*.jpg');
tiffiles=dir('*.tif');
if(¬isempty(jpgfiles))
     for u=1:length(jpgfiles)
         Filename_sequence{u,1}=['/',jpgfiles(u).name];
     end
     txtfile=dir('*.txt');
% datfile=dir('*dat');
% if (isempty(txtfile)==0);
%---------load fps-----------------
[names, types, fps, y, answer]
= textread(txtfile.name,'%s %s %d %s %s', 1);

else
    for u=1:length(tiffiles)
         Filename_sequence{u,1}=tiffiles(u).name;
     end
end

dt=1/fps;
fr=1:length(Filename_sequence);
t=0:dt:(length(Filename_sequence)-1)*dt;
frame_now=imread([Pathname,Filename_sequence{1}]);
frame_now=frame_now(20:end-20,20:end-20,:,1);
BW = im2bw(frame_now, 0.00000001);%graythresh(frame_now));
images = zeros([size(BW) length(Filename_sequence)]);
% m = zeros([size(BW) 1 2]);
for l=1:length(Filename_sequence);

     frame_n=imread([Pathname,Filename_sequence{l}]);

     frame_no=frame_n(:,:,1);
     frame=zeros(size(frame_no));

     frame_now= imadjust(frame_no);

     BW = im2bw(frame_now,0.0000000001);%graythresh(frame_now));
     BW=not(BW);
     [B,L,N] = bwboundaries(BW,'noholes');
     %imshow(frame)
     %hold on

%---------------detect single bubbles--------

for k =2:length(B)
     boundary = B{k};
     s=size(boundary);
     s=s(1,1);
     if (s>1)
         for k=1:s
         frame(boundary(k,1), boundary(k,2))=1;
         end
```

```
    end
end
se90 = strel('line', 1, 90);
se0 = strel('line', 1, 0);
BWsdil = imdilate(frame, [se90 se0]);
BWdfill = imfill(BWsdil, 'holes');
BWdfill=bwareaopen(BWdfill,5);
BWdfill=BWdfill(20:end-20,20:end-20,:,1);
%------------sum pizels-------------
blackcount = sum(sum(BWdfill==0));
whitecount = sum(sum(BWdfill==1));

        volume(l)=0;

        volume(l)=whitecount;%-blackcount;
%         if volume(l)==0
%             volume(l)=volume(l-1)
%         end



images(:,:,l)=BWdfill(:,:,:);
%images_3(:,:,l)=BW(:,:,:);
      images2(:,:,l)=frame_no(20:end-20,20:end-20,:);
       imagefus(:,:,l)=[gray2ind(images(:,:,l)),images2(:,:,l)];

end
volume(1)=volume(2);
%figure
t=0:dt:(length(Filename_sequence)-1)*dt;
%ti=0:dt:(length(Filename_sequence)-1)*dt;
%volume=interp1(ti,volume,t);
volume=sqrt((volume)./(pi))./0.24;
vol=volume(30:70);
mean(vol)
max(vol)
min(vol(vol>0 & vol<mean(vol)))
%---------------time plot---------------

figure
plot(t,volume)


%mean(volume);
volume(1)=0;
%implay(images_3)
cd(home);

%implay(imagefus)


%*********Spectrum plot********


volume=[volume,zeros(1,2001)];
% t_interval=[0 max(t)];%time interval to analyse
% jj=find(t>t_interval(1) & t<t_interval(2));
```

```
% t_data=t(jj);
 Data=volume;
% ii=find(t_data>0);
% Data(ii)=0;
F=1:length(Data);
F=F-mean(F);
F=F/length(Data)*fps;
FFT=fftshift(fft2(ifftshift(Data)));
jj=find(F≥0);
%figure;plot(F(jj),20*log10(abs(FFT(jj)))),
grid on, axis([0 0.4e6 min(20*log10(abs(FFT(jj))))
max(20*log10(abs(FFT(jj))))])
```

MatLab code of dark pixel counting algorithm

6.2 Appendix B: Other significant high-speed observations

This appendix includes observations that were made with the high-speed cameras that are not directly relevant to the main avenues of investigation, for this thesis, but are nonetheless of some interest. The significance of each figure presented is contained in the accompanying each caption.

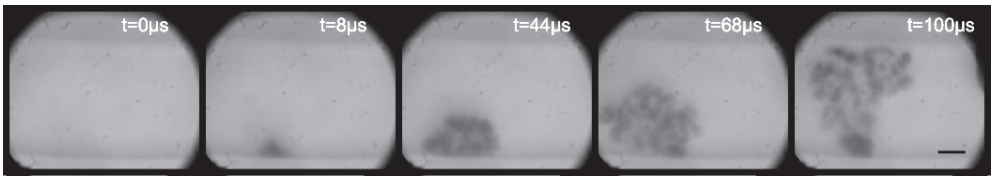

Figure 6.4: Cavitation in capillary - As discussed in §2.2.2 cavitation nucleates at a range of discontinuities in a host medium such as a boundary. A central premise of this work is that the acoustic cavitation can be nucleated via laser-pulse is equivalent to that which occurs naturally. The frames presented above represent a high-speed camera recording of a 'natural' nucleated cavitation event, when a capillary was placed inside the sonoptic chamber. The nature of cavitation nucleii is not clear however the cloud evolution is reconcilable to the main observations of LNAC, given the fluidic environment. HIFU of PNP is incident to a capillary vasculature model (ø200 μm) at the time of high-speed image acquisition. Scale bar: 50 μm.

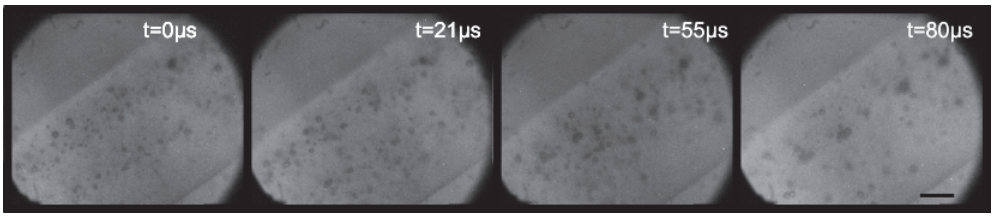

Figure 6.5: High-speed observations of UCA cavitation - A microbubble suspension is flowed through the capillary see fig. 6.4. HIFU of PNP equal to 2.0 MPa is incident at t=0 μs. Agglomeration of the microbubbles into clusters is apparent, consistent with (Kotopoulis and Postema [68]). The alignment of clusters parallel of the boundary of the capillary might suggest standing wave formation, but the HIFU excitation in-situ is not well characterized. Scale bar: 50 μm.

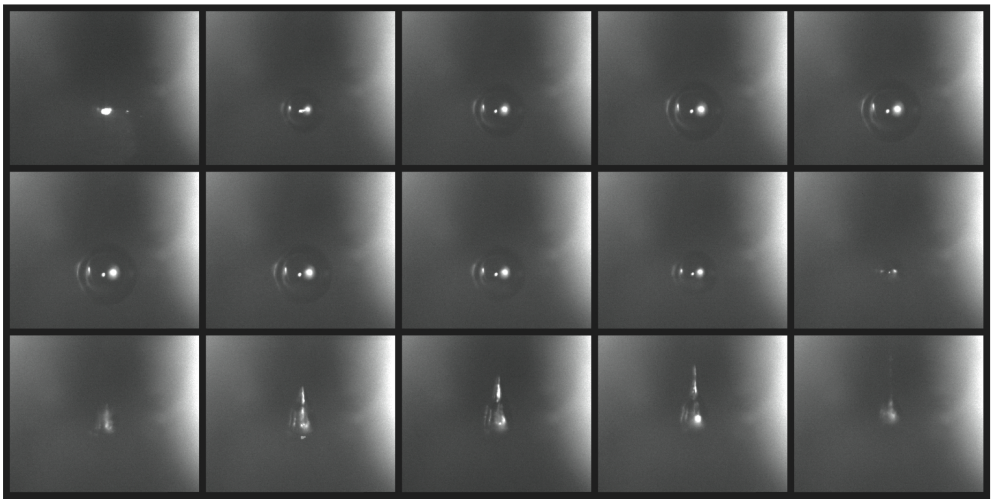

Figure 6.6: Jet observed with front illumination - for HIFU of PNP = 3.3 MPa to an LIC located on the propagation axis, recorded through the 5× objective lens. All observations in the main thesis were undertaken with a back illumination configuration. As such, the presence of a cavity will act of scatter illumination from the recording CCD. Therefore a bubble appears dark on a light background in the image. An alternative approach is illumination from the viewing direction, where the scattering object will appear bright on a dark background. The disadvantage of this configuration is that a very intense light source is required. Alternatively a lower framing rate (125 kfps) can be used. Nonetheless, in this figure the jet structure is very apparent.

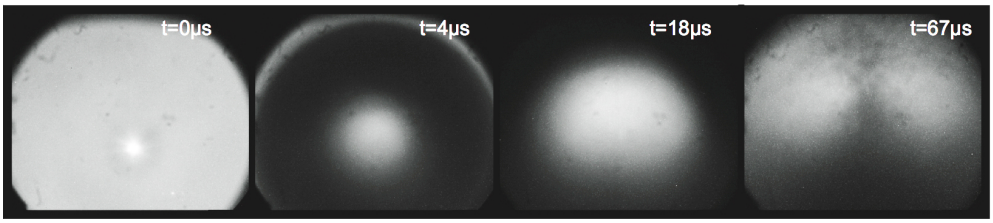

Figure 6.7: Disruptive involution of LIC under high PNP - taken in the parallel configuration with the 50× objective lens, at 1 Mfps.

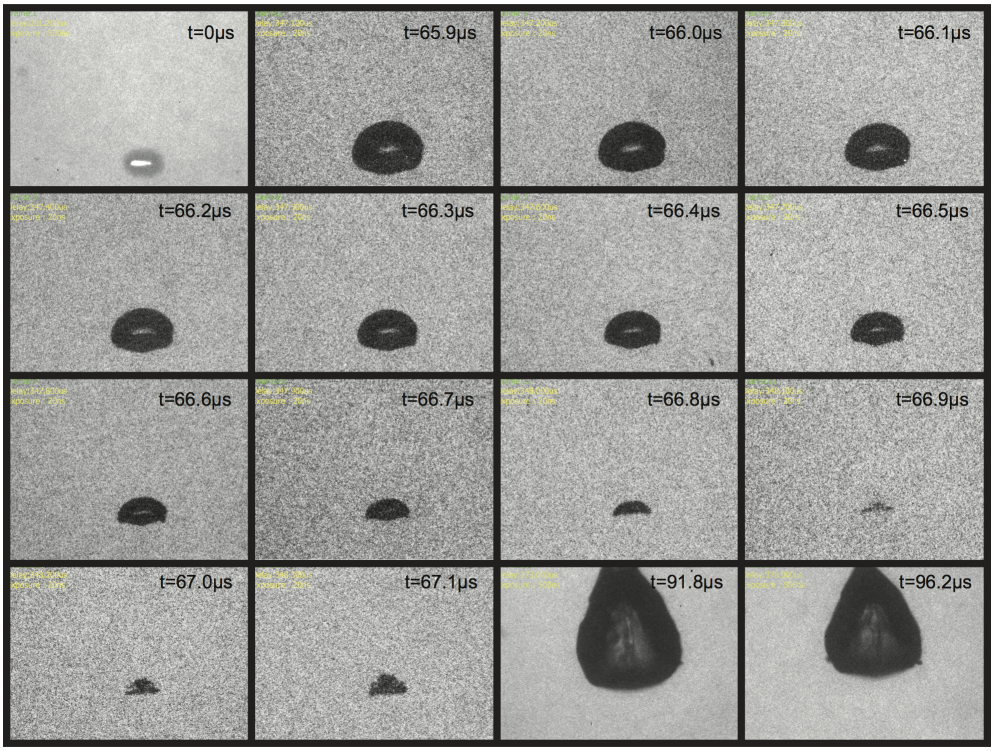

Figure 6.8: Highly temporally resolved collapse of jetting LIC - this figure represent observation around the moment of collapse for an LIC that jets, at 10 Mfps, under HIFU exposure. The flattening of the cavity wall exposed to the ultrasound is very apparent even around the moment of collapse. The first frame captured the plasma formation; the last two frames were triggered to capture the subsequent jetting.

6.3 Appendix C: Matlab code

In this appendix contains the MatLab code used for the main simulations and model discussed in this thesis. The code is complete therefore can just be copied to an Matlab editor and is fully operational.

6.3.1 Acoustic field simulation

This code is an implementation[1] of the theory described in detail in '*Fourier Acoustics*' (Williams and Mann [131]).

```
1
2  clear all;close all;clc;
3
4  % %#########Ideal spherical ...
       segment###################################
5  Opening=32;%opening angle in deg
6  N=101;P=zeros(N,N);
7  % non-even number of points helps to define single-valued c. ...
       freq. for FFT
8  freq=1.471e6;%frequency [Hz]
9  dx=0.1;dy=dx;%original field spatial resolution [mm]
10 %*************************************************************
11 %**********Window conditioning-cut or zero padding***********
12 Window=[20,20];%window size [mm] to cut or zero padd acoustic data
13 [P,xaxis,yaxis]=WindCond(P,dx,dy,Window);
14 zaxis=-5:.2:5;% points on Z-axis for 3D reconstruction
15 %************Build of spherical segment transducer k-space ...
       image**********
16 Pk=zeros(size(P));% Fourier image of the (zero) pressure field
17 SIZ=size(Pk);
18 c=1485e3;%sound speed in water [mm/sec]
19 lam=c/freq; %wavelength
20 K=2*pi/lam; %wavevector
21 kx=(1:SIZ(1))*2*pi/dx/SIZ(1);kx=kx-mean(kx);% k-space axes
22 ky=(1:SIZ(2))*2*pi/dy/SIZ(2);ky=ky-mean(ky);
23 [Kx,Ky]=ndgrid(kx,ky);
24 jj=find(sqrt(Kx.^2+Ky.^2)/K<tand(Opening));
25 Kz=sqrt(K^2-Kx(jj).^2-Ky(jj).^2);
26 Pk(jj)=1./Kz;
27 figure;imagesc(kx,ky,abs(Pk)');axis xy,axis equal,grid on
28 title('Spherical segment transducer k-space image')
29 %**********************3D ...
       reconstruction************************************
30 resample=[0.3,0.3];% improving resolution of output by resampling
31 Norm=1;% normalization to emmited power (1W)
32 [P3D,xaxis,yaxis]=Reconstruction(Pk,dx,dy,zaxis,freq,resample,Norm);
33 %**********Vertical plane plot**********
34 center=round(length(yaxis)/2);
35 figure;imagesc(xaxis,zaxis,squeeze(abs(P3D(:,center,:)))'),
```

[1] This code was implemented by Oleg Prus (Insightec Ltd.). I would like to thank him very much for all the support he has given me.

```
axis equal,axis xy,colorbar
xlabel('X [mm]')
ylabel('Z [mm]')
title('Spherical segment pressure [Pa peak] for 1W emitted')
%*********Orizontal plane plot**********
center=round(length(zaxis)/2);
figure;slice=imagesc(xaxis,yaxis,squeeze(abs(P3D(:,:,center))));
axis equal,axis xy, axis([-10, 10, -10, 10]),colorbar
xlabel('X [mm]')
ylabel('Z [mm]')
title('Spherical segment pressure [Pa peak] for 1W emitted')
```

Reconstruction:

```
function ...
    [P3D,xaxis,yaxis]=Reconstruction(Pk,dx,dy,zaxis,freq,resample,Norm)

% Pk - Fourirer image of the acoustic field
% dx,dy - real space resolution
% zaxis - 1D vector of points [mm] along Z-axis for reconstruction.
%Z=0 - initial field plane
% freq - ultrasound frequency [Hz]
% resample - two component vector for resample ratio ...
    resample(1)<(>)1 -
%increase (decrease) output resolution
% Norm -  0 - for no normalization. Peak pressure is equal to
%Voltage signal that should be measured in each point
%         1 - normalization by total power of the acoustic field to
%1W emmited
%         2 - normalization to momentum of the acoustic field as
%measured by absorbing target radiation force to 1W measured
% P3D - output 3D peak (not RMS!) presure in Pa [N/m^2]

c=1485e3; %sound speed in water [mm/sec]




SIZ=size(Pk);
lam=c/freq; %wavelength
K=2*pi/lam; %wavevector
kx=(1:SIZ(1))*2*pi/dx/SIZ(1);kx=kx-mean(kx);% k-space axes
ky=(1:SIZ(2))*2*pi/dy/SIZ(2);ky=ky-mean(ky);
%**************Zero padding or cut to match desired real-space ...
    resolution
%(resample)************
%**********x - direction*****************
if resample(1)>1 %cuting in kx-space to reduce real-space resolution
    jx=sort(find(abs(kx)<(max(kx)/resample(1))));
    fac=SIZ(1)/length(jx);% scale norm factor
    kx=kx(jx);
    Pk=Pk(jx,:)/fac;
else %pading for increase real-space resolution
    kx=padding2(kx,1/resample(1));
    fac=SIZ(1)/length(kx);% scale norm factor
    Pk=padding2(Pk,[1/resample(1),1])/fac;
end
```

```
dx=dx*fac;
%**********y - direction*****************
if resample(2)>1 %cuting in ky-space to reduce real-space resolution
    jy=sort(find(abs(ky)<=(max(ky)/resample(2))));
    fac=SIZ(2)/length(jy);% scale norm factor
    ky=ky(jy);
    Pk=Pk(:,jy)/fac;
else %pading for increase real-space resolution
    ky=padding2(ky,1/resample(2));
    fac=SIZ(2)/length(ky);% scale norm factor
    Pk=padding2(Pk,[1,1/resample(2)])/fac;
end
dy=dy*fac;
SIZ=size(Pk);
xaxis=(1:SIZ(1))*dx;xaxis=xaxis-mean(xaxis);
yaxis=(1:SIZ(2))*dy;yaxis=yaxis-mean(yaxis);
%*********Removing imaginary (non-propagating) harmonics to
%improve stability********
[Kx,Ky]=ndgrid(kx,ky);
Kz=K^2-Kx.^2-Ky.^2;
j0=find(Kz<=0);% imaginary K-wavevector harmonics
Kz(j0)=0;
Kz=sqrt(Kz);
Pk(j0)=0;

%********Normalization*********************************
rho=1e3;%water dencity [kg/m^3]
Za=c*1e-3*rho;%water acoustical impedance [kg/m^2/sec]
switch Norm
    case 0 %no normalization
        W=1;
    case 1 %normalization by total emiting energy
        %(Poynting vector integral)
                W=sum(sum(abs(Pk).^2.*Kz))/K/prod(SIZ)*dx*dy*1e-6/(2*Za);
    case 2 %normalization by total momentum in Z-direction
        %(Radiation force measurement with absorbing target)
             W=sum(sum(abs(Pk).^2.*Kz.^2))/K^2/prod(SIZ)*dx*dy*1e-6/(2*Za);
end
Pk=Pk/sqrt(W);
%*****************************************************

%****************3D volume reconstruction*******************
i=sqrt(-1);
P3D=ones(length(xaxis),length(yaxis),length(zaxis))*i;
%memory reserving for output array
for jz=1:length(zaxis)
    P3D(:,:,jz)=fftshift(ifft2(ifftshift(Pk.*exp(i*Kz*zaxis(jz)))));
    %slice reconstruction
    if mod(jz,10)==0
        disp(['Plane Z=',num2str(zaxis(jz)),'mm reconstruction'])
    end
end
%*******************************************************
```

WindCond

```
function [P,xaxis,yaxis]=WindCond(P,dx,dy,Window);
```

```
% [P,xaxis,yaxis]=WindCond(P,dx,dy,Window) - Window ...
    conditioning-cut or zero padding
% Window - window size [mm] to cut or zero padd acoustic data


SIZ=size(P);
xaxis=(1:SIZ(1))*dx;xaxis=xaxis-mean(xaxis);
yaxis=(1:SIZ(2))*dy;yaxis=yaxis-mean(yaxis);

%********Zero pading or cut to match defined Window***************
if Window(1)>max(xaxis)
    P=padding2(P,[Window(1)/max(xaxis),1]);
    xaxis=padding2(xaxis,Window(1)/max(xaxis));
else
    jj=sort(find(abs(xaxis)<Window(1)));
    P=P(jj,:);
    xaxis=xaxis(jj);
end
if Window(2)>max(yaxis)
    P=padding2(P,[1,Window(2)/max(yaxis)]);
    yaxis=padding2(yaxis,Window(2)/max(yaxis));
else
    jj=sort(find(abs(yaxis)<Window(2)));
    P=P(:,jj);
    yaxis=yaxis(jj);
end
```

6.3.2 Rayleigh-Plesset single bubble model

This code implements[1] the classical Rayleigh-Plesset equation (see eq. 4.1). The output if this code is the plot of $R(t)$ and its Fourier transform. A reiterating version (not shown) of the code was used to create the bifurcation diagram.

```
%the Rayleigh-Plesset model to simulate the
%behaviour of a single bubble and compare it to the behaviour of ...
    a cloud


%% Equation:
%R*(d^2R/dt^2)+3/2*(dR/dt)^2=1/rho*((p0+2*sigma/R0(i))*(R0(i)/R)^(3*k)+pv-2
%*sigma/R-p0-4*etha/R*(dR/dt)-P)
%%can be found in the acoustic bubble
%%
%time in seconds
%R in meters
%p in Pa
clear all;
close all;

    %% Set parameters
    R0=26.3*1e-6;
    P0=1.04*1e6;
```

[1] this model is based on a code written by Itay Rachmilevitch (InSightec Ltd.), I would like to thank him for the support to this research

```
19      freq=0.521*1e6;
20      mu0=freq/(2*pi);
21
22      %% time
23      T=1/freq;
24      dt=T/1e4;
25      t=0:dt:360e-6;
26      Nt=length(t);
27       %Number of cycles to build up pressure%
28      Nstart=5;
29
30
31      %% Material parameters
32      %Pascal ambient pressure
33      p0=1*1e5;
34      %kg/m^-3   water density
35      %[ref Physics of bubble oscillations Lauterborn]
36      rho=1.0*1e3;
37      %N/m (72 dynes/cm) surface tension
38      %[ref Physics of bubble oscillations Lauterborn]
39      sigma=72*1e-3;
40      %nobel gas
41      %[ref Physics of bubble oscillations Lauterborn]
42      k=5/3;
43      %Pascal vapour pressure
44      %[used 2330 in jet directed bubbles]
45      pv=0.02*p0;
46      %Pa s shear viscousity
47      %[in 0.001 Pa s ref Physics of bubble oscillations Lauterborn]
48      etha=0.894*1e-3;
49
50      %%%% empty arrays for R creation etc
51      R=ones(1,Nt)*R0;
52      Δ=zeros(1,Nt);
53
54      %% Driving pressure
55      P=P0*cos(2*pi*freq*t);
56      %to intorduce non-lin add line uncomment below and comment above
57      %+P0/2*cos(2*pi*2*freq*t)+P0/3*cos(2*pi*3*freq*t);
58      ts=Nstart/freq*2;
59      Nis=round(ts/dt/2);
60      P(1:Nis)=P(1:Nis).*(1-cos(2*pi*(1:Nis)*dt/ts))/2;
61
62      %differential equation calculation  'Exact method' single ...
           solution
63
64  for n=2:Nt-1
65  dp_rho=1/rho*((p0+2*sigma/R0-pv)*(R0/R(n))^(3*k)+pv-2*sigma/R(n)-p0-P(n));
66  a=1;
67  b=8/3*R(n)-2*R(n-1)+(16*etha*dt)/(3*rho*R(n));
68  c=R(n-1)^2-16/3*R(n)^2+8/3*R(n)*R(n-1)-((16*etha*dt)/(3*rho*R(n)))*R(n-1)-8/3*dt^
69  R(n+1)=real((-b+sqrt(b^2-4*a*c))/(2*a));
70  Δ(n+1)=b^2-4*a*c;
71  end
72
73      %%%%%%%%%%%%%%%%%%%%%%%%%%%%%%%%%%%%%%%%%%%% ploting ...
           %%%%%%%%%%%%%%%%%
74  % calculation of FFT of R
```

```
75
76 t_interval=[0 max(t)];%time interval to analyse
77 jj=find(t>t_interval(1) & t<t_interval(2));
78 t_data=t(jj);
79 Data=R(jj);
80 ii=find(t_data>50e-6);
81 Data(ii)=0;
82 F=1:length(R);
83 F=F-mean(F);
84 F=F/length(R)*(1/dt);
85 FFT=fftshift(fft2(ifftshift(R)));
86 jj=find(F≥10e3 & F<2500e3);
87 FF=F(jj);
88 %plot of FFT
89
90 figure;plot(F(jj),20*log10(abs(FFT(jj)))),grid on,
91 axis([0 2.5e6 min(20*log10(abs(FFT(jj)))) ...
      max(20*log10(abs(FFT(jj))))])
92 xlabel('Fequency [MHz]')
93 ylabel(' Power [dB]')
94 title('Power Spectrum as sampled')
```

6.3.3 Model for translation speed of clouds

This code implements[1] the theory presented in §4.3.

```
1 clear all
2 close all
3
4 %----------coefficients
5
6 rho=998;%density
7
8 c=1480;%speed of sound
9
10 eta=10^-3;%dynamic shear viscosity
11
12 d=0.06;%damping coef
13
14 f=1.471e+6;%drivinig freq.
15
16
17 %----------------pressure signal in the wanted range
18
19 N=101;%number of samples
20
21 p_a_st=0.75;
22
23 p_a_sp=8.9;
24
25 dp_a=(p_a_sp-p_a_st)/N;
26
```

[1] I would like to note that this code was completely written by my self :), based on the paper of Kotoupolis [68] and the last author of that paper was not helpful at all. So I am not going to thank him.

```
27 p_a=p_a_st:dp_a:p_a_sp;
28
29
30 %------calculation of Radius using linear relation
31
32
33 R0=(10*p_a)-4.5026;% this law is slightly different than the one ...
       obtained by the data
34
35 %------------------ R0 from experiments
36 % P0=[.8,1.12,2.15,3.14,4.58,5.68,6.58,7.76,8.87];
37 % R0=[3.22,7.8,16.4,32.8,44.3,55,66.6,77.6,90];
38
39 % R0=interp1(P0,R0,p_a);
40
41 R0=R0*10^-6;%convert to right order
42 p_a=p_a.*10^6;%convert to right order
43 f_c=3./R0;%Minnaert frequency
44 figure
45 plot(p_a,R0)
46 xlabel('US pressure [Pa]')
47 ylabel('radius R0 [m]')
48 %hold all
49 for l=1:length(p_a)
50 %     if(p_a(l)<0.7*10^6)
51 %         d=0.15;
52 %     else
53 %         d=0.06;
54 %     end
55
56     v1(l)=p_a(l)^2/(6*rho*c*f*eta)*d*(f_c(1)/f)/(((f_c(1)/f)^2-1)^2+(d*(f_c(1)/f)
57
58
59    for r=1:length(f_c)
60
61     v2(l,r)=p_a(l)^2/(6*rho*c*f*eta)*d*(f_c(r)/f)/(((f_c(r)/f)^2-1)^2+(d*(f_c(r)/
62     %equation 13 of spiros paper
63
64    end
65
66
67
68 end
69
70 %------------ plotting
71 figure
72 hold on
73
74 dg=diag(v2);
75 p=plot(p_a,dg);
76 set(p,'Color','red','LineWidth',3)
77
78
79 %figure
80 n=8;
81 p_a_short=p_a(1:n:length(p_a));
82 v2_short=v2(1:n:length(p_a),1:n:length(p_a));
83 R0_short=R0(1:n:length(p_a));
```

```
84 plot(p_a_short,v2_short(:,:))
85 axis([0 p_a(end) 0 10])
86 xlabel('US pressure [Pa]')
87 ylabel('cloud speed [m/s]')
88 hold off
89
90 for l=1:length(dg)
91     p_al(l,1)=p_a(l);
92 end
```

Publications

Peer-reviewed journals

- **B. Gerold**, P. Glynne-Jones,C. McDougall,D. McGloin, S. Cochran, P. Prentice. Directed Jetting from Collapsing Cavities Exposed to Focused Ultrasound. *Applied Physics Letters*, 100,024104 (2012)

- **B. Gerold**, S. Kotopoulis, C. McDougall, D. McGloin, M. Postema , P. Prentice. Laser-nucleated acoustic cavitation in focussed ultrasound. *Review of Scientific Instruments*, 84(4) April 2011

- **B. Gerold**, I. Rachmilevitch, P. Prentice. Acoustic emissions from early stage cavitation clouds in focused ultrasound. *New Journal of Physics* (in press)

- M. Bobeica, **B. Gerold**, D. Xu ,R. Wang ,R. Habeshaw, P. Prentice, S. Cochran, and A. Melzer. Optimization of a High Throughput Device for Ultrasound-mediated Drug Delivery Experiments In- Vitro. *Review of Scientific Instruments* (in review process)

Conference papers

- **B. Gerold**, J. Joy, O. Prus, J. Grinfeld, A. Volovyk, Y. Medan, A. Melzer, S. Cochran1 P. Prentice Laser-nucleated acoustic cavitation: size matters. *WIMRC 3rd International Cavitation Forum proceedings 2011, Coventry, England*

- **B. Gerold**,D. Gourevich ,D. Xu ,F. Arditti ,P. Prentice ,S. Cochran ,J. Gnaim ,M. Yoav ,L. Wang andA. Melzer. Applicator for In-vitro Ultrasound-activated Targeted Drug Delivery. *International Society for Therapeutic Ultrasound proceeding 2011.*

- D. Gourevich, **B. Gerold**, F. Arditti, D. Xu, D. Liu, A. Volovick, L. Wang, Y. Medan, J. Gnaim, P. Prentice, S. Cochran, A. Melzer. Ultrasound ac-

tivated nano-encapsulated targeted drug delivery and tumor cell poration. *47th Oholo conference 2010 proceedings, Eilat, Israel.*

- **Bjoern Gerold**, S. Reynolds, A. Melzer, S. Cochran, Early Exploration of MRI-compatible Diagnostic Ultrasound Transducers. *2010 IEEE International Ultrasonics Symposium (IUS) proceedings, San Diego, U.S.A.*

Presentations

- *'Ultrasound Activated Nano-Encapsulated Targeted Drug Delivery and Tumour Cell Poration'* Presented at the 47th Oholo Conference, Israel 2010.
- *'Ultra-High Speed Observation of Laser-Nucleated Acoustic Cavitation'* Presented at the International Society for Therapeutic Ultrasound, Heidelberg, Germany 2012 (peer review abstract and stundent travel award)
- *'Contolled Jetting from Collapsing Cavities Exposed to HIFU'* Presented at the International Society for Therapeutic Ultrasound, Heidelberg, Germany 2012 (peer review abstract and stundent travel award)
- *'Ultra-High Speed Observation of Laser-Nucleated Acoustic Cavitation'* 22nd Annual Postgraduate Student Research Symposium in Dundee, Scotland (**1st presentation price**)

Posters with award

- *'Ultra-high speed observation and acoustic emission analysis of cavitation in focused ultrasound'* IEEE US 2012 conference Dresden (peer review abstract and student travel award)
- *'Cavitation in therapeutic ultrasound'* 22nd International conference of Society for Medical Innovation and Technology (**1st poster price**)

References

[1] J. Abbott. Rationale and derivation of Mi and Ti - A review. *Ultrasound in Medicine & Biology*, 25(3):431–441, 1999. 17

[2] I. Akhatov, R. Mettin, C.-D. Ohl, U. Parlitz, and W. Lauterborn. Bjerknes force threshold for stable single bubble sonoluminescence. *Physical Review E*, 55(3):3747–3750, 1997. 33

[3] S. B. Barnett, G. R. ter Haar, M. C. Ziskin, W. L. Nyborg, K. Maeda, and J. Bang. Current status of research on biophysical effects of ultrasound. *Ultrasound in Medicine & Biology*, 20(3):205–218, 1994. 19

[4] C. E. Bell. Laser-induced high-pressure shock waves in water. *Applied Physics Letters*, 10(2):46, 1967. 30

[5] T. Benjamin and A. Ellis. The collapse of Cavitation bubbles and the pressure thereby produced against solid boundaries. *Philosophical Transactions for the Royal Society of Lodon.*, 260(1110):221–240, 1966. 105

[6] R. T. Beyer and R. T. Beyer. *Nonlinear Acoustics*. Acoustical Society of America, 1997. 21

[7] P. R. Birkin, D. G. Offin, C. J. B. Vian, and T. G. Leighton. Multiple observations of cavitation cluster dynamics close to an ultrasonic horn tip. *The Journal of the Acoustical Society of America*, 130(5):3379–3388, November 2011. 41, 48

[8] J. Blake and P. Robinson. Interaction of two cavitation bubbles with a rigid boundary. *Journal of Fluid Mechanics*, 255:707–721, 1993. 121

[9] J. Blake, B. B. Taib, and G. Doherty. Transient cavities near boundaries. Part 2. Free surface. *Journal of Fluid Mechanics*, 181:197–212, 1987. 104, 106, 111

[10] N. Bremond, M. Arora, C.-D. Ohl, and D. Lohse. Controlled Multibubble Surface Cavitation. *Physical Review Letters*, 96(22), June 2006. 90

[11] C. E. Brennen. An Introduction to Cavitation Fundamentals. In *WIMRC FORUM 2011*, pages 1–17. California Institute of Technology, Pasadena, California, USA, June 2011. 27

[12] C. Brennen. *Cavitation and bubble dynamics. 1995.* Oxford University Press, November 1995. 32, 42

[13] A. Brotchie, F. Grieser, and M. Ashokkumar. Effect of Power and Frequency on Bubble-Size Distributions in Acoustic Cavitation. *Physical Review Letters*, 102(8), February 2009. 40

[14] E. A. Brujan, T. Ikeda, K. Yoshinaka, and Y. Matsumoto. The final stage of the collapse of a cloud of bubbles close to a rigid boundary. *Ultrasonics - Sonochemistry*, 18(1):59–64, January 2011. 48

[15] E. F. Carome. Photographic studies of laserinduced pressure impulses in liquids. *Applied Physics Letters*, 11(2):64, 1967. 30

[16] E. F. Carome, N. A. Clark, and C. E. Moeller. Generation of acoustic signals in liquids by ruby laser-induced thermal stress transient. *Applied Physics Letters*, 4(6):95–97, 1964. 30

[17] E. F. Carome, C. MOELLER, and N. A. Clark. Intense Ruby-Laser-Induced Acoustic Impulses in Liquids. *Journal of the Acoustical Society of America*, 40(6):1462–&, 1966. 30

[18] F. Caupin and E. Herbert. Cavitation in water: a review. *Comptes Rendus Physique*, 7(9-10):1000–1017, November 2006. 35

[19] S. Chalker and E. S. C. Weiner. *Oxf Dict English Grammar*. Oxford University Press, USA, 1998. 27

[20] H. Chen, W. Kreider, A. Brayman, M. R. Bailey, and T. Matula. Blood Vessel Deformations on Microsecond Time Scales by Ultrasonic Cavitation. *Physical Review Letters*, 106(3), January 2011. 106, 126

[21] H. Chen, X. Li, M. Wan, and S. Wang. High-speed observation of cavitation bubble cloud structures in the focal region of a 1.2MHz high-intensity focused ultrasound transducer. *Ultrasonics - Sonochemistry*, 14(3):291–297, March 2007. 96

[22] Y.-H. Chen, H.-Y. Chu, and L. I. Interaction and Fragmentation of Pulsed Laser Induced Microbubbles in a Narrow Gap. *Physical Review Letters*, 96 (3), January 2006. 47

[23] A. Coleman and M. Choi. Detection of acoustic emission from cavitation in tissue during clinical extracorporeal lithotripsy. *Ultrasound in Medicine & Biology*, 22(8):1079–1087, 1996. 125

[24] C. C. Coussios, C. H. Farny, G. ter Haar, and R. A. Roy. Role of acoustic cavitation in the delivery and monitoring of cancer treatment by high-intensity focused ultrasound (HIFU). *International Journal of Hyperthermia*, 23(2):105–120, January 2007. 11, 33, 44

[25] C. C. Coussios and R. A. Roy. Applications of Acoustics and Cavitation to Noninvasive Therapy and Drug Delivery. *Annual Review of Fluid Mechanics*, 40(1):395–420, January 2008. 44

[26] E. D. Crawford and A. Barqawi. Targeted focal therapy: a minimally

invasive ablation technique for early prostate cancer. *Oncology (Williston Park, N.Y.)*, 21(1):27–32; discussion 33–4, 39, January 2007. 10

[27] L. D'Agostino and C. E. Brennen. On the acoustical dynamics of bubble clouds. In *Applied Mechanics, Bioengineering, and Fluids Engineering Conference*, 1983. 40

[28] L. D'Agostino and C. Brennen. Acoustical Absorption and Scattering Cross-Sections of Spherical Bubble Clouds. *Journal of the Acoustical Society of America*, 84(6):2126–2134, 1988. 39

[29] L. D'Agostino and C. Brennen. Linearized Dynamics of Spherical Bubble Clouds. *Journal of Fluid Mechanics*, 199:155–176, 1989. 40

[30] P. A. Dayton, K. E. Morgan, A. L. Klibanov, G. Brandenburger, K. R. Nightingale, and K. W. Ferrara. A preliminary evaluation of the effects of primary and secondary radiation forces on acoustic contrast agents. *IEEE Transactions on Ultrasonics, Ferroelectrics and Frequency Control*, 44(6): 1264–1277, 1997. 99, 100

[31] A. Delalande, S. Kotopoulis, T. Rovers, C. Pichon, and M. Postema. Sonoporation at a low mechanical index. *Bubble Science, Engineering & Technology*, 3(1):3–12, May 2011. 19

[32] A. Delalande, M.-F. Bureau, P. Midoux, A. Bouakaz, and C. Pichon. Ultrasound-assisted microbubbles gene transfer in tendons for gene therapy. *Ultrasonics*, 50(2):269–272, February 2010. 19

[33] C. Demore, Z. Yang, A. Volovick, S. Cochran, M. MacDonald, and G. Spalding. Mechanical Evidence of the Orbital Angular Momentum to Energy Ratio of Vortex Beams. *Physical Review Letters*, 108(19):194301, May 2012. 18

[34] E. A. Dick, S. D. Taylor-Robinson, H. C. Thomas, and W. M. W. Gedroyc. Ablative therapy for liver tumours. *Gut*, 50:733–739, 2002. 10

[35] A. Doinikov. On the radiation pressure on small spheres. *Journal of the Acoustical Society of America*, 100(2):1231–1233, 1996. 41

[36] I. Donald, J. Macvicar, and T. G. Brown. Investigation of abdominal masses by pulsed ultrasound. *The Lancet*, 1(7032):1188–1195, June 1958. 7

[37] F. Duck. Nonlinear acoustics in diagnostic ultrasound. *Ultrasound in Medicine & Biology*, 28(1):1–18, 2002. 20, 21

[38] A. Ellis. Parameters affecting cavitation and some new methods for their study. Technical report, 1965. 110

[39] K. D. Evans, B. Weiss, and M. Knopp. High-Intensity Focused Ultrasound (HIFU) for Specific Therapeutic Treatments: A Literature Review. *Journal of Diagnostic Medical Sonography*, 23(6):319–327, November 2007. 9

[40] R. Evans, S. Camacho-López, F. G. Pérez-Gutiérrez, and G. Aguilar. Pump-probe imaging of nanosecond laser-induced bubbles in agar gel. *Optics express*, 16(10):7481–7492, May 2008. 47

[41] M. P. Felix and A. Ellis. LaserInduced Liquid Breakdowna StepByStep Account. *Applied Physics Letters*, 19(11):484–486, 1971. 30

[42] J. Field and A. Walton. Gas compression and jet formation in cavities collapsed by a shock wave. *Nature*, 1988. 104

[43] F. E. Fox and W. A. Wallace. Absorption of Finite Amplitude Sound Waves. *Journal of the Acoustical Society of America*, 26:994–1006, November 4. 21

[44] V. Frenkel, J. Oberoi, M. J. Stone, M. Park, C. Deng, B. J. Wood, Z. Neeman, M. Horne, and K. C. P. Li. Pulsed High-Intensity Focused Ultrasound Enhances Thrombolysis in an in Vitro Model. *Radiology*, 239(1):86–93, February 2006. 26

[45] F. J. Fry. Precision high intensity focusing ultrasonic machines for surgery. *American journal of physical medicine*, 37(3):152–156, June 1958. 9

[46] S. Fujikawa and T. Akamatsu. Effects of the non-equilibrium condensation of vapour on the pressure wave produced by the collapse of a bubble in a liquid. *Journal of Fluid Mechanics*, 1980. 66

[47] J. Fujimoto, W. Lin, E. Ippen, and C. Puliafito. Time-resolved studies of Nd: YAG laser-induced breakdown. Plasma formation, acoustic wave generation, and cavitation. *Investigative Ophthalmology & Visual Science*, 26:1771–1777,, 1985. 30, 47

[48] A. Gelet, J.-Y. Chapelon, R. Bouvier, O. Rouviere, D. Lyonnet, and J. M. Dubernard. Transrectal high intensity focused ultrasound for the treatment of localized prostate cancer: factors influencing the outcome. *European Urology*, 40(2):124–129, August 2001. 10

[49] B. Gerold, P. Glynne-Jones, C. McDougall, D. McGloin, S. Cochran, A. Melzer, and P. Prentice. Directed jetting from collapsing cavities exposed to focused ultrasound. *Applied Physics Letters*, 100(2):024104, 2012. 110

[50] B. Gerold, S. Kotopoulis, C. McDougall, D. McGloin, M. Postema, and P. Prentice. Laser-nucleated acoustic cavitation in focused ultrasound. *Review of Scientific Instruments*, 82(4):044902, 2011. 49, 60, 63

[51] B. Gerold, I. Rachmilevitch, and P. Prentice. Bifurcation of ensemble oscillations and acoustic emissions from early stage cavitation clouds in focused ultrasound. *New Journal of Physics*, *in press* at time of writing, 2013. 81

[52] F. Gilmore. The growth or collapse of a spherical bubble in a viscous compressible liquid. 1952. 39

[53] H. Guzman, D. Nguyen, S. Khan, and M. Prausnitz. Ultrasound-mediated disruption of cell membranes. I. Quantification of molecular uptake and cell viability. *The Journal of the Acoustical Society of America*, 110(1):588–596, 2001. 45

[54] I. Hansson, V. Kedrinskii, and K. A. Morch. On the dynamics of cavity clusters. *Journal of Physics D: Applied Physics*, 15(9):1725, 2000. 40

[55] T. Hasegawa and K. Yosioka. AcousticRadiation Force on a Solid Elastic Sphere. *Journal of the Acoustical Society of America*, 46(5B):1139–1143, 1969. 18, 41, 42, 99

[56] E. Herbert and S. Balibar. Cavitation pressure in water. *Physical Review E*, 74(4), 2006. 36

[57] C. K. Holland and R. E. Apfel. An Improved Theory for the Prediction of Microcavitation Thresholds. *IEEE Transactions on Ultrasonics, Ferroelectrics and Frequency Control*, 36(2):204–208, 1989. 37

[58] C. K. Holland, C. X. Deng, R. E. Apfel, J. L. Alderman, L. A. Fernandez, and K. J. Taylor. Direct evidence of cavitation in vivo from diagnostic ultrasound. *Ultrasound in Medicine & Biology*, 22(7):917–925, 1996. 17

[59] R. Holt and R. A. Roy. Measurements of bubble-enhanced heating from focused, MHz-frequency ultrasound in a tissue-mimicking material. *Ultrasound in Medicine & Biology*, 27(10):1399–1412, 2001. 43

[60] T. Ikeda, S. Yoshizawa, M. Tosaki, J. Allen, S. Takagi, N. Ohta, T. Kitamura, and Y. Matsumoto. Cloud cavitation control for lithotripsy using high intensity focused ultrasound. *Ultrasound in Medicine & Biology*, 32 (9):1383–1397, September 2006. 125

[61] R. O. Illing, J. E. Kennedy, F. Wu, G. R. ter Haar, A. S. Protheroe, P. J. Friend, F. V. Gleeson, D. W. Cranston, R. R. Phillips, and M. R. Mid-

dleton. The safety and feasibility of extracorporeal high-intensity focused ultrasound (HIFU) for the treatment of liver and kidney tumours in a Western population. *British Journal of Cancer*, 93(8):890–895, September 2005. 10

[62] J. E. Kennedy, G. R. ter Haar, and D. W. Cranston. High intensity focused ultrasound: surgery of the future? *British Journal of Radiology*, 76(909): 590–599, September 2003. 9, 10, 15

[63] P. Kennedy. A first-order model for computation of laser-induced breakdown thresholds in ocular and aqueous media. I. Theory. *Quantum Electronics, IEEE Journal of*, 31(12):2241–2249, 1995. 31

[64] D. Kim, M. Ye, and C. Grigoropoulos. Pulsed laser-induced ablation of absorbing liquids and acoustic-transient generation. *Applied Physics a-Materials Science & Processing*, 67(2):169–181, 1998. 47

[65] Y.-s. Kim, H. Rhim, M. J. Choi, H. K. Lim, and D. Choi. High-Intensity Focused Ultrasound Therapy: an Overview for Radiologists. *Korean Journal of Radiology*, 9(4):291, 2008. 11, 23

[66] G. S. Kino. *Acoustic waves*. devices, imaging, and analog signal processing. Prentice Hall, 1987. 18

[67] D. P. Koller and P. M. Shankar. Acoustical emissions from bubble clouds. *Ultrasonics*, 32(3):229–233, 1994. 49

[68] S. Kotopoulis and M. Postema. Microfoam formation in a capillary. *Ultrasonics*, 50(2):260–268, February 2010. 93, 100, 138, 146

[69] B. Krasovitsky, A. Goldring, A. Harari, and E. Kimmel. Growth and collapse of vapour bubble and shockwave emission around holmium laser beam: theory and experiments. *Bubble Science, Engineering & Technology*, 2(1): 17–24, June 2010. 30

[70] V. A. Krassilnikov, V. V. Shklovskaya-Kordy, and L. K. Zarembo. On the Propagation of Ultrasonic Waves of Finite Amplitude in Liquids. *Journal of the Acoustical Society of America*, 29(5):642–647, May 1957. 21, 22

[71] F. Kremkau. Cancer-Therapy with Ultrasound - Historical Review. *Journal of Clinical Ultrasound*, 7(4):287–300, 1979. 8, 9, 10

[72] S. Kumar and C. E. Brennen. Nonlinear effects in the dynamics of clouds of bubbles. *The Journal of the Acoustical Society of America*, 89(2):707–714, February 1991. 40

[73] A. M. Lake, T. L. Hall, K. Kieran, J. B. Fowlkes, C. A. Cain, and W. W. Roberts. Histotripsy: Minimally Invasive Technology for Prostatic Tissue Ablation in an In Vivo Canine Model. *Urology*, 72(3):682–686, September 2008. 44

[74] W. Lauterborn and H. Bolle. Experimental investigations of cavitation-bubble collapse in the neighbourhood of a solid boundary. *Journal of Fluid Mechanics*, 72(02):391–399, 1975. 30, 89, 104

[75] W. Lauterborn and E. Cramer. Subharmonic route to chaos observed in acoustics. *Physical Review Letters*, 47(20):1445–1448, 1981. 74, 76, 78, 81

[76] W. Lauterborn and T. Kurz. Physics of bubble oscillations. *Reports on Progress in Physics*, 73(10):106501, September 2010. 4, 31, 32, 34, 40, 78, 81

[77] C. Lee. Acoustic radiation force on a bubble. *J AcoustSoc Am*, 93(3), 1993. 18

[78] C. P. Lee and T. G. Wang. Acoustic radiation pressure. *The Journal of the Acoustical Society of America*, 94(2):1099–1109, 1992. 18

[79] T. G. Leighton. Bubble population phenomena in acoustic cavitation. *Ultrasonics - Sonochemistry*, 2(s123-s136), 1995. 36, 49

[80] T. G. Leighton. *The acoustic bubble*. Academic Pr, 1997. 33, 35, 37, 38, 41, 77, 78, 81, 98, 104

[81] T. G. Leighton, A. J. Waltont, and M. J. W. Pickworth. Primary bjerknes forces. *Europena Journal of Physics*, 11:47–50, 1990. 33, 38, 42

[82] R. Manasseh, P. Tho, A. Ooi, K. Petkovic-Duran, and Y. Zhu. Cavitation microstreaming and material transport around microbubbles. *Physics Procedia*, 3(1):427–432, January 2010. 19

[83] P. Marmottant and S. Hilgenfeldt. Controlled vesicle deformation and lysis by single oscillating bubbles. *Nature*, 423(6936):153–156, May 2003. 19

[84] P. Marmottant and S. Hilgenfeldt. Controlled vesicle deformation and lysis by single oscillating bubbles. *Nature*, 423(6936):153–156, 2003. 45

[85] F. Marquet, M. Pernot, J.-F. Aubry, G. Montaldo, L. Marsac, M. Tanter, and M. Fink. Non-invasive transcranial ultrasound therapy based on a 3D CT scan: protocol validation and in vitroresults. *Physics in Medicine and Biology*, 54(9):2597–2613, April 2009. 25

[86] E. Martin, D. Jeanmonod, A. Morel, E. Zadicario, and B. Werner. High-intensity focused ultrasound for noninvasive functional neurosurgery. *Annals of Neurology*, 66(6):858–861, December 2009. 24

[87] W. McNamara, Y. Didenko, and K. Suslick. Sonoluminescence temperatures during multi-bubble cavitation. *Nature*, 401(6755):772–775, 1999. 85

[88] R. Mettin, I. Akhatov, U. Parlitz, C.-D. Ohl, and W. Lauterborn. Bjerknes forces between small cavitation bubbles in a strong acoustic field. *Physical Review E*, 56(3):2924–2931, 1997. 42, 43

[89] V. Misraï, M. Rouprêt, E. Chartier-Kastler, E. Comperat, R. Renard-Penna, A. Haertig, M.-O. Bitker, F. Richard, and P. Conort. Oncologic

control provided by HIFU therapy as single treatment in men with clinically localized prostate cancer. *World Journal of Urology*, 26(5):481–485, June 2008. 10

[90] K. A. Morch. Cavitation Nuclei: Experiments and Theory. *Journal of Hydrodynamics*, 21(2):176–189, April 2009. 40

[91] E. Neppiras. Acoustic Cavitation. *Physics Reports-Review Section of Physics Letters*, 61(3):159–251, 1980. 34

[92] T. Neumann and H. Ermert. Schlieren visualization of ultrasonic wave fields with high spatial resolution. *Ultrasonics*, 44:e1561–e1566, December 2006. 55

[93] B. Niemczewki. Observations of water cavitation intensity under practical ultrasonic cleaning conditions. *Ultrasonics - Sonochemistry*, 14(1):13–18, January 2007. 48

[94] NIH-PA. Section 2–Definitions and description of nonthermal mechanisms. American Institute of Ultrasound in Medicine. In *Journal of Ultrasound in Medicine*, pages 77–68, February 2000. 19

[95] W. Nyborg. Biological effects of ultrasound: development of safety guidelines. Part II: general review. *Ultrasound in Medicine & Biology*, 27(3), 2001. 19

[96] W. O'Brien, Jr. Assessing the risks for modern diagnostic ultrasound imaging. *Japanese Journal of Applied Physics*, 1998. 16, 32

[97] W. O'Brien, Jr. Ultrasound–biophysics mechanisms. *Progress in Biophysics and Molecular Biology*, 93(1-3):212–255, January 2007. 8, 13, 26

[98] C.-D. Ohl, T. Kurz, R. Geisler, O. Lindau, and W. Lauterborn. Bubble dynamics, shock waves and sonoluminescence. *Philosophical Transactions*

of the Royal Society of London Series a-Mathematical Physical and Engineering Sciences, 357(1751):269–294, 1999. 31, 40

[99] R. Omta. Oscillations of a Cloud of Bubbles of Small and not So Small Amplitude. *Journal of the Acoustical Society of America*, 82(3):1018–1033, March 1987. 40

[100] P. Palanchon, P. Tortoli, A. Bouakaz, M. Versluis, and N. De Jong. Optical observations of acoustical radiation force effects on individual air bubbles. *IEEE Transactions on Ultrasonics, Ferroelectrics and Frequency Control*, 52(1):104–110, January 2005. 49, 93

[101] D. Palanker and I. Turovets. Dynamics of ArF excimer laser-induced cavitation bubbles in gel surrounded by a liquid medium. *Lasers in surgery and medicine*, 1997. 47

[102] U. Parlitz, V. Englisch, C. Scheffczyk, and W. Lauterborn. Bifurcation structure of bubble oscillators. *Journal of the Acoustical Society of America*, 88(2):1061–1077, July 1990. 78

[103] U. Parlitz, R. Mettin, S. Luther, I. Akhatov, M. Voss, and W. Lauterborn. Spatio-temporal dynamics of acoustic cavitation bubble clouds. *Philosophical Transactions of the Royal Society of London Series a-Mathematical Physical and Engineering Sciences*, 357(1751):313–334, 1999. 49, 93

[104] A. Philipp and W. Lauterborn. Cavitation erosion by single laser-produced bubbles. *Journal of Fluid Mechanics*, 361:75–116, 1998. 104, 106

[105] P. Prentice, A. Cuschieri, K. Dholakia, M. Prausnitz, and P. Campbell. Membrane disruption by optically controlled microbubble cavitation. *Nature Physics*, 1(2):107–110, October 2005. 45, 125

[106] A. Prospetti. Nonlinear oscillations of gas bubbles in liquids: steadystate

solutions. *Journal of the Acoustical Society of America*, 56(3):878–885, October 2004. 93

[107] L. Rayleigh. VIII. On the pressure developed in a liquid during the collapse of a spherical cavity. *Philosophical Magazine Series 6*, 34(200):94–98, August 1917. 28

[108] L. Reslan, J.-L. Mestas, S. Herveau, J.-C. Béra, and C. Dumontet. Transfection of cells in suspension by ultrasound cavitation. *Journal of Controlled Release*, 142(2):251–258, March 2010. 45

[109] R. S. Rosenson, A. McCormick, and E. F. Uretz. Distribution of blood viscosity values and biochemical correlates in healthy adults. *Clinical Chemistry*, 42(8):1189–1195, July 1996. 85

[110] G. Sankin, F. Yuan, and P. Zhong. Pulsating Tandem Microbubble for Localized and Directional Single-Cell Membrane Poration. *Physical Review Letters*, 105(7), August 2010. 106

[111] J. B. Segur and H. E. Oberstar. Viscosity of Glycerol and Its Aqueous Solutions. *Industrial & Engineering Chemistry*, 43(9):2117–2120, September 1951. 85

[112] A. Shaw and G. ter Haar. Requirements for measurement standards in high intensity focused ultrasound (HIFU) fields. *NPL Report*, pages 1744–0599, 2006. 49

[113] T. L. Szabo. *Diagnostic ultrasound imaging.* inside out. Academic Press, 2004. 8

[114] G. ter Haar. Therapeutic ultrasound. *European Journal of Ultrasound*, 9: 3–9, 1999. 10

[115] G. ter Haar, A. R. Clark, M. G. Vaughan, and C. R. Hill. Trackless Surgery

Using Focused Ultrasound - Technique and Case-Report. *Minimally Invasive Therapy & Allied Technologies*, 1(1):13–19, 1991. 10

[116] G. R. ter Haar. Safety and bio-effects of ultrasound contrast agents. *Medical & Biological Engineering & Computing*, 47(8):893–900, July 2009. 17

[117] J. Tervo, R. Mettin, and W. Lauterborn. Bubble cluster dynamics in acoustic cavitation. *Acta Acustica United with Acustica*, 92(1):178–180, 2006. 40, 41, 48

[118] G. Thalhammer, R. Steiger, M. Meinschad, M. Hill, S. Bernet, and M. Ritsch-Marte. Combined acoustic and optical trapping. *Biomedical optics express*, 2(10):2859–2870, October 2011. 18

[119] Y. Tomita, A. Shima, and K. Sato. Dynamic behavior of twolaserinduced bubbles in water. *Applied Physics Letters*, 1990. 104

[120] R. Tong, W. Schiffers, S. Shaw, J. Blake, and D. Emmony. The role of 'splashing' in the collapse of a laser-generated cavity near a rigid boundary. *Journal of Fluid Mechanics*, 380:339–361, 1999. 48

[121] Y.-S. Tung, F. Marquet, T. Teichert, V. Ferrera, and E. E. Konofagou. Feasibility of noninvasive cavitation-guided blood-brain barrier opening using focused ultrasound and microbubbles in nonhuman primates. *Applied Physics Letters*, 98(16):163704, 2011. 25, 46

[122] A. van Wamel, K. Kooiman, M. Harteveld, M. Emmer, F. J. ten Cate, M. Versluis, and N. De Jong. Vibrating microbubbles poking individual cells: Drug transfer into cells via sonoporation. *Journal of Controlled Release*, 112(2):149–155, May 2006. 19

[123] A. Vogel, S. Busch, and U. Parlitz. Shock wave emission and cavitation bubble generation by picosecond and nanosecond optical breakdown in wa-

ter. *Journal of the Acoustical Society of America*, 100(1):148–165, 1996. 31, 63

[124] N. Vykhodtseva, N. J. McDannold, and K. Hynynen. Progress and problems in the application of focused ultrasound for blood–brain barrier disruption. *Ultrasonics*, 48(4):279–296, August 2008. 45

[125] P. Wang, C. Xu, X. Xia, J. Xu, X. Wang, J. Xiang, and A. W. Leung. Mitochondrial damage in nasopharyngeal carcinoma cells induced by ultrasound radiation in the presence of hypocrellin B. *Journal of ultrasound in medicine : official journal of the American Institute of Ultrasound in Medicine*, 29(1):43–50, January 2010. 18

[126] T.-Y. Wang, Z. Xu, T. L. Hall, J. B. Fowlkes, and C. A. Cain. An Efficient Treatment Strategy for Histotripsy by Removing Cavitation Memory. *Ultrasound in Medicine & Biology*, 38(5):753–766, May 2012. 48

[127] M. M. Ward, J. J. Wu, and J. F. J. Chiu. Ultrasound-induced cell lysis and sonoporation enhanced by contrast agents. *Journal of the Acoustical Society of America*, 105(5):2951–2957, April 1999. 45

[128] M. Warmuth, T. Johansson, and P. Mad. Systematic review of the efficacy and safety of high-intensity focussed ultrasound for the primary and salvage treatment of prostate cancer. *European Urology*, 58(6):803–815, December 2010. 24

[129] N. Watkin and G. Ter Haar. The intensity dependence of the site of maximal energy deposition in focused ultrasound surgery. *Ultrasound in Medicine & Biology*, 22(4):483–491, 1996. 10

[130] E. Weitendorf. On the History of Propeller Cavitation and Cavitation Tunnels. *CAV2001 conference proceedings*, 2001. 28, 29

[131] E. G. Williams and J. A. Mann, III. Fourier Acoustics: Sound Radiation and Nearfield Acoustical Holography. *The Journal of the Acoustical Society of America*, 2000. 141

[132] F. Wu. Extracorporeal high intensity focused ultrasound ablation in the treatment of 1038 patients with solid carcinomas in China: an overview. *Ultrasonics - Sonochemistry*, 11(3-4):149–154, May 2004. 11

[133] F. Wu. Extracorporeal high intensity focused ultrasound in the treatment of patients with solid malignancy. *Minimally Invasive Therapy & Allied Technologies*, 15(1):26–35, January 2006. 9

[134] F. Wu, W.-Z. Chen, J. Bai, J.-Z. Zou, Z. L. Wang, H. Zhu, and Z.-B. Wang. Pathological changes in human malignant carcinoma treated with high-intensity focused ultrasound. *Ultrasound in Medicine & Biology*, 27 (8):1099–1106, August 2001. 10, 11

[135] F. Wu, Z.-B. Wang, Y.-D. Cao, W.-Z. Chen, J. Bai, J.-Z. Zou, and H. Zhu. A randomised clinical trial of high-intensity focused ultrasound ablation for the treatment of patients with localised breast cancer. *British Journal of Cancer*, 89(12):2227–2233, December 2003. 11

[136] F. Wu, Z.-B. Wang, W.-Z. Chen, H. Zhu, J. Bai, J.-Z. Zou, K.-Q. Li, C. B. Jin, F.-L. Xie, and H.-B. Su. Extracorporeal High Intensity Focused Ultrasound Ablation in the Treatment of Patients with Large Hepatocellular Carcinoma. *Annals of Surgical Oncology*, 11(12):1061–1069, December 2004. 26

[137] J. WU, J. Pepe, and M. Rincon. Sonoporation, anti-cancer drug and antibody delivery using ultrasound. *Ultrasonics*, 44:e21–e25, December 2006. 19

[138] J. Wu and W. L. Nyborg. Ultrasound, cavitation bubbles and their interac-

tion with cells. *Advanced Drug Delivery Reviews*, 60(10):1103–1116, June 2008. 19

[139] K. Yasui. Influence of ultrasonic frequency on multibubble sonoluminescence. *Journal of the Acoustical Society of America*, 112(4):1405–1413, September 2002. 40

[140] K. Yoisioka and Y. Kawasima. Acoustic radiation force on compressible sphere. *Acoustica*, 5, November 1955. 18, 99

[141] S. Yoon, L. A. Crum, A. Prospetti, and N. LU. An Investigation of the Collective Oscillations of a Bubble Cloud. *Journal of the Acoustical Society of America*, 89(2):700–706, 1991. 35

[142] Y. Zhou, J. Qin, and P. Zhong. Characteristics of the Secondary Bubble Cluster Produced by an Electrohydraulic Shock Wave Lithotripter. *Ultrasound in Medicine & Biology*, 38(4):601–610, April 2012. 48